COMPLEX EDGE STATES IN TAILORED PHOTONIC GRAPHENE

DISSERTATION

zur Erlangung des akademischen Grades
doctor rerum naturalium (Dr. rer. nat.)

vorgelegt dem Rat der Physikalisch-Astronomischen Fakultät
der Friedrich-Schiller-Universität Jena

von Dipl.-Phys. Julia Margarethe Zeuner
geboren am 07. Juni 1985 in Passau

1. Gutachter:	Prof. Dr. Alexander Szameit, *Friedrich-Schiller-Universität Jena*
2. Gutachter:	Prof. Dr. Fedor Mitschke, *Universität Rostock*
3. Gutachter:	Prof. Robert Thomson, Ph.D., *Heriot-Watt University Edinburgh*

Tag der Disputation: 14.03.2017

CONTENTS

1

INTRODUCTION

In 2010, the Nobel prize in physics was awarded to A. Geim and K. Novoselov for the realization and characterization of graphene [1–3]. At a time when groundbreaking discoveries are typically made at the far end of the periodic table with its currently 118 elements, or in the development of ever-more complex composite materials, one might ask what makes a simple honeycomb sheet of carbon atoms so outstanding as to merit the ensuing whirlwind of scientific attention. A hint lies in the fact that it was indeed the Nobel prize in physics, and not chemistry, that was awarded a mere six years after the first experiments. Indeed, in addition to being the first genuinely two-dimensional (2D) material, graphene offers a host of fascinating properties, many of which are deeply rooted in its very structure. Despite consisting of only a single layer of atoms and being extremely flexible [4], the mechanical strength of graphene exceeds that of steel by two orders of magnitude [5]. At the same time, it offers unusually high thermal [6] as well as electrical conductivities [7]. Finally, its astonishingly low optical absorption coefficient is related to the fine structure constant and not proportional to the wavelength [8], rendering graphene highly transparent throughout the optical regime.

Thus, graphene and other subsequently realized 2D materials, such as Boronnitride, are promising for applications as flexible or/and transparent conductors, as for touch screens, light panels, or solar cells. Furthermore, due to graphene's extremely high charge carrier mobility it is uniquely suited for high-frequency applications, such as satellite communications or radar. Beyond such practical considerations, graphene is a fascinating material from the vantage point of fundamental physics. In particular, its seemingly simple atomic structure leads to a unique electron dynamics as described by the band structure with its singular points of the Fermi energy. Together with the linear nature of the bands in the vicinity of these points, the dispersion relation is reminiscent of a system governed by a massless Dirac type equation. Indeed, a formal equivalence exists between excitations of graphene and relativistic 2D Dirac physics. Along these lines, the honeycomb structure of the graphene lattice allows for the observation of an unusual quantum Hall effect [7,9], as well as the exotic Klein tunneling [10] that had evaded the grasp of experimentalists since its prediction in 1929 [11].

The aim of this work is to bring the fascinating structural properties of graphene to bear in the optical domain. To this end, two dimensional photonic lattices comprised of evanescently coupled waveguides take the place of individual atoms, and the temporal evolution of the elctronic wave function is replaced by the coherent propagation of light. Since this "photonic graphene" is mathematically equivalent to its carbon-based namesake, its various aspects will be studied at time- and length-scales which are readily accessible to experiments. Going beyond mere emulation, it will be shown that graphene inspired ideas can be adapted and systematically extended to enrich the design and functionality of integrated photonic systems. Remarkably, photonic graphene turns out to be more flexible in terms of its parameters than the conventional carbon lattice. Examples are the preparation of arbitrary edge terminations, a straight forward and continuous control over the mass (i.e. the effective index) of individual sites, and the possibility to implement even extreme lattice deformations that would by far exceed the mechanical stability of an atomic lattice. It is this versatility and access to new degrees of freedoms that makes photonic graphene the starting point for an entirely new field of optics: topological photonics. Here, very robust light transport being insensitive to defects and fabrication disorder can be realized. This seems promising for many different optical components susceptible to parasitic scattering in integrated photonic circuits. Moreover, it constitutes one step towards the vision of all-optical circuitry being as fast as the speed of light.

This thesis will first introduce selected basic properties of atomic graphene which are subsequently connected to the photonic system. Within the Fundamentals' Chapter the atomic lattice of graphene is explained, its famous connection to relativistic physics is derived, as well as a basic understanding of topology in physics and of edge state properties of the graphene lattice is given. The transfer to the optical system is accomplished in the third part of the Fundamentals' Chapter and the relations between the atomic system and its photonic counterpart are revealed. Moreover, the technical aspects to realize photonic graphene and the techniques enabling the different experiments, as presented in the main Chapters 3-5, complete the Fundamentals. The approaches established in the main Chapters are all based on the implementation of various modifications of the basic photonic graphene lattice geometry and were performed in collaboration with the Technion – Israel Institute of Technology. The topological robustness and its limits in graphene are derived in Chapter 3 by stretching the lattice to an extremely high extent. A completely different kind of deformation of the honeycomb structure is revealed in Chapter 4, demonstrating the realization of the first pseudomagnetic field in optics leading to the remarkable Dirac Landau level structure. As opposed to the atomic system and as explained in this Chapter, in the photonic system the Landau level splitting cannot act as the basis to realize the prominent quantum Hall effect. However, to develop further these thoughts, Chapter 5 utilizes another way enabling the experimental realization of special robust topological edge states being known as one of the remarkable properties of the quantum Hall effect. Finally, in Chapter 6, the conclusion of this thesis and an outlook to future possible studies is presented.

2

FUNDAMENTALS

2.1 GRAPHENE

Graphene, consisting of a single layer of carbon atoms, is the first two-dimensional (2D) material which ever was realized. Since its first discovery in 2004 [1], it is celebrated as a new wonder material due to its exceptional properties [4–8]. However, graphene is not only promising in terms of applications but also gained a lot of interest in fundamental physics [9, 12–16]. In this section, the basics about the atomic structure of graphene will be given in the scope of the tight-binding model which is able to explain a lot of the characteristic properties of the material. Furthermore, the special topology of the material with different edge states and their properties will be introduced since they play a major role in all experiments in photonic graphene presented within this work. At the end there will be a section introducing the basics about very extraordinary edge states being robust against scattering. To achieve such states the feature of graphene of exhibiting singular points in the band structure can serve as a starting point.

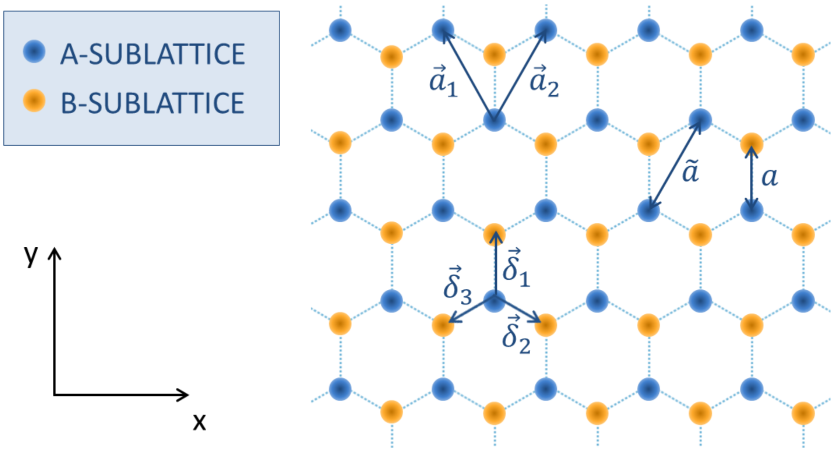

Figure 2.1: Atomic honeycomb structure of graphene consisting of two equivalent sublattices A and B with primitive translation vectors $\vec{a}_1$ and $\vec{a}_2$. The nearest neighbour distance is named a being converted to the lattice constant via $\tilde{a} = \sqrt{3}a$. The vectors describing the positions of adjacent B sites to one A site are given by $\vec{\delta}_1$, $\vec{\delta}_2$, and $\vec{\delta}_3$.

2.1.1 ATOMIC LATTICE AND TIGHT-BINDING DESCRIPTION

ATOMIC LATTICE STRUCTURE. Graphene naturally occurs in the guise of graphite, the by far most common phase of carbon. This seemingly unremarkable material consists of loosely bound stacks of individual graphene sheets with carbon atoms arranged in a honeycomb pattern. Since in graphite the carbon atoms in each layer are bound much stronger than the different lattice layers, it is possible to obtain graphene by micromechanical cleavage of graphite [2]. Moreover, the simplest description of the electronic structure of graphite is based on graphene and its special band structure was first characterized in 1947 by Wallace [17]. On the most fundamental level, the honeycomb lattice structure of graphene can be described as a triangular Bravais lattice consisting of two equivalent sublattices A and B being shifted to each other by a vector $\vec{\delta}_1 = (0, a)$ as shown in Fig. 2.1. The primitive translation vectors

$$\vec{a}_1 = \frac{a}{2}\left(-\sqrt{3}, 3\right), \quad \vec{a}_2 = \frac{a}{2}\left(\sqrt{3}, 3\right), \tag{2.1}$$

span up the unit cell, where $a \approx 1.42$ Å is the nearest neighbour distance between two atoms and the lattice constant is $\tilde{a} = \sqrt{3}a$. The vectors δ_i, connecting the two sublattices,

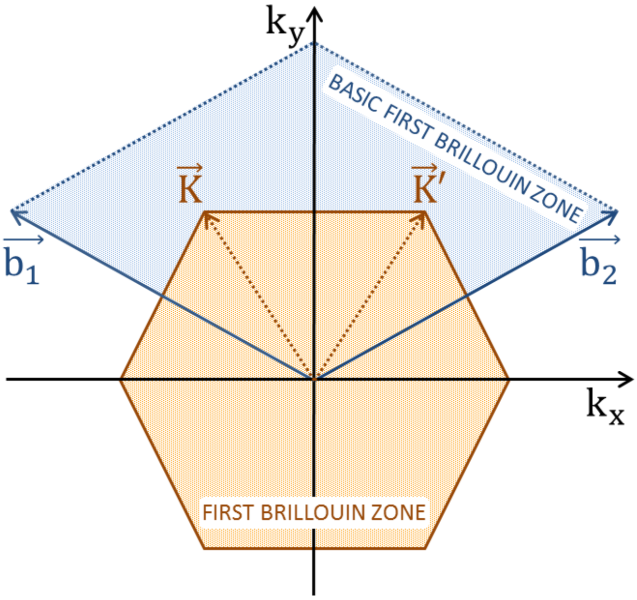

Figure 2.2: Primitive vectors of the reciprocal lattice with its associated unit cell, which equals to the basic first Brillouin zone, and two of the Dirac points K and K'. Furthermore, the hexagonal first Brillouin zone is shown which is commonly used for convenience.

are given by:

$$\vec{\delta}_1 = (a, 0), \quad \vec{\delta}_2 = \frac{a}{2}\left(\sqrt{3}, 1\right), \quad \vec{\delta}_3 = -\frac{a}{2}\left(\sqrt{3}, 1\right). \tag{2.2}$$

The reciprocal lattice is a triangular lattice, as well, with its lattice vectors fulfilling the condition $\vec{b}_i \cdot \vec{a}_j = 2\pi\delta_{ij}$:

$$\vec{b}_1 = \frac{2\pi}{3a}(-\sqrt{3}, 1), \quad \vec{b}_2 = \frac{2\pi}{3a}(\sqrt{3}, 1). \tag{2.3}$$

The first Brillouin zone (BZ) can be described by these two vectors, but for reasons of convenience, commonly a hexagonal BZ is used as shown in Fig. 2.2. Of particular relevance are the high-symmetry points K and K'. The implications of these so-called "Dirac points" for the properties of the graphene lattice will be discussed in detail in Section 2.1.3.

TIGHT-BINDING DESCRIPTION. Each carbon atom has four valence electrons. In the graphene lattice, three of them form σ-bonds with adjacent atoms, whereas the remaining one is in a π-state and therefore can serve as conduction electron [18]. This allows to describe graphene in a good approximation with a tight-binding description.

Furthermore, here only nearest neighbour interactions will be included. Hence, atoms from the A sublattice exclusively interact with atoms from the B sublattice and vice versa, leading to a 2 × 2 Hamiltonian. Assuming an infinite lattice, the Hamiltonian can be set up in Bloch form with c_1, c_2, and c_3 being the nearest neighbour hopping parameters along δ_1, δ_2, and δ_3, respectively (as defined in Fig. 2.1):

$$H = \sum_{\vec{k}} \begin{pmatrix} a^+(\vec{k}) & b^+(\vec{k}) \end{pmatrix} H_B(\vec{k}) \begin{pmatrix} a(\vec{k}) \\ b(\vec{k}) \end{pmatrix}, \tag{2.4}$$

with the Bloch-Hamiltonian

$$H_B(\vec{k}) = \begin{pmatrix} 0 & \tilde{S}(\vec{k}) \\ \tilde{S}^*(\vec{k}) & 0, \end{pmatrix} \tag{2.5}$$

which contains only off-diagonal elements, defined by

$$\tilde{S}(\vec{k}) = c_1 + c_2 \mathrm{e}^{-i\vec{k}\vec{a}_1} + c_3 \mathrm{e}^{-i\vec{k}\vec{a}_2}. \tag{2.6}$$

For regular graphene the hopping parameters $c_1 = c_2 = c_3 := c$ are identical and thus Eq. (2.6) simplifies to $\tilde{S}(\vec{k}) = cS(\vec{k})$ with $S(\vec{k}) = 1 + \mathrm{e}^{-i\vec{k}\vec{a}_1} + \mathrm{e}^{-i\vec{k}\vec{a}_2}$. Inserting the primitive translation vectors for graphene (as defined in (2.1)) this yields:

$$\begin{aligned} S(\vec{k}) &= 1 + \mathrm{e}^{-i\left(-\frac{\sqrt{3}}{2}ak_x + \frac{3}{2}ak_y\right)} + \mathrm{e}^{-i\left(\frac{\sqrt{3}}{2}ak_x + \frac{3}{2}ak_y\right)} \\ &= 1 + \mathrm{e}^{-i\frac{3}{2}ak_y} \cdot 2\cos\left(\frac{\sqrt{3}}{2}ak_x\right). \end{aligned} \tag{2.7}$$

Hence, this explicitly defines the Bloch-Hamiltonian of the graphene lattice in the tight-binding approximation including nearest-neighbour interactions only.

2.1.2 BAND STRUCTURE

Based on the tight-binding Hamiltonian, in this section the band model of graphene will be derived. The energy spectrum of the lattice can directly be calculated as the

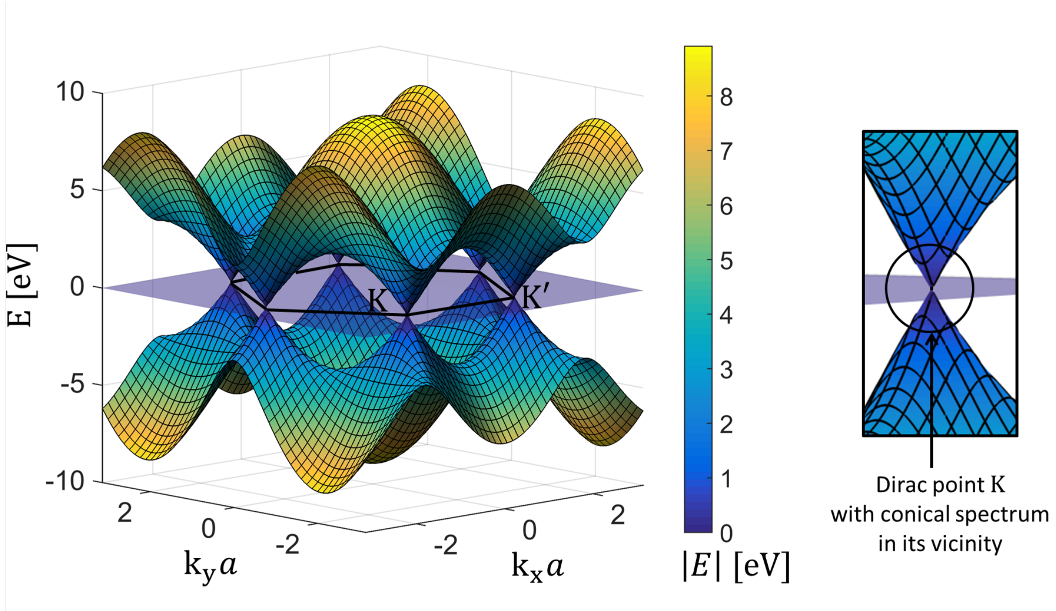

Figure 2.3: Energy spectrum of graphene with a hopping parameter of $c = -2.97\,\mathrm{eV}$ according to [19]. The plane at which the Dirac points K and K' (two of them are labelled) can be found, is shown in blue. The first BZ is defined by the black lines. On the right, a zoomed-in image of one of the Dirac-points is shown.

eigenvalue spectrum of the Bloch-Hamiltonian:

$$
\begin{aligned}
E(\vec{k}) &= \pm c|S(\vec{k})| \\
&= \pm c\left[\left(1 + \mathrm{e}^{-i\frac{3}{2}ak_y} \cdot 2\cos\left(\frac{\sqrt{3}}{2}ak_x\right)\right) \cdot \left(1 + \mathrm{e}^{+i\frac{3}{2}ak_y} \cdot 2\cos\left(\frac{\sqrt{3}}{2}ak_x\right)\right)\right]^{1/2} \\
&= \pm c\left[1 + \mathrm{e}^{i\frac{3}{2}ak_y} 2\cos\left(\frac{\sqrt{3}}{2}ak_x\right) + \mathrm{e}^{-i\frac{3}{2}ak_y} 2\cos\left(\frac{\sqrt{3}}{2}ak_x\right) + 4\cos^2\left(\frac{\sqrt{3}}{2}ak_x\right)\right]^{1/2} \\
&= \pm c\left[3 + 4\cos\left(\frac{\sqrt{3}}{2}ak_x\right)\cos\left(\frac{3}{2}ak_y\right) + 2\cos\left(\sqrt{3}ak_x\right)\right]^{1/2}, \qquad (2.8)
\end{aligned}
$$

using the trigonometrical relation $2\cos^2 x = \cos(2x) + 1$. (2.9)

The resulting band structure is shown in Fig. 2.3. The two bands are completely symmetric with respect to the zero-energy level since the two sublattices are identical and only nearest neighbour coupling is included. It exhibits points with zero slope at $\vec{k} = 0$; these are so-called van Hove singularities at which the density of states diverges [18,20]. More importantly it possesses very special intersection points at $\vec{K}$

and $\vec{K}'$, being calculated by setting $E(\vec{k}) \overset{!}{=} 0$:

$$\vec{K} = \left(-\frac{2\pi}{3\sqrt{3}a}, \frac{2\pi}{3a}\right),\ \vec{K}' = \left(\frac{2\pi}{3\sqrt{3}a}, \frac{2\pi}{3a}\right). \tag{2.10}$$

To facilitate an intuitive understanding of the equivalence between the points $\vec{K}$ and $\vec{K}'$, it is instructive to take a broader perspective beyond the first BZ, as shown in Fig. 2.3. In terms of lattice theory, the point $\vec{K}$ only differs to $-\vec{K}'$ by a reciprocal lattice vector $\vec{b} = \vec{b_1} - \vec{b_2}$. The Fermi energy level in graphene coincides with these band crossing points such that the material has a completely filled valence band and an empty conduction band without a gap in between [18]. Thus, from the point of band theory, the material is an example of a gapless semiconductor. However, the extraordinary properties do not mainly originate from the lack of the band gap but from the very special conical shape around the intersection points and from the symmetry of the band structure.

2.1.3 MASSLESS DIRAC FERMIONS

The shape of the band structure around the Fermi energy level plays a crucial role for understanding many extraordinary properties of graphene. To mathematically derive it, the Bloch-Hamiltonian and therefore in a first step $S(\vec{k})$ is expanded in a Taylor series to the first order around the Dirac points using $\delta\vec{k} = \vec{k} - \vec{K}$ and $\delta\vec{k}' = \vec{k} - \vec{K}'$:

$$\begin{aligned}
S_{\vec{K}}(\delta\vec{k}) &\approx \delta k_x \cdot \frac{\partial S}{\partial k_x}(\vec{K}) + \delta k_y \cdot \frac{\partial S}{\partial k_y}(\vec{K}) = \frac{3}{2}a(-\delta k_x + i\delta k_y),\\
\Rightarrow \quad H_{\vec{K}}(\delta\vec{k}) &\approx \frac{3}{2}ac \begin{pmatrix} 0 & -\delta k_x + i\delta k_y \\ -\delta k_x - i\delta k_y & 0 \end{pmatrix}\\
&= -\frac{3}{2}ac(\delta k_x\sigma_x + \delta k_y\sigma_y) = -\frac{3}{2}ac\,\delta\vec{k}\cdot\vec{\sigma} \qquad (2.11)\\
&= -\frac{3ac}{2\hbar}\vec{p}\vec{\sigma} \quad \text{and}\\
\Rightarrow \quad H_{\vec{K}'}(\delta\vec{k}') &\approx \frac{3}{2}ac(\delta k_x'\sigma_x - \delta k_y'\sigma_y) \qquad (2.12)\\
&= -H_{\vec{K}}^T(\delta\vec{k}) \qquad (2.13)
\end{aligned}$$

with the Pauli matrices $\sigma_x = \begin{pmatrix} 0 & 1 \\ 1 & 0 \end{pmatrix}$ and $\sigma_y = \begin{pmatrix} 0 & -i \\ i & 0 \end{pmatrix}$, and where T denotes the transposed matrix.

Hence, the energy band structure around the Dirac points yields:

$$\begin{aligned} E_{\vec{K}}(\delta\vec{k}) &\approx \pm\frac{3}{2}ac|\delta\vec{k}| = \pm v_F\hbar\,\delta k \\ E_{\vec{K}'}(\delta\vec{k}') &\approx \pm\frac{3}{2}ac|\delta\vec{k}'| = \pm v_F\hbar\,\delta k'. \end{aligned} \tag{2.14}$$

The calculation yields a linear slope of the spectrum around the Dirac points resulting in a conical dispersion relation (see Eq. (2.14)). Furthermore, the Hamiltonian in the vicinity of $\vec{K}$ and $\vec{K}'$ according to Eq. (2.13) corresponds to the Hamiltonian of the 2D Dirac-equation for massless particles. Though, the speed of light is here replaced by a Fermi-velocity of $v_F = \frac{3ac}{2\hbar}$. Note, that this is only valid close to the points $\vec{K}$ and $\vec{K}'$, which therefore are called Dirac points. It should be emphasized, that the Pauli-matrix $\vec{\sigma}$ does not describe a real spin in this context, but rather a so-called pseudospin representing the two atoms per unit cell. Since the Fermi energy of graphene resides at the conical points, the low-energy electrons behave as massless Dirac particles; with the Fermi-velocity given above corresponding to the speed of light in the original Dirac-equation. Consequently, using graphene one can perform experiments with Dirac-like dynamics without needing the extreme conditions usually associated with relativistic physics. One example for this is Klein-tunneling [11], which was first examined in a graphene lattice [10]. Furthermore, for graphene with a Fermi-energy at the Dirac points, a vanishing density of states (DOS) is found [21]. The special symmetry of the graphene lattice leading to the conical spectrum is one main reason for many of its remarkable properties as, e.g., the high carrier mobility [7].

2.2 TOPOLOGICAL PROPERTIES

As shown above, the low-energy electrons in graphene behave correspondingly to massless Dirac particles. However, as will be outlined in the following, the electronic properties of finite graphene pieces are also crucially influenced by the structure of their edges [22]. This section will explain some basics of the mathematical branch of topology playing a role in the graphene lattice and will point out the connections to the edge physics of the system.

Topology is a mathematical concept based on quantized variables being conserved under continuous deformations of bodies. To give a famous and descriptive example, a torus and a coffee cup with a handle may look completely different, but they can be described by the same topological number. Topology describes basic features of bodies that remain unaffected by continuous deformations, i.e., transformations which do not create or close holes. In the example of the coffee cup, the quantized topological invariant is called genus and, describing the number of holes in the object, has a value of 1. The connection between genus and the geometry of the body is the Gauss-Bonnet theorem [23]. What makes the topic so special is that topological numbers can only change discretely. Consequently, they are protected against perturbations with small continuous changes in the system parameters. Along these lines, any physical feature based on topological quantities would be extremely robust. The question naturally arises as to how the mathematical field of topology is related to physics in general and especially to an atomic lattice as graphene constituting the background of the present work. One example in physics, where such a topological behaviour plays a crucial role, is the quantum Hall effect. In 1980, Klaus von Klitzing made the extraordinary finding that the Hall resistance for a two-dimensional electron gas at low temperatures shows a very robust quantized steplike growth with increasing magnetic field [24]. Counterintuitively, the steps always exhibited the same height independent of sample parameters as, for instance, the size, the number of defects, the shape, and the charge carrier density. For his finding von Klitzing was awarded the Nobel Prize in 1985. Interestingly, it was shown that the robustness of the quantum Hall effect is based on a quantized topological invariant [25–27].

The theoretical description of the graphene structure usually is performed on the basis of an infinite lattice. Periodic two-dimensional (2D) lattices can be described in the reciprocal space by a 2D BZ which is periodical in both directions. This is exactly a torus if one closes the periodical boundaries of the BZ and for such a closed surface one can define topological quantities. Along these lines, this yields the connection between the field of topology and the graphene lattice.

Though, every real system naturally is finite and has boundaries, which are not described by the equations introduced in the last section. In some systems, they give rise to the existence of edge states which can lead to very interesting findings as for example in the quantum Hall effect. The connection between topological quantities defined on the basis of an infinite lattice (or rather a finite one with periodic boundary conditions) and the arising of edge states in the same, but finite, system is also sometimes called the bulk-edge correspondence [28].

Within this section, typical topological quantities will be defined, the fundamental edge states of graphene will be explained, and a short introduction to chiral edge states, as present in the quantum Hall effect, will be given.

2.2.1 BERRY PHASE AND WINDING NUMBER

One very important topological property, which for example distinguishes one Dirac point from the other, is the Berry phase. Originally, this quantity was found for a quantum mechanic system undergoing a closed adiabatic loop in the parameter space during which the wavefunction can accumulate a phase factor [29]. In the graphene lattice, the Berry phase can be accumulated by a wavefunction moved along a closed path in reciprocal space. It should be noted that the reciprocal space itself is closed since it is periodical in the k_x- and k_y-direction. Accordingly, the BZ of graphene is a torus. The Berry phase γ is calculated along a closed path in the phase space by

$$\gamma = \oint \langle u(\vec{k})|i\nabla_{\vec{k}}|u(\vec{k})\rangle \, d\vec{k} = \oint A(\vec{k})d\vec{k}, \tag{2.15}$$

where $A(\vec{k}) = \langle u(\vec{k})|i\nabla_{\vec{k}}|u(\vec{k})\rangle$ is called the Berry connection with u being the eigenvectors of the Bloch Hamiltonian at the wave vector $\vec{k}$. For one-dimensional problems in lattice systems, the Berry phase is also known as Zak phase [30]. Calculating this quantity for a closed loop around one Dirac cone of the graphene lattice yields either π or $-\pi$ for the point K or K', respectively. Along these lines, the Dirac points can be described by a topological property which is generally robust with respect to perturbations. Only for very strong distortions, for example when two Dirac points merge, this topological property changes.

To directly calculate the Berry phase in a graphene ribbon, it might be helpful to introduce a certain winding number, which will be shown here. The Bloch-Hamiltonian

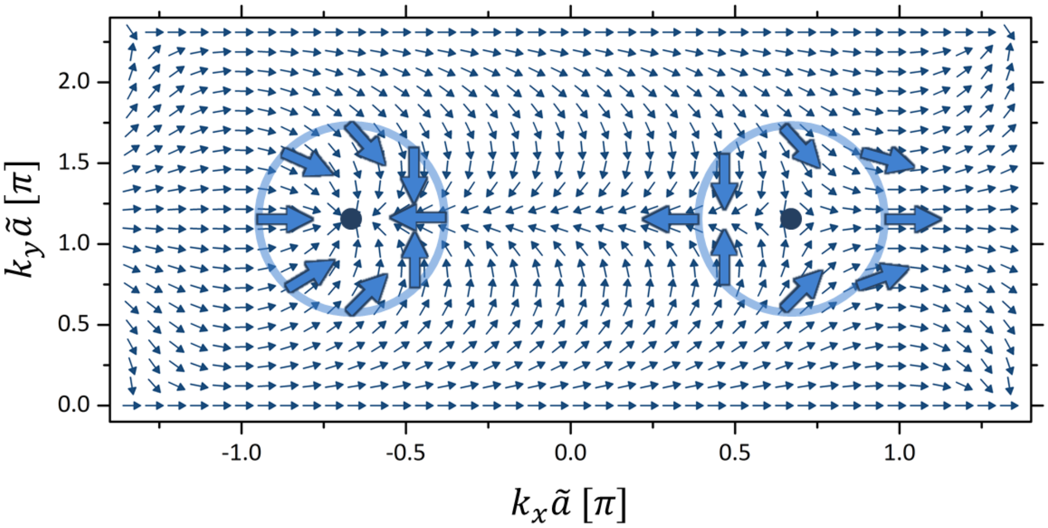

Figure 2.4: Vector $\vec{h}(\vec{k})$ plotted for different positions in the reciprocal space around two Dirac points K and K' marked by the blue dots. Along a closed integration path around a Dirac point the vector $\vec{h}(\vec{k})$ undergoes a complete clockwise (left) or counterclockwise (right) winding implying a Berry phase of π and $-\pi$, respectively.

as derived in Eq. (2.5) can be rewritten using the Pauli matrices $\vec{\sigma} = (\sigma_x, \sigma_y)$:

$$H_B = \vec{h}(\vec{k}) \cdot \vec{\sigma}\,, \text{with} \quad \vec{h}(\vec{k}) = c \begin{pmatrix} \Re(S(\vec{k})) \\ -\Im(S(\vec{k})) \end{pmatrix}. \tag{2.16}$$

The winding number w of the vector $\vec{h}(\vec{k})$ around the origin is connected to the Berry phase via $w = \gamma/\pi$ [31]. To retrace this in the equations one can express $S(\vec{k}) = |S(\vec{k})|\mathrm{e}^{-i\Phi(\vec{k})}$ by its amplitude and phase Φ and plug it into Eq. (2.16) leading to

$$\vec{h}(\vec{k}) = c|S(\vec{k})| \begin{pmatrix} \cos(\Phi(\vec{k})) \\ \sin(\Phi(\vec{k})) \end{pmatrix}. \tag{2.17}$$

From this equation it can be seen that the angle between $\vec{h}(\vec{k})$ and the positive x-axis is equal to the phase $\Phi(\vec{k})$. Furthermore, the eigenvectors of the Bloch-Hamiltonian are

$$|u(\vec{k})_\pm\rangle = \frac{1}{\sqrt{2}} \begin{pmatrix} \mathrm{e}^{-i\Phi(\vec{k})} \\ \pm 1 \end{pmatrix}. \tag{2.18}$$

If they are plugged into Eq.(2.15) this yields a Berry phase of:

$$\gamma = \frac{1}{2} \oint d\vec{k} \frac{d\Phi(\vec{k})}{d\vec{k}}. \tag{2.19}$$

Consequently, this allows to determine the Berry phase graphically by following the direction of $\vec{h}(\vec{k})$ along a closed loop in the BZ. An example is shown in Fig. 2.4, where the vector $\vec{h}(\vec{k})$ is plotted at a grid of positions in k-space. Along a closed path around two Dirac points K and K' the vector undergoes one complete clockwise or counterclockwise rotation. Hence, in one case a Berry phase of π is accumulated, in the other case $-\pi$, which is the topological property characterizing the Dirac points. In the following section, edge states in the graphene lattice will be introduced. Interestingly, the existence of the edge states is directly connected to the Berry phase along a certain path.

2.2.2 EDGE STATES

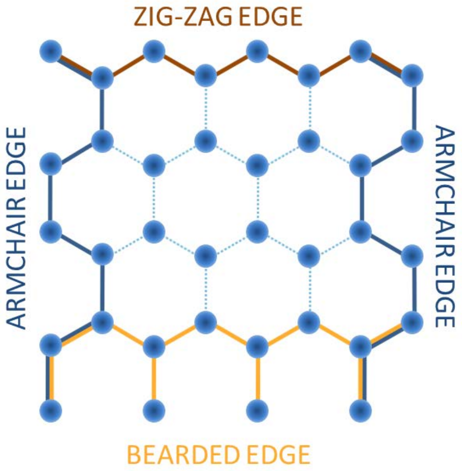

Figure 2.5: Three different main types of edges in a graphene lattice.

A finite honeycomb lattice allows for three fundamentally different terminations: armchair, zig-zag and bearded edges, as shown in Fig. 2.5. Note that in the context of carbon-based graphene, the dangling bonds associated with a bearded edge make this type of termination highly unstable [32]. As will be shown, this limitation does not exist for photonic implementations, and bearded edges actually provide a valuable degree of freedom for the design of discrete topological systems. So far, only an infinite lattice using Bloch's theorem was considered to derive the bulk properties of graphene. However, in a real and hence finite system the edges of the material lead to significant changes in the electronic structure, such as the emerging of edge states.

In particular, graphene supports a special type of zero-energy edge states that rely on chiral symmetry [33–36]. They can be found at the zero energy point in the tight-binding band structure and reside at the lattice edge. They are characterized by an exponential decay into the bulk of the lattice, and consequently a certain localization length related to them can be defined [37]. Interestingly, these edge states only exist at the bearded and zig-zag edge, but not at the armchair edge. To visualize their position in reciprocal space, the tight-binding edge band structure is calculated. For that purpose, a unit cell is used that is periodic in the x-direction but finite in the y-direction, or vice versa depending on the edge under consideration. The termination is chosen such that the respective edge type is formed as depicted in Fig. 2.6(a)-(c). In the right column of Fig. 2.6, the associated dispersion curves of these semi-infinite arrays of graphene with (d) only armchair edges, (e) only zig-zag edges, and (f) only bearded edges are plotted. For the armchair edge termination one does not find any zero-energy edge states as shown in Fig. 2.6(d). The dispersion curves of the zig-zag (Fig. 2.6(e)) and bearded termination of the lattice (Fig. 2.6(f)) exhibit the same bulk states but they differ in their zero-energy states. These edge states at the zig-zag edges (Fig. 2.6(e)) clearly exist in the outer regions of the BZ at $-\pi < k_x\tilde{a} < -\frac{2}{3}\pi$ and $\frac{2}{3}\pi < k_x\tilde{a} < \pi$. At the bearded edges (Fig. 2.6(f)) they are found in the center between $-\frac{2}{3}\pi < k_x\tilde{a} < \frac{2}{3}\pi$.

The existence of zero-energy edge states in graphene is directly related to the topological property of the Berry phase [28, 31, 35, 38]. Calculating the Berry phase along a closed loop in the k_y-direction for a certain value of k_x results in either $|\gamma| = \pi$ or $\gamma = 0$. It was shown that in the first case there exists an edge state at the certain value of k_x and in the second case not; this works equivalently for the k_x-direction to find an edge state at a certain k_y. Depending on how the unit cell is chosen, one can either make a statement for the armchair, the bearded or zig-zag edge state. The reason is that by using different unit cells one can describe different types of edges as graphically shown in Fig. 2.7. In the same way, as the winding number can be used to graphically calculate the Berry phase along a closed path around the Dirac points, it can be used to graphically calculate the Berry phase along a closed path in k_x-direction at a fixed k_y to determine the existence of an edge state at the respective k_y, or vice versa.

Since the existence of the zero-energy edge states is based on topological properties,

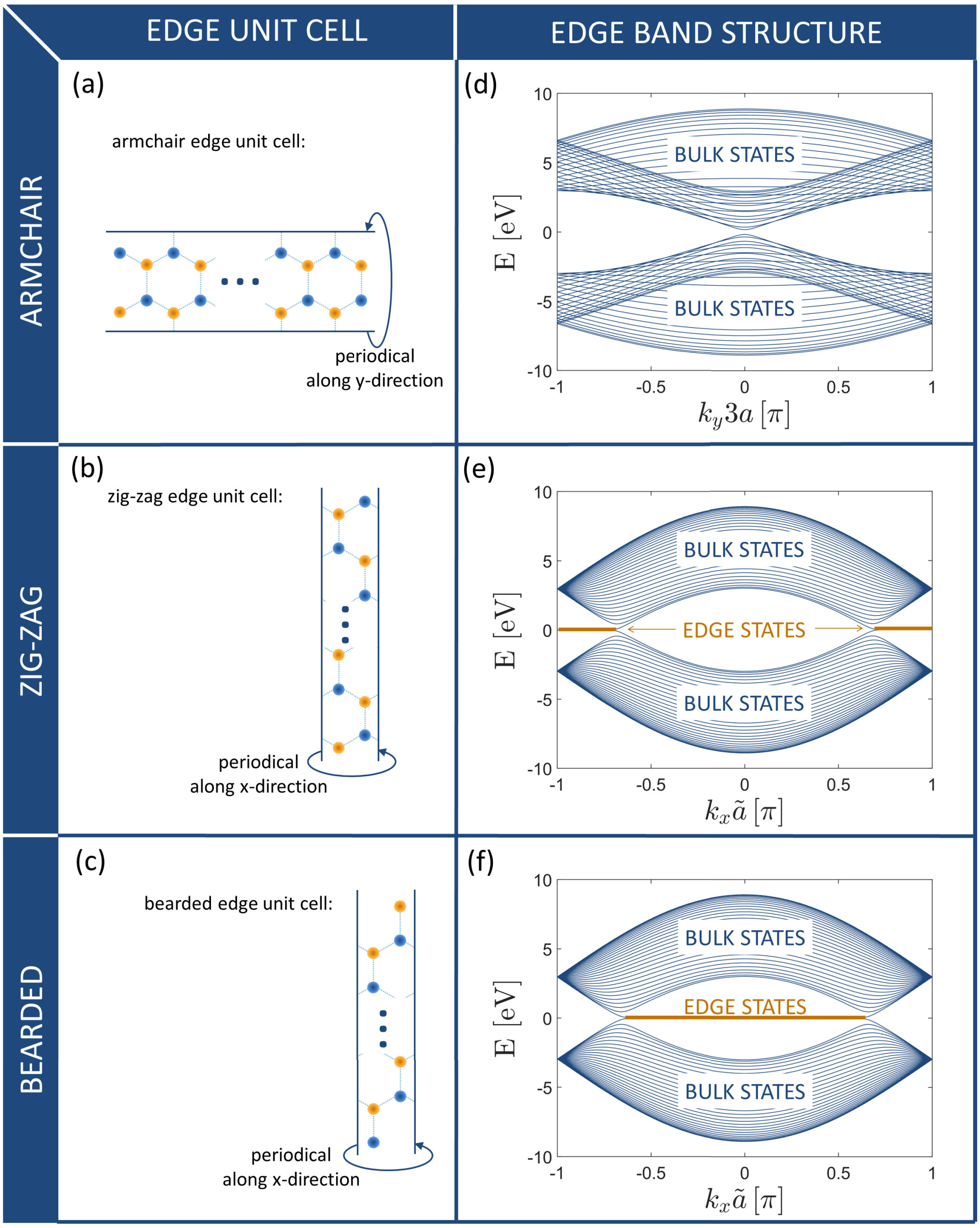

Figure 2.6: Left column: Edge unit cells being periodic in one direction and terminated in the transversal directon as applied to calculate an edge band structure. The different types exhibit three edge terminations: (a) armchair, (b) zig-zag, and (c) bearded edges. Right column: Associated dispersion curves of each semi-infinite lattice. (d) The armchair edge does not support any zero-energy edge states. (e) At the zig-zag edge, zero-energy edge states appear in the outer regions of the edge BZ, whereas (f) at bearded edges they are located in the center.

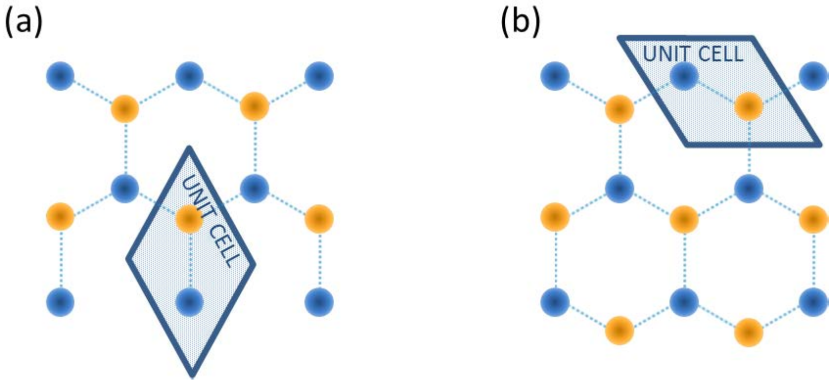

Figure 2.7: Choice of the unit cell to either take into consideration (a) bearded or (b) zig-zag edges along the x-direction via the bulk-edge correspondence, whereas along the y-direction in both cases an armchair edge is described.

they are extraordinarily resilient under perturbations respecting certain symmetries. For instance, disorder which respects chiral symmetry (i.e. off-diagonal disorder) does not destroy the edge states [39].

2.2.3 QUANTUM HALL EFFECT AND CHIRAL EDGE STATES

Chiral edge states are special conducting states at the surface of certain materials, which are insulators in the bulk. These states are immune against scattering at defects or due to disorder which leads to an extraordinary robust transport at the edges. An example where such states play a crucial role is the quantum Hall effect [24]. It is a quantum version of the Hall effect and occurs on surfaces where electrons can be described as a 2D electron gas. Therefore, extremely low temperatures and a strong magnetic field perpendicular to the electron gas are needed. In a very simple classical picture, the transport in the quantum Hall effect can be explained as follows: due to the magnetic field, applied perpendicular to the 2D electron gas, the electrons are forced along circular orbits, which leads to an insulating behavior in the bulk of the 2D electron gas. Though, at the edges, these circular orbits are interrupted leading to transport as pictured in Fig. 2.8. In measurements, a stepwise growth of the Hall resistance is found with increasing magnetic field while applying a constant current along the sample perpendicular to the measured Hall resistivity. Each conductance step

Figure 2.8: Sketch of the simple classical image of electron movement in the quantum Hall effect. In the center of the 2D electron gas a cyclotron movement along circular orbits lying perpendicular to the direction of the magnetic field is found, turning the bulk into an insulator. However, along the edge transport takes place since the circular orbits are disrupted by the edge.

arises because chiral edge states of the 2D electron gas yield charge transport [26,40,41]. The magnetic field splits the band structure into highly degenerate Landau levels with band gaps in between them. As long as the Fermi-energy lies in the gap, edge transport exists and the Hall resistance exhibits a plateau. These special edge states have no time-reversal partner at the same energy due to the magnetic field which breaks time-reversal symmetry. Hence, during their transport along the edge, they cannot be backscattered. In addition, they exist in the band gap and hence cannot be scattered into the bulk. Consequently, these edge states are very robust and can be attributed to a topological invariant [26,27]. By increasing the strength of the magnetic field, the Landau level landscape shifts. Each time, the Landau level coincides with the Fermi energy, a jump in the Hall resistance takes place. Once the Fermi energy lies in the subsequent band gap, again a topological edge state occurs. The correlation between the edge states and the topological invariant is reflected in the extremely robust step-height of the measured Hall-resistivity. This robustness turns the quantum Hall effect into one of the most special effects of solid-state physics [24].

Graphene-based observations of this effect have been proposed and experimentally realized in a number of works [9,42–45]. Interestingly, an entirely different manifestation of this effect was predicted in absence of an external magnetic field in 1988 [46]. Instead, a local periodic modulation of the magnetic field combined with the inclusion of next-nearest neighbor hopping lifts the degeneracy at the Dirac points. As a result, a band gap is opened in such a way that the usual edge states as described above turn into chiral edge states. Notably, this is the first example where such a quantum Hall state was predicted without any net magnetic flux through the unit cell of the lattice.

The idea of having chiral edge states without any external magnetic field at all was brought up by Kane and Mele in 2005 [47]. They showed that under certain conditions, which are based on strong spin-orbit coupling, chiral edge states can arise without the need of breaking time-reversal symmetry. Furthermore, these so-called topological insulators operate at room temperature. Interestingly, their theory was built up on a graphene structure. Shortly after this suggestion, it turned out that for a realization other materials are much better suited [48] and the first topological insulator finally was realized in 2006 [49]. They are predicted to have wide-ranging applications in fault-tolerant quantum computing and spintronics. Additionally, combined with superconductivity, these materials might support a new type of particles, i.e. Majorana fermions, which are of high interest in fundamental physics [50,51].

What all these approaches have in common, are gapped band structures with the Fermi-energy lying in a band gap comparable to ordinary insulators (along these lines, Landau levels in the quantum Hall effect are viewed as bands [50]). The difference to regular insulators lies in the mathematical structure of topology, which can be applied for these physical systems in the reciprocal space. In the considered cases, a topological class can be assigned to the bands. The corresponding topological invariant can assume integer values only and does not change under continuous deformations as long as the band gap remains open. At the interface between two band gapped media with different topological invariants, the gap has to be closed to neutralize the topological numbers. This happens by the formation of chiral edge states. In the quantum Hall effect and in topological insulators the interface is situated between the medium and its environment (i.e. air with its topological invariant being zero). The topological invariant which plays a role in the present work and in general for topological systems with broken time-reversal symmetry, is the first Chern number C. It is calculated via the Berry connection A (see Eq. (2.15)), and results from the total Berry flux in the BZ:

$$\mathcal{C} = \frac{1}{2\pi} \iint F(\vec{k}) \cdot d\vec{k}\,, \text{with the Berry flux} \quad F(\vec{k}) = \nabla_{\vec{k}} \times A(\vec{k}). \tag{2.20}$$

If there is more than one occupied band, the total Chern number of a material is achieved by summation over the Chern numbers of all occupied bands. Due to the fact that the arising of a chiral edge state is linked to a topological number, which can only change discretely, they cannot be destroyed under small adiabatic changes in the system parameters. That phenomenon is called "topological protection". In the quantum Hall effect this is the reason for the steps being so exact in height. Since the chiral edge state is the only way of transport in a topological insulator or a quantum Hall electron gas (with the bulk being an insulator) the resulting conductance is essentially independent from external perturbations.

In conclusion, when considering topology, it is important to separate between two cases: topologically trivial states and topologically non-trivial states. The edge states in classical graphene, without any external field applied to it, as described in Section 2.2.2 belong to the topologically trivial case. In fact, they can be described via a topological property (Berry phase) but the associated band structure cannot be classified by a topological invariant. In contrast, materials which support topologically non-trivial chiral edge states which are robust against scattering always have a gapped band structure which is classified by a non-zero topological invariant.

2.3 PHOTONIC WAVEGUIDE LATTICES

Many of the extraordinary features found in graphene, especially the Dirac like dispersion relation at the zero-energy point, are based on the very special honeycomb lattice structure. However, exactly this geometry can be realized in many other systems built up by a two-dimensional lattice going beyond atomic physics, as well. To examine the features of graphene and to have a tunable platform such artificial honeycomb lattices were implemented for electrons, atoms, acoustic waves [52] and photons of different wavelength regimes [53, 54]. Examples, beneath the one presented within this work, are photonic crystal slabs [55], microwave resonators [56], ultra-cold Fermi gases [57], molecular assemblies [58], polaritons [59], and optomechanical systems [60]. The present work deals with an optical system: coupled waveguides arranged in a honeycomb lattice being also termed "photonic graphene". Such a structure was for the first time realized in 2007 in the context of the observation of lattice solitons [61]. Using the light propagation in such a lattice, one is able to emulate the temporal evolution of an electronic wavefunction in real graphene. From an experimental point of view, the optical system yields a much easier access since the light evolution can directly be observed. Furthermore, certain effects, based on, e.g., strong strain, a perfect structure without disorder, pre-defined disorder, or pre-defined edge terminations of the lattice, are not or hardly accessible in real graphene. Whereas, in the photonic system, all these features can easily be generated during fabrication of the lattice. Here, one has many degrees of freedom in designing the lattice; even negative couplings have already been implemented in waveguide arrays [62,63]. Moreover, also one-dimensional Dirac physics has been examined in coupled waveguide systems, both for the massless Dirac equation [64] and for the massive one [65,66].

In this section, the mathematical description of light propagation in such an array of waveguides is derived. Furthermore, coupled mode equations, being a simplified but often sufficient model to describe the amplitude distribution along the lattice, are introduced. They represent the equivalent to the tight-binding model in the atomic structure. At the end, photonic graphene, its fabrication, as well as the used measurement setups will be explained.

2.3.1 LIGHT PROPAGATION IN WAVEGUIDE ARRAYS

PARAXIAL HELMHOLTZ EQUATION. A way to describe the light propagation in an array of waveguides mathematically is the paraxial Helmholtz equation [67,68]. To derive it, one can make several approximations starting from the wave equation describing light propagation in dielectric media in general:

$$\left(\nabla^2 - \frac{n^2}{{c_0}^2}{\partial_t}^2\right)\vec{E}(x,y,z,t) = 0, \tag{2.21}$$

with the vacuum speed of light c_0 and the refractive index $n = n(x,y,z)$. Since we will consider a waveguide array, the propagation direction z is different from the transverse directions $\vec{r} = (x, y)$. Substituting the monochromatic plane wave ansatz in Eq. (2.21) and taking into account only one scalar component of the electric field leads to

$$\left(\nabla^2 + 2ik\frac{\partial}{\partial z} - k^2 + \frac{n^2\omega^2}{{c_0}^2} \right) \psi(\vec{r}, z) = 0. \tag{2.22}$$

Here, $\psi(\vec{r}, z)$ is the electric field envelope function defined by $E(\vec{r}, z) = \psi(\vec{r}, z)\mathrm{e}^{i(kz-\omega t)}$ with ω being the angular frequency of the wave propagating along z-direction. Assuming only adiabatic variations along z, the second derivative in z in the above equation can be neglected. Now the refractive index profile of the waveguide array embedded in a bulk material with refractive index n_0 comes into play with $n = n_0 + \Delta n(\vec{r}, z)$. Due to the fact that the refractive index landscape of the waveguides shall only vary very slightly around the bulk index ($\Delta n << n_0$), the assumptions $n^2 \approxeq {n_0}^2 + 2n_0\Delta n(\vec{r}, z)$ and $k \approxeq k_0 = \frac{n_0\omega}{c_0}$ are justified. This leads to the paraxial Helmholtz equation

$$i\partial_z\psi(\vec{r}, z) = -\frac{1}{2k_0}{\nabla_T}^2\psi(\vec{r}, z) - \frac{k_0\Delta n(\vec{r}, z)}{n_0}\psi(\vec{r}, z). \tag{2.23}$$

Here, ∇_T only acts on the x and y components of ψ. Interestingly, this equation has the same mathematical structure as the temporal Schrödinger equation in two dimensions x and y, with the z-component here being equivalent to the temporal component. Please note, that in the above derivation the z-component is the propagation direction. Furthermore, the potential term in Eq. (2.23) has a negative sign instead of a positive sign as found in the Schrödinger equation. But for photons, an increase in the refractive index being here the analogue to the potential, acts attracting, whereas for atoms a decrease of the potential acts attracting. Hence, the opposite sign exactly holds up the analogy of the two equations. Of course, the filling of the potential well is different since photons are bosons, but the transversal supermodes of the waveguide structure can be seen equivalently to a bound eigenstate of the potential. In summary, the Schrödinger-like structure of the paraxial Helmholtz equation (Eq. (2.23)) is the reason for the comparability between such different systems as atomic and photonic lattices. A more simplified way to describe only the propagation of amplitudes along the waveguides of the lattice will be given in the next section.

COUPLED MODE EQUATIONS. In the context of this thesis, a waveguide will always be built up by a refractive index profile supporting the fundamental mode solely. The guided light is not completely constricted to the area of refractive index increase but exhibits exponential decay into the surrounding bulk material - the so-called evanescent field. Similar to the tunneling effect in quantum mechanics, this evanescent field can lead to a transfer of energy to surrounding waveguides - its strength being exponentially dependent on the distance. The amplitude behavior cannot only be calculated by Eq. (2.23), but often a simpler description is sufficient: the coupled mode equations. The condition therefor is that the waveguides are separated in a way that the mode amplitude of each waveguide is not remarkably modified by the adjacent guides. In that case, the overall wavefunction can be expressed as a superposition of the individual wavefunctions of each waveguide. To describe the propagation of the amplitude of the guided mode ϕ_n in the n-th waveguide one can then find the following set of coupled differential equations [69]:

$$i\partial_z\phi_n(z) = -\sum_m C_{n,m}\phi_m(z) - k_n\phi_n(z). \tag{2.24}$$

The symmetric coupling matrix $C_{n,m}$ consists of the coupling coefficients between pairs of waveguides describing the energy transfer between them. It is given by the overlap of the mode fields $\varphi_n(\vec{r})$ and $\varphi_m(\vec{r})$ with the dielectric function ε [70]:

$$C_{n,m} = \iint\limits_{-\infty}^{+\infty} \varepsilon(\vec{r})\varphi_n(\vec{r})\varphi_m^*(\vec{r})\,d\vec{r}\,, \text{with} \quad \varepsilon^2 = \Delta n(\vec{r}). \tag{2.25}$$

The propagation constants k_n of the individual waveguides are obtained by:

$$k_n = \iint\limits_{-\infty}^{+\infty} \varepsilon(\vec{r})|\varphi_n(\vec{r})|^2\,d\vec{r}\,, \text{with} \quad \varepsilon^2 = \Delta n(\vec{r}). \tag{2.26}$$

The coupled mode equations (2.24) are exactly the same approach for the waveguide lattice as the tight-binding model is for an atomic lattice. Instead of the hopping parameter one finds the coupling parameters and the mass of the atom in the waveguide array is substituted by the propagation constant k_n which can be varied from waveguide to waveguide. This together with the possibility of varying the distances between the waveguides offers degrees of freedom not available in an atomic lattice. The analogy allows to implement a tight-binding model of graphene in a honeycomb lattice of

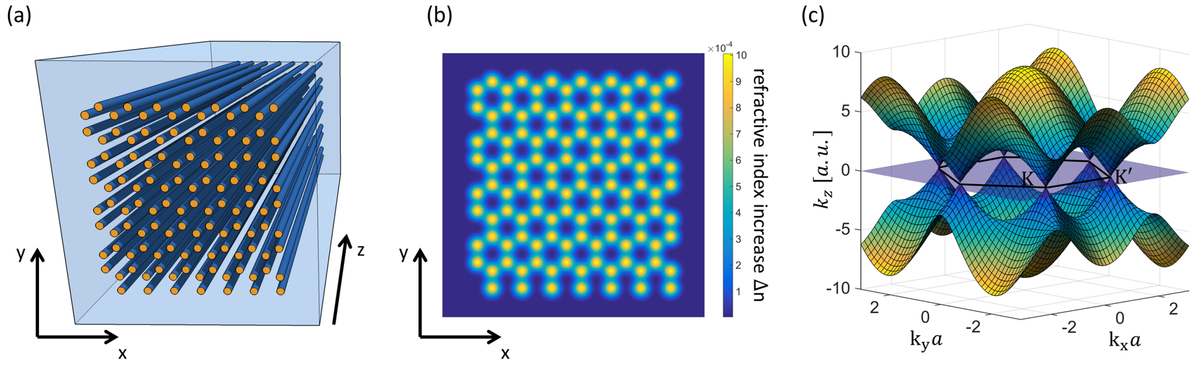

Figure 2.9: (a) Sketch of the photonic graphene lattice consisting of waveguides arranged in a honeycomb lattice. (b) Exemplary refractive index increase profile of such a lattice for calculating the light propagation with the paraxial Helmholtz equation. (c) Tight-binding band structure of photonic graphene.

waveguides described by coupled mode equations. Hence, in the same manner as the Bloch band structure of the atomic lattice is derived from the tight-binding model, the Bloch band structure of the waveguide array can be achieved.

2.3.2 PHOTONIC GRAPHENE

This section will characterize the basic honeycomb waveguide lattice used within this thesis and will give an idea about the dynamics of the light propagation in it, which was in general mathematically derived in the last section.

The here used photonic lattice consists of waveguides arranged in the same structure as the atoms in the graphene lattice and is called photonic graphene. A sketch of the structure is shown in Fig. 2.9(a). The waveguides themselves are embedded in a fused silica bulk material, which has a refractive index of $n_0 = 1.45$ at a wavelength of $\lambda = 633\,\text{nm}$. There is a smooth increase of refractive index building up the waveguides which reaches its maximum in their center with about $\Delta n = 10^{-3}$. An exemplary refractive index increase profile $\Delta n(\vec{r})$ of a lattice as sketched in Fig. 2.9(a) is depicted in Fig. 2.9(b). Here, each waveguide is characterized by a Gaussian profile. If this refractive index distribution is inserted in Eq. (2.23), the propagation of the wavefunction in photonic graphene along the z-direction can be calculated from the initial wavefunction (for more details see Appendix). Furthermore, due to the structural equality of the paraxial Helmholtz equation and the Schrödinger equation, the propagation in photonic graphene corresponds to the wavefunction propagation in time in a graphene lattice. The refractive index profile of the waveguides takes then the place of the potential in graphene originating from the atomic lattice. If only the propagation of the amplitudes in each waveguide is taken into account, one can use Eq. (2.24) to describe the so-called discrete diffraction in photonic graphene. To further simplify the equations, in a good approximation only nearest neighbor interaction is considered. If all waveguides are identical, additionally the propagation constants k_n can be set equal for all n and normalized out. To find the static solution of the coupled mode equations, a plane wave ansatz $\phi_n = \Psi_n \mathrm{e}^{-i(k_z z)}$ is employed. This leads to the eigenvalue equation for the static solutions:

$$k_z \Psi_n = -\sum_{\langle m \rangle} c_{n,m} \Psi_m \equiv H_{m,n} \Psi_m, \tag{2.27}$$

where the summation is only taken over nearest neighbours and $c_{n,m}$ is the coupling constant between the n-th and m-th waveguides. For an infinite lattice Bloch's theorem can be applied, leading to the same Bloch Hamiltonian as defined for graphene in Eq. (2.5). Hence, the solutions of Eq. (2.27) in reciprocal space can be calculated to plot the tight-binding band structure of the honeycomb waveguide array (Fig. 2.9(c)). The only difference to the band structure of graphene (Fig. 2.3) is that in the waveguide array, the energy is replaced by the propagation constant k_z. It becomes clear that the tight-binding modell of the atomic lattice is equivalent to the coupled mode description of the waveguide array. In the context of this thesis, only single-mode excitations and hence, the first dispersion bands will be of interest.

To get an imagination about the dynamics of light spreading in a coupled waveguide lattice, it is helpful to plot the amplitude propagation according to Eq. (2.24) while only taking into account nearest neighbour coupling coefficients. Compared to a homogeneous medium, where a narrow wave packet diffracts continuously, here discrete diffraction is present. The smallest excitation, one can realize in photonic graphene, is launching light into one single waveguide as shown in the simulation of the propagation in Fig. 2.10(a). It can be seen that during propagation the light spreads throughout the lattice, exhibiting the 3-fold rotational symmetry of the honeycomb

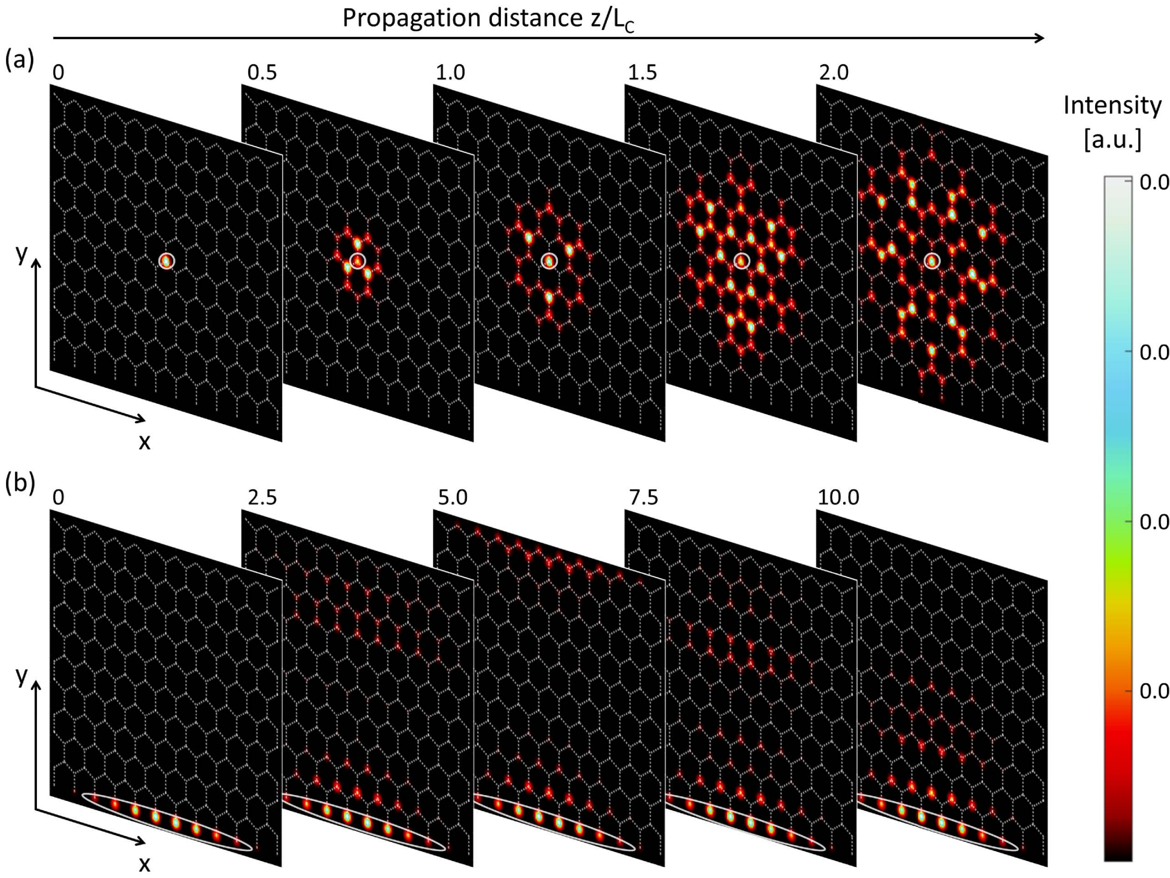

Figure 2.10: Coupled-mode simulation of the light propagation in photonic graphene with (a) excitation of a single waveguide in the center and (b) excitation with an elliptically shaped beam at the bearded edge of the lattice. The excitation region is marked by the white circle and ellipse, respectively. The propagation distance is plotted in units of the coupling length $L_C = \pi/2c$. Please note, that each cross section has been normalized with respect to its maximum value for better visibility.

structure. This narrow excitation in real space corresponds to a broad excitation of the whole BZ in momentum space. In contrast, if an infinitely broad wave packet is launched into the array by choosing a certain wave vector $\vec{k} = (k_x, k_y)$, one can specify the excitation point in the BZ. In reality, of course no infinitely broad wave packet is available, but in most cases it is sufficient to launch light into a region of a few waveguides to get a small excitation in reciprocal space. This is exactly what is done if an edge state as described in Section 2.2.2 is excited. A broad wave packet excitation in x-direction with a wave vector around $k_x = 0$ at the bearded edge (and with a wave vector around $k_x = \pm\pi/\tilde{a}$ at the zig-zag edge, respectively) excites an edge state. Hence, an elliptical beam (with the main axis of the ellipse in x-direction and the small axis in y-direction) is launched into the lattice as shown by a simulation of the propagation using Eq. (2.24) with nearest-neighbour coupling only in Fig. 2.10(b). Here, the part of the excited light which possesses perfect overlap to the edge state stays at the edge during propagation and the other, smaller part of the light, which possesses overlap with bulk modes moves into the lattice bulk. To understand the connection between the dispersion relation and the behaviour of the light propagation, it is helpful to look at the edge dispersion as plotted in Fig. 2.6 (for the waveguide array the energy has to be replaced by k_z). Here can be seen that the edge state exhibits a flat dispersion in momentum space ($k_z^{\text{edge state}}(k_x) = 0$). Since the first derivative of the dispersion relation is equal to the group velocity, the edge state does not move in the transverse direction during propagation. Furthermore, the second derivative, corresponding to the diffraction, also yields zero. Hence, the edge state does not broaden during propagation as shown in Fig. 2.10(b). In general, within this work edge states in photonic graphene will play a major role exploring the rich dynamics of the system.

In summary, this section showed that the properties of graphene described in Sections 2.1 and 2.2 are also valid in photonic graphene. Furthermore, many features of real graphene can be assigned to the photonic system: e.g., the existence of edge states, the single particle dynamics described by the Schrödinger equation (being equivalent to the paraxial Helmholtz equation), the tight-binding description (being equivalent to the coupled mode description), and the respective band structure. Though, in the accession to the band structure also lies a wide difference. In graphene, by tuning the

Fermi energy the particle dynamics exhibit a certain dispersion, whereas in photonic graphene one can tune the k_x and k_y component of the exciting wave packet but not easily the k_z component.

In general, photonic graphene offers degrees of freedom which are not or not readily accessible in real graphene. In photonic graphene, the coupling parameters being exponentially dependent on the distance between waveguides can be tuned easily as will be shown in the description of the fabrication in the next section. Adding a strain to the lattice is possible in both systems, but in real graphene it is much more sophisticated and cannot be completely predetermined [71]. However, in the waveguide lattice, a strain of the lattice can be designed almost arbitrarily, the only limitation is that the waveguides may not overlap. Furthermore, realizing the different edge types and accessing the edge states is much easier than in real graphene where edge states can be examined via scanning tunnelling microscopy [72,73]. Especially, an extended bearded edge was only realized recently in real graphene [74] since it lacks stability due to its dangling bonds. Whereas photonic graphene enabled the discovery of a new edge state at the bearded termination [75]. It arises at the van-Hove singularity and is not present in simple tight-binding analysis. Moreover, in contrast to real graphene also the two basically different kinds of disorder (on-diagonal/structural and off-diagonal/coupling disorder) can be implemented in a predefined way in the photonic system. This led to the insight that pronounced Anderson localization appears if the lattice is excited around the Dirac points [76] and it was shown that the edge state stability is strongly dependent on the type of disorder [39]. Altogether, this thesis will show different effects realized within photonic graphene going beyond the possiblities of real graphene.

2.3.3 WAVEGUIDE FABRICATION

The practical realization of photonic graphene hinges upon the capability to implement three-dimensional waveguide lattices. The first honeycomb photonic lattice was realized by optical induction in a nonlinear medium [61]. This system was created by the interference of three plane waves in a photosensitive material. However, the technique only allows to realize strictly periodical structures without any modulation along the z-direction. Furthermore, arbitrary pre-defined edge terminations are difficult or rather impossible to implement. Within this thesis, a different method called femtosecond direct laser writing will be employed. In comparison to the induction technique, the here used lattices have the following major advantages: they are permanent, defects and certain edge terminations can easily be implemented. Additionally, arbitrary strain and variations along the propagation direction can be realized.

Femtosecond direct laser writing leads to a modification of the refractive index in certain transparent media. The intense exposure of femtosecond laser radiation (usually realized by focussing the beam) leads to nonlinear absorption in the material. Hence, a local energy deposition takes place resulting in a permanent change of the refractive index [77]. In the fused silica samples, used within this work, these processes lead to a change in the amorphous ring structure of the material. After the intense laser radiation smaller molecular rings with higher packing densities are found in the modified regions [78,79]. Consequently, the local refractive index is increased. Writing an extended waveguide with this technique is realized spot by spot. For that purpose the sample is moved along the propagation direction of the waveguide as shown in Fig. 2.11(a). After the discovery of this technique in 1996 [80], it was brought forward to write extended three dimensional waveguide structures with almost arbitrary shape in fused silica [81].

The photonic graphene lattices, used within the experiments in this thesis, were inscribed with a Ti:Sapphire laser system (Coherent Mira 900F/ RegA 9000) with a pulse energy of approximately 250 nJ, and a repetition rate of 100 kHz at a wavelength of 800 nm. The pulses with a length of approx. 160 fs were focused in a fused silica sample (Corning®HPFS®7980) with a 20× microscope objective with a numerical aperture of 0.35. To realize the waveguide extension along the propagation direction, the sample, being placed on a computer controlled translation stage (Aerotech ALS 130), was moved continuously with velocities between 1 and 2 mm/s. While all other parameters are fixed, the writing velocity allows to define the amount of energy replaced in the sample. This enables the control of the change in refractive index being higher for lower writing velocities and vice versa. A typical refractive index change acting as waveguide is

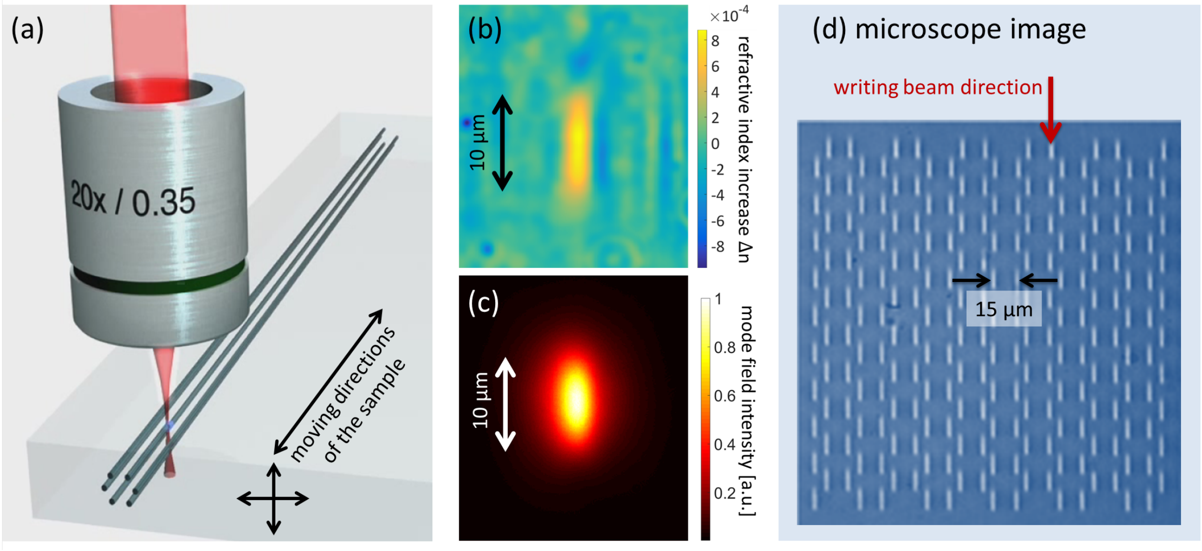

Figure 2.11: (a) Fabrication of photonic graphene by femtosecond direct laser writing. (b) Refractive index increase profile of one waveguide calculated from the mode profile at a wavelength of 633 nm as shown in (c). (d) Transmitted light microscopic image of the end facet of a honeycomb waveguide lattice.

plotted in Fig. 2.11(b). It was calculated by numerical inversion of the Helmholtz equation from the mode profile at 633 nm as shown in Fig. 2.11(c) [82]. This method is well-suited to get a good approximation of the refractive index contrast and its general shape. However, noise in the experimentally achieved image of the mode profile has a strong effect on the calculation leading to uncertainties of approximately $\pm 0.15 \times 10^{-4}$ in the vicinity of the waveguide cores.

The coupling parameter between waveguides is mainly determined by their distance. It changes only slightly within the applicable writing velocities. The nearest neighbor separations between waveguides in the regular honeycomb lattices used within this thesis were in the range of $14\,\mu\text{m} - 22\,\mu\text{m}$ in order to achieve the desired coupling strengths of $2\,\text{cm}^{-1} - 0.2\,\text{cm}^{-1}$, respectively. A microscopic image of the front facet of an exemplary photonic graphene lattice is shown in Fig. 2.11(d). As can be seen in the refractive index increase profile (Fig. 2.11(b)) and in the microscopic image of a photonic graphene lattice (Fig. 2.11(d)), the waveguides are elongated along the direction of the inscription beam. The elliptical cross section leads to a slight difference in the vertical and horizontal coupling parameter, which could be compensated. However, stronger focussing would increase the spherical aberrations and thereby lead to a depth dependence of the refractive index - clearly a not desirable trade-off for the task at hand. To ensure the quality of the experimental results a high degree of homogeneity of the waveguides across large lattices is required.

In summary, femtosecond direct laser writing enables the realization of very complex lattice geometries as will be presented in the following chapters. This includes the implementation of even intricate types of strain of the photonic graphene lattice. Furthermore, within this thesis waveguides with a periodical helical modification along the propagation direction were realized for the first time.

2.3.4 MEASUREMENT TECHNIQUE

Although the realization technique of the structure itself is a highly complex process, the focus here is on the influence of a certain lattice geometry on the propagation of light through it. All of the presented experiments are based on the honeycomb waveguide lattice. However, in each experiment the basic structure is modified in order to achieve certain effects. Consequently, the light propagation in these lattices differs to the one in regular photonic graphene. The applied experimental measurement techniques to observe this behavior are described within this section.

Initially, the sample with the waveguides inscribed in it, is mounted on an xyz linear translation stage. To excite certain waveguides, a particular light distribution is shined into the input facet. If not stated otherwise, the wavelength of the exciting light is 633 nm, generated by a conventional HeNe-laser. In the context of this work two different input shapes were applied:

(i) A single waveguide excitation is achieved by passing the light from the HeNe source through a fiber with a mode diameter being matched to an individual waveguide. The fiber is placed directly at the input facet (schematically depicted in Fig. 2.12(a)). This point-like excitation in position-space corresponds to a broadband excitation in reciprocal space. Hence, with this technique, not a certain position of $\vec{k}$ can be addressed but the whole spectrum.

(ii) The second kind of input shape is an elliptical beam profile as shown in Fig. 2.10(b).

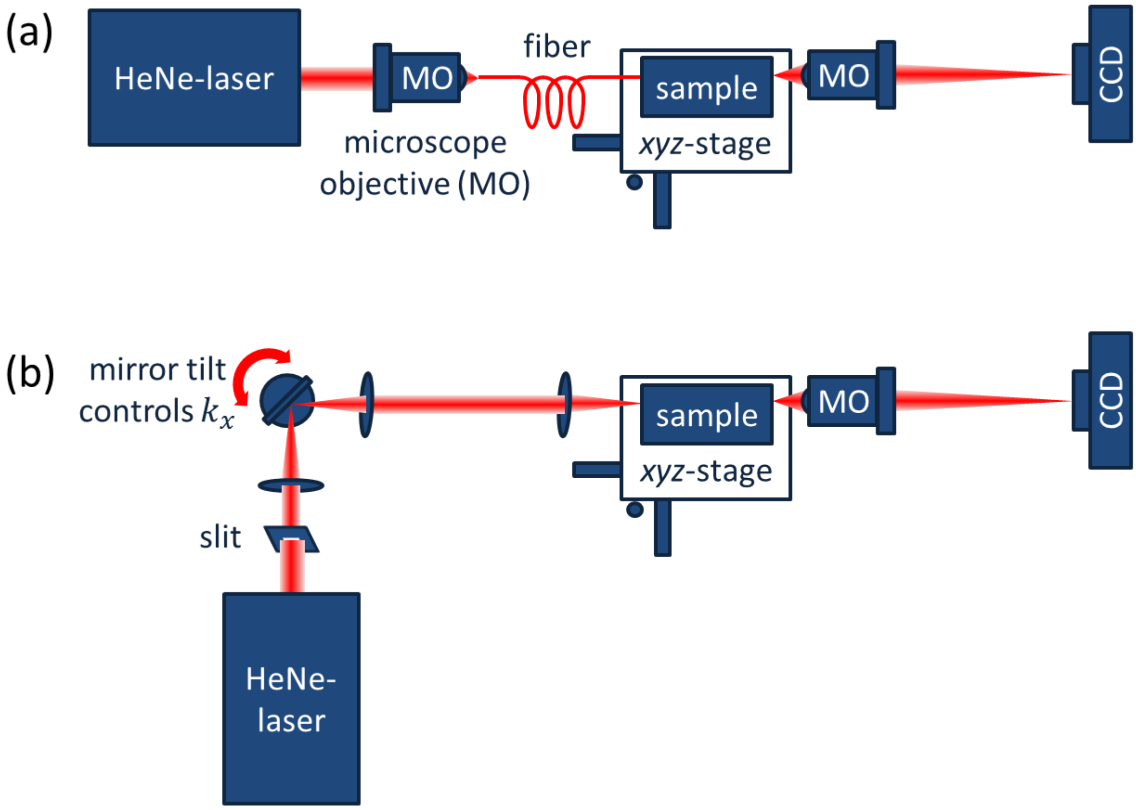

Figure 2.12: Scheme of the measuring setup to image the light distribution at the output facet of the sample. (a) Single waveguide excitation by placing a fiber directly at the input facet of the sample. (b) Setup to generate an elliptically shaped beam (with main axis along x). Its phase k_x can be varied via a tilt of a mirror onto which the beam profile is focused after being cut out by a slit aperture. Subsequently the elliptical beam is imaged onto the input facet of the sample.

> The main axis of the ellipse lies along the x-axis and has a length of approx. 80 µm, whereas the small axis lies along the y-axis and covers approx. 20 µm. To synthesize the elliptical profile experimentally, first a slit aperture is brought in the Gaussian beam profile of a HeNe-laser. Subsequently, the beam is focused onto a tiltable mirror with which the k_x component of the phase of the ellipse can be varied. Afterwards the beam, with a particular phase k_x imprinted on it, is imaged onto the input facet of the sample using a 4f-system (two identical lenses with a distance of twice their focal length). This beam profile allows a narrow-band excitation in the k_x direction. Furthermore, a large part of the elliptical beam profile coincides with an edge eigenstate allowing to mainly excite an edge state. As a consequence, this yields the possibility to directly address each k_x separately in the edge band structure (Fig. 2.6). Taken together, by applying a linear phase gradient in the x-direction, this technique enables a "spatial spectroscopy"on the edge.

The next step in the experiments is the most important one. According to the respective design of the lattice geometry, the injected light diffracts in the sample and a certain output light distribution is generated. The structure of the different lattices, used within this work, and its effect on the light dynamics are the topic of the following chapters. Though, in all cases, the technique to visualize the light distribution at the output facets of the samples is equal. First, an enlargement by a microscope objective is employed and subsequently the image is acquired using a CCD camera as shown in Figs. 2.12(a) and (b).

The above measurement technique with single waveguide excitation was established during many former experiments [83–86]. The broad elliptical excitation yields a well-suited expansion of this technique, enabling the edge state probing in the honeycomb geometry. In general, the light dynamics during propagation in the sample cannot be directly measured with this technique. To overcome this problem, either samples of different lengths have to be fabricated or the sample has to be cut several times, each time after the measurement was performed. A similar effect can also be achieved by fabricating several lattices while varying the coupling coefficients or certain parameters defining the strength of the effect which is supposed to be demonstrated. Another, yet elegant way, is to use different excitation wavelengths, resulting in a variation of the coupling strength between waveguides. As an example, a shorter wavelength leads to smaller coupling strengths, with results being comparable to the ones of a shorter propagation distance. In summary, the utilized techniques enable a stable way to probe the effect of the sample geometry on the light propagation and are used in all experiments presented within this thesis.

3

EDGE STATE TRANSITION CAUSED BY COMPRESSION

In physics, the main reason for strong interest in topological properties is their robustness under perturbations. If a topological property changes one talks about a topological phase transition, which by definition is discrete. This section will show theoretically and experimentally a topological phase transition in photonic graphene. To achieve this, a strong linear strain is applied to the lattice, which is beyond the attainable strain levels in carbon-based graphene [87]. A compression of the lattice will lead to a transition from an ungapped phase with two unique Dirac points, to a phase where the Dirac points have merged and a band gap opens [31,88]. This results from the geometry of the honeycomb lattice only, and hence is general. As described in Section 2.2.1, the Dirac points can be characterized by a topological property, the Berry phase. Encircling each of the two unique Dirac points, one finds a Berry phase of π and $-\pi$, respectively, which is topologically protected against small strains or compressions preserving inversion symmetry. The linear compression of the lattice, as employed in this section, indeed preserves inversion symmetry. It leads to a shift of the Dirac points in the reciprocal lattice and at a certain threshold that corresponds to the merging of the two Dirac

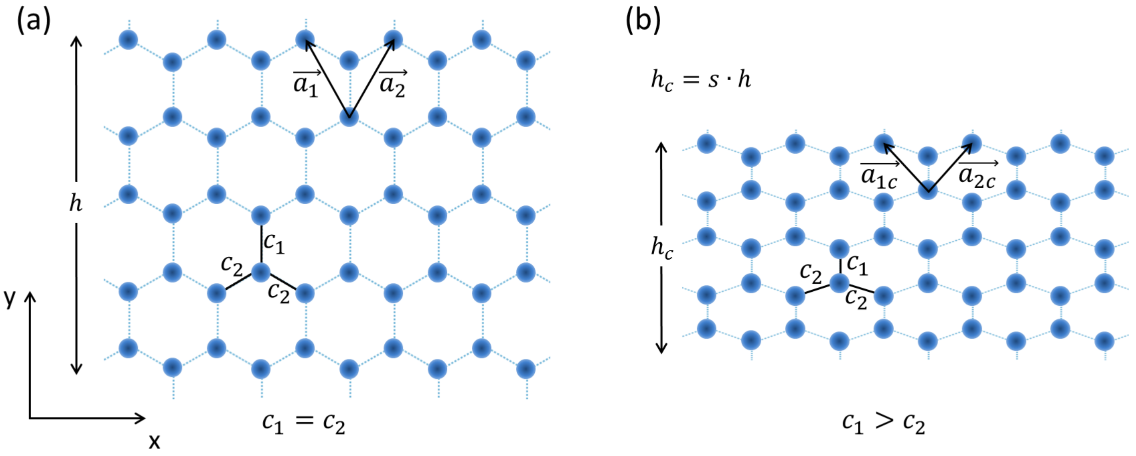

Figure 3.1: Configuration of the waveguides in the case of the (a) uncompressed honeycomb lattice with strain factor $s = 1$ and (b) the linearly compressed lattice with strain factor $s = 0.6$. This increases the ratio of the vertical coupling c_1 to the diagonal coupling c_2.

points a topological transition takes place and a bulk band gap is opened. This process correlates with an edge state transition, which will be demonstrated experimentally.

3.1 TOPOLOGICAL PHASE TRANSITION

To achieve the topological phase transition, the honeycomb lattice is strained in a certain manner. As shown in Fig. 3.1, a linear compression along the y-direction of the lattice is applied. The strain factor s describes the ratio of the heights of the compressed lattice to the uncompressed one being $s = \frac{h_c}{h}$. Hence, this kind of strain does not destroy periodicity, neither in x-, nor in the y-direction. It leads to a change of the y-components of the primitive translation vectors $\vec{a}_{1c} = \frac{a}{2}\left(-\sqrt{3}, 3s\right)$ and $\vec{a}_{2c} = \frac{a}{2}\left(\sqrt{3}, 3s\right)$. The compression modifies both the vertical c_1 and diagonal couplings c_2, but it increases c_1 stronger than c_2. The reason for that is an exponential dependence of the coupling parameter c on the distance d defined by $c(d) = c_0 \mathrm{e}^{-(d-a)/l_0}$, where a is the nearest-neighbour spacing of the unstrained honeycomb lattice, l_0 is the coupling decay length, and c_0 is the coupling strength at $d = a$. Hence, the ratio between the vertical and diagonal coupling is connected to the strain factor as follows:

$$\frac{c_1}{c_2} = \mathrm{e}^{\frac{a}{l_0}\left(\frac{1}{2}\sqrt{3+s}-s\right)}. \tag{3.1}$$

Based on the changes in the lattice geometry, the effects in reciprocal space can be examined. To calculate the changes in the band structure, Eq. (2.6) is written down inserting the above lattice vectors which include the strain:

$$\begin{aligned}\tilde{S}(\vec{k}) &= c_1 + c_2\left(\mathrm{e}^{-i\vec{k}\vec{a}_{1c}} + \mathrm{e}^{-i\vec{k}\vec{a}_{2c}}\right) \qquad (3.2)\\ &= c_1 + c_2\left[2\cos\left(\frac{\sqrt{3}}{2}ak_x\right)\cos\left(\frac{3}{2}ak_y s\right) - 2i\cos\left(\frac{\sqrt{3}}{2}ak_x\right)\sin\left(\frac{3}{2}ak_y s\right)\right].\end{aligned}$$

Applying this result, the dispersion relation of the compressed photonic graphene lattice can directly be calculated as $k_z = |\tilde{S}(\vec{k})|$, leading to:

$$k_z = \pm\left[c_1^2 + 4c_1c_2\cos\left(\frac{\sqrt{3}}{2}ak_x\right)\cos\left(\frac{3}{2}ak_y s\right) + 4{c_2}^2\cos^2\left(\frac{\sqrt{3}}{2}ak_x\right)\right]^{1/2}. \tag{3.3}$$

The above equation allows to describe the effect of the strain in reciprocal space. To get an imagination about the changes of the band structure under the compression, one of the two bands (the two bands are positioned symmetrically around zero) is shown in a color plot in Fig. 3.2. The uncompressed lattice in Fig. 3.2(a) exhibits the six Dirac points arranged in a regular hexagon corresponding to Fig. 2.3. Each two of the Dirac points with different Berry phase approach under compression, their moving direction is marked by the white arrows. Figure 3.2(b)-(d) shows the reciprocal lattice for increasing compression of the real lattice. Exactly at $c_1/c_2 = 2$ each two Dirac points merge (Fig. 3.2(c)). For larger coupling ratios ($c_1/c_2 > 2$) a band gap is opened as shown in Fig. 3.2(d) and (e). In the latter a 3D-plot of both first bands is shown for $c_1/c_2 = 2.5$ for better visualization of the strain induced band gap opening. The merging of the two inequivalent Dirac points constitutes a topological transition. Exactly at that point, the Berry phases $\pm\pi$ associated with the Dirac points annihilate. Although this transition is a bulk property and independent of the edge terminations of the lattice under appropriate choice of the edges it is directly connected to an edge state transition.

As described in Section 2.2.1, the presence of edge states in the honeycomb lattice can analytically be derived via an indirect calculation of the Berry phase. For that purpose,

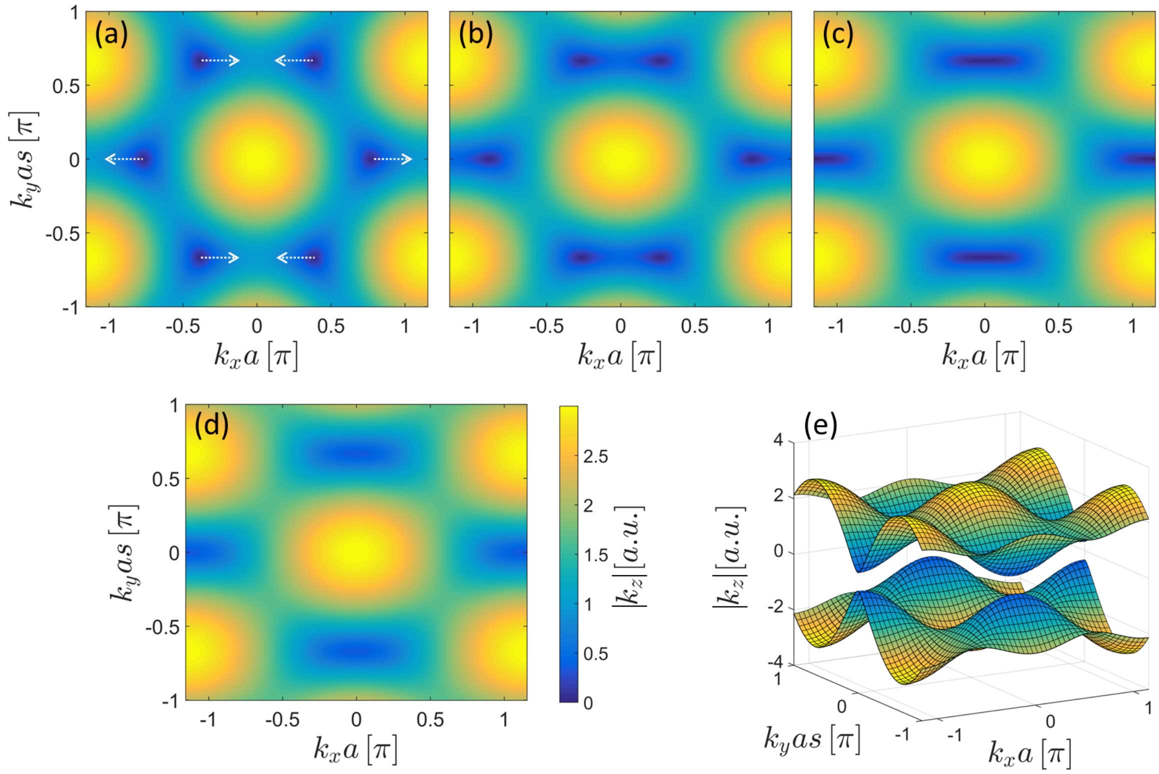

Figure 3.2: Color plot of $|k_z|$ over the extended BZ of the honeycomb lattice for different coupling constant ratios. (a) Uncompressed lattice with $c_1/c_2 = 1$ with six Dirac points visible. The white arrows depict the movement of the Dirac points under compression of the lattice. (b) The Dirac points have moved and each two of them have approached for $c_1/c_2 = 1.5$. (c) If the vertical coupling c_1 is exactly double the diagonal coupling c_2 the Dirac points merge. (d) For larger coupling ratios (here $c_1/c_2 = 2.5$) a band gap is opened. To better see the band gap, a respective 3D-plot of both first bands is shown in (e).

the vector $\vec{h}(\vec{k})$ (defined by Eq. (2.16)), more precisely its winding number along a closed loop in the BZ is evaluated. Note, that depending on the choice of the unit cell this yields a statement about the existence of an edge state at either the bearded or the zig-zag edge (see also Fig. 2.7). The above defined primitive translation vectors, applied to calculate $\vec{h}(\vec{k})$, are chosen such that a bearded edge termination can be described and lead to:

$$\begin{aligned}\vec{h}(\vec{k}) &= \left(\Re e\left[\tilde{S}(\vec{k})\right], -\Im m\left[\tilde{S}(\vec{k})\right]\right) \qquad (3.4)\\ &= \left(c_1 + 2c_2\cos\left(\frac{\tilde{a}}{2}k_x\right)\cos\left(\frac{\sqrt{3}\tilde{a}s}{2}k_y\right), 2c_2\cos\left(\frac{\tilde{a}}{2}k_x\right)\sin\left(\frac{\sqrt{3}\tilde{a}s}{2}k_y\right)\right).\end{aligned}$$

The winding number of $\vec{h}(\vec{k})$ along a closed loop in the k_y-direction at a fixed k_x reveals the existence of an edge state at the respective value of k_x. For a complete winding of $\vec{h}(\vec{k})$ along a closed path in reciprocal space, the Berry phase is equal to $\pm\pi$. Hence, in this region an edge state is present. Whereas for incomplete windings of $\vec{h}(\vec{k})$, the Berry phase is zero and thus no edge state exists. In Fig. 3.3, the directions of the vector $\vec{h}(\vec{k})$, calculated from Eq. (3.5), are plotted as arrows for a grid of points in the reciprocal space. The blue dots indicate the Dirac points as a guide to the eye. The diagram is plotted for the bearded edge, when it is repeated in the x-direction but terminated in the y-direction. Following the derivation in Section 2.2.1, the Berry phase can directly be read out of this arrow plot. Figure 3.3 (a) shows the directions of $\vec{h}(\vec{k})$ for an uncompressed honeycomb lattice. In the shaded regions $\vec{h}(\vec{k})$ makes a closed loop along the k_y-direction as it can be seen from the arrows. Thus, here the Berry phase equals $\pm\pi$ indicating the existence of edge states at the respective values of k_x. In the white regions, the arrows do not undergo a complete loop along a closed path in the k_y-direction revealing that there is no edge state present. In the center of the first BZ, a bearded edge state is present, while in the outer third no edge state is found. This is in full agreement with the statements derived in Section 2.2.2. Figure 3.3 (b) shows the case of strong compression ($c_1/c_2 = 2.5$), where a bandgap has emerged. Here, in the complete BZ the bearded edge states have been eliminated since $\vec{h}(\vec{k})$ for every k_x undergoes no complete winding around the origin along a closed path in k_y-direction.

To get a statement about zig-zag edge states, the respective primitive translation vectors (including the strain factor) can be chosen as $\vec{a}_{1c} = \frac{a}{2}(\sqrt{3}, 3s)$ and $\vec{a}_{2c} = a(\sqrt{3}, 0)$.

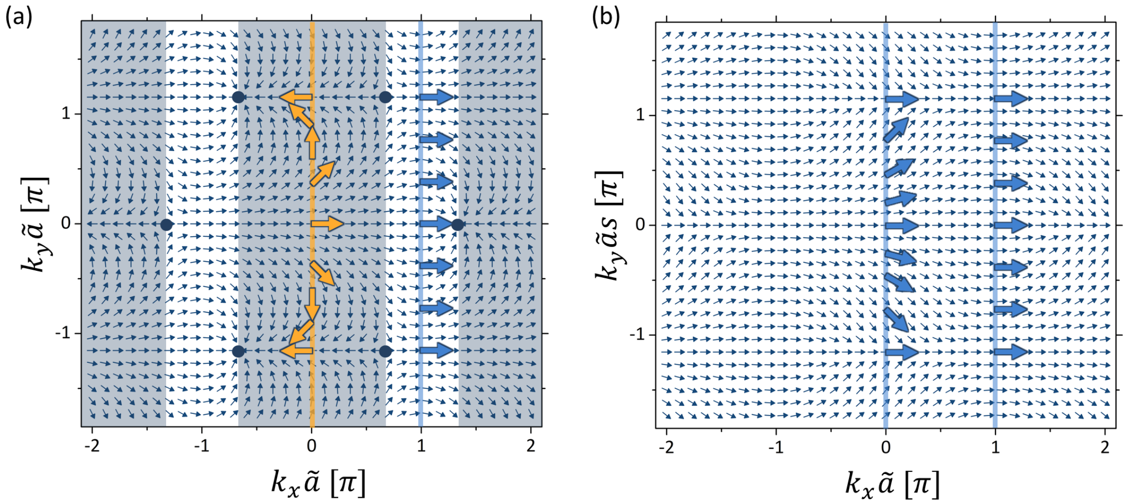

Figure 3.3: Schematic of Berry's phase calculation demonstrating the values of k_x for which a bearded edge state exists. The arrows point in the direction of vector $\vec{h}(\vec{k})$. A complete winding of $\vec{h}(\vec{k})$ along a closed path in k_y-direction is found in the shaded regions, however not in the white regions. Thus, bearded edge states are present in the shaded regions, whereas in the white parts no bearded edge states are present. The plots are shown for (a) the uncompressed ($c_1/c_2 = 1$), and (b) the strongly compressed case ($c_1/c_2 = 2.5$). In (a), the blue dots indicate the Dirac points.

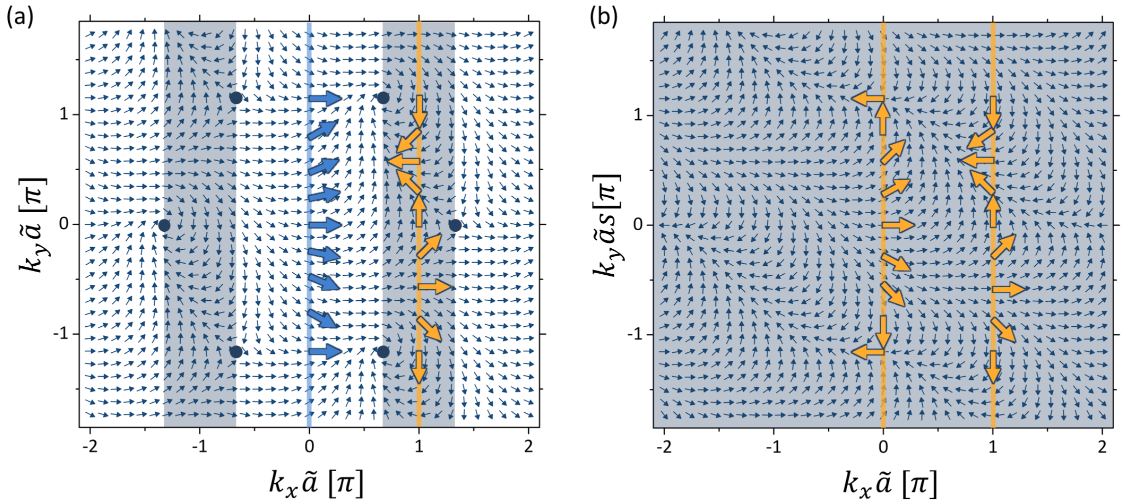

Figure 3.4: Similar to Fig. 3.3, but for the zig-zag termination.

Using these vectors, $\vec{h}(\vec{k})$ is calculated again:

$$\vec{h}(\vec{k}) = \left(c_2 + c_2 \cos\left(\tilde{a}k_x\right) + c_1 \cos\left(\frac{\tilde{a}}{2}k_x + \frac{\sqrt{3}\tilde{a}s}{2}k_y\right),\right. \tag{3.5}$$

$$\left. c_2 \sin\left(\tilde{a}k_x\right) + c_1 \sin\left(\frac{\tilde{a}}{2}k_x + \frac{\sqrt{3}\tilde{a}s}{2}k_y\right)\right). \tag{3.6}$$

An equivalent schematic Berry's phase plot to that one for the bearded edge (Fig. 3.3) can now be depicted for the zig-zag edge. It is shown in Fig. 3.4 for (a) the uncompressed and (b) the strongly compressed case. Here, exactly the inverse picture compared to the bearded termination can be seen: in both cases, the zig-zag edge states exist in the regions of k_x, where no bearded edge states exist. Interestingly, in the strongly compressed case the zig-zag edge states are present for any k_x.

To confirm the results from the schematic Berry phase plots, edge band structures can be computed for different values of the compression and for different edge types. This follows the derivation in Section 2.2.2. The band structure yields the propagation constant k_z, of a given eigenmode of the Hamiltonian. Here, instead of applying the tight-binding model, rather the more accurate continuous paraxial Helmholtz equation (2.23) with laboratory parameters is used. It is an exact description of the spatial photonic band structure and provides a better comparability to the findings of the experiment. In doing so, the two first bands are no longer perfectly symmetric and the propagation constant of the edge state is not completely flat, but slightly curved.

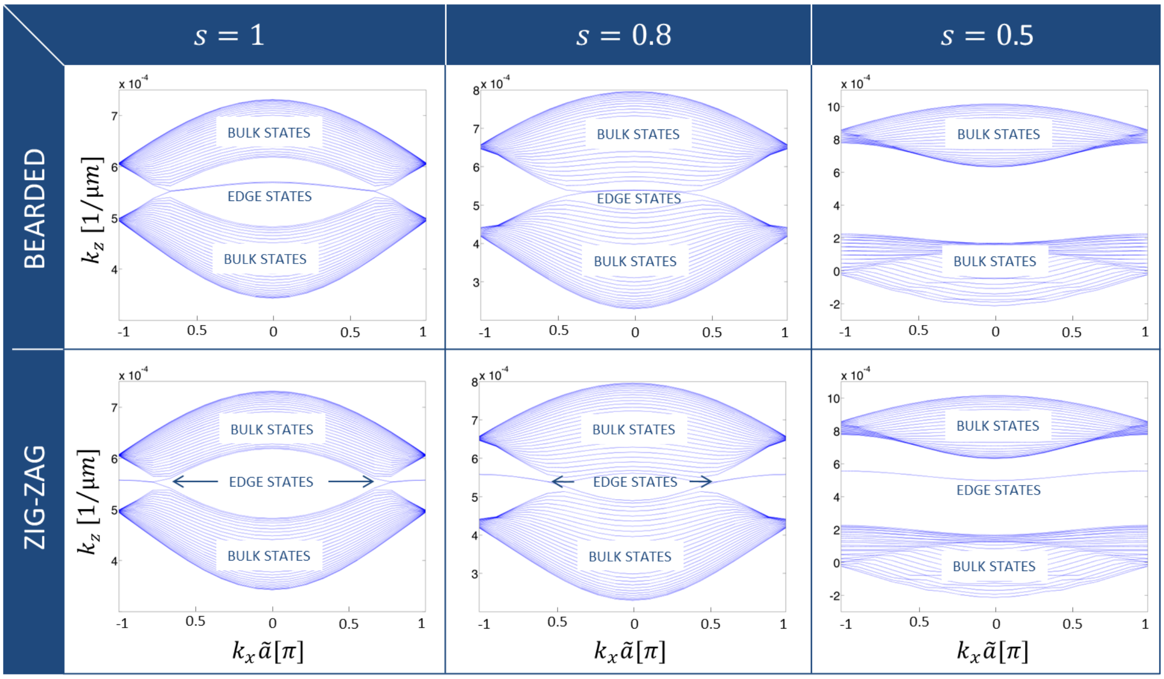

Figure 3.5: Edge band structures, calculated using the full paraxial Helmholtz equation (2.23), with the propagation constant k_z plotted versus k_x for lattices with bearded and zig-zag termination and three different compressions. In the left row, there is no lattice compression ($s = 1$), the second row shows a sub-critical compression ($s = 0.8$), and the right row exhibits a super-critical compression ($s = 0.5$), past the point of the Dirac points merging.

The edge band structures are plotted in Fig. 3.5 for bearded as well as zig-zag edges each for three different values of the compression: $s = 1.0$ (uncompressed), $s = 0.8$ (slightly compressed), and $s = 0.5$ (strongly compressed after the merging of the Dirac points, with a band gap present). It can be seen that with increasing compression the Dirac points get closer. At the same time, the region in which the bearded edge state exists, shrinks. In return, the zig-zag edge state occupies a larger fraction of the edge BZ. While the edge state at the bearded edge vanishes with increasing compression it arises at the zig-zag edge. After the Dirac points have merged at the topological transition, the zig-zag edge state exists in the whole edge BZ, whereas the bearded edge state is eliminated. Consequently, the topological transition goes along with an edge state transition which is not only present in the perfect discrete lattice model, but also in a continuous system. Accordingly, edge state experiments can be utilized to demonstrate the topological transition.

3.2 EDGE STATE OBSERVATION AS FUNCTION OF TRANSVERSAL WAVE NUMBER

For the experiments, lattices with different strain factors were fabricated by femtosecond direct laser writing (Section 2.3.3) in a 10 cm long sample. The nearest neighbor distance between waveguides in the uncompressed case was $a = 22\,\mu\text{m}$ leading to a lattice constant of $\tilde{a} = 22 \times \sqrt{3}\,\mu\text{m}$. Experiments were performed in lattices, where the vertical direction was compressed by a factor of $s = 0.5,\ 0.6,\ 0.7,\ 0.8,\ 0.9$, and 1.0, resulting in coupling constant ratios of $c_1/c_2 = 3.6,\ 2.6,\ 1.9,\ 1.5,\ 1.1$ and 0.9, respectively. Note the coupling ratio in the uncompressed case is $c_1/c_2 \neq 1$ due to the elongation of the waveguides in the y-direction yielding a higher coupling constant in the horizontal direction in comparison to the vertical one for equal distances. This makes the conversion of the strain factor s into the coupling constant ratio c_1/c_2 more complicate than defined in the theoretical part in Eq. (3.1). The here denoted coupling constant ratios were achieved by finding the best fit between the experimentally measured output images and numerical simulations using the beam propagation method. The photonic graphene lattices are fabricated such that each sample contains besides two armchair edges, one bearded and one zig-zag edge. Microscopic images of the front facets of the uncompressed and the most strongly compressed lattices are shown in Fig. 3.6(a) and (b), respectively. Figure 3.6(c) shows the vertical coupling parameter c_1 and the diagonal coupling parameter c_2. The measurement was performed in the following way: at the input facet of the array an elliptically shaped beam was shined into the edge waveguides, once for the bearded and once for the zig-zag edge. The Bloch wave number k_x of the incoming beam was shifted to perform a "spatial spectroscopy"measurement at the edge as described in Section 2.3.4. Afterwards, near field images of the output facet were taken, each for a certain value of k_x. Finally, the ratio of the optical power remaining on the edge (within the first two rows of waveguides) relative to the power diffracted into the bulk was evaluated as a function of k_x. This is done for different lattices, each with a certain strain. The results are plotted within the first edge BZ in Fig. 3.7. While the different strains allow to observe the transition between the edge states, the "spatial spectroscopy"enables a scan in the reciprocal space. Furthermore, numerical continuum simulations were performed employing the beam propagation method (BPM), in which the continuous paraxial Helmholtz equation (2.23) is solved along the propagation direction z in a finite honeycomb lattice (for further details see Appendix).

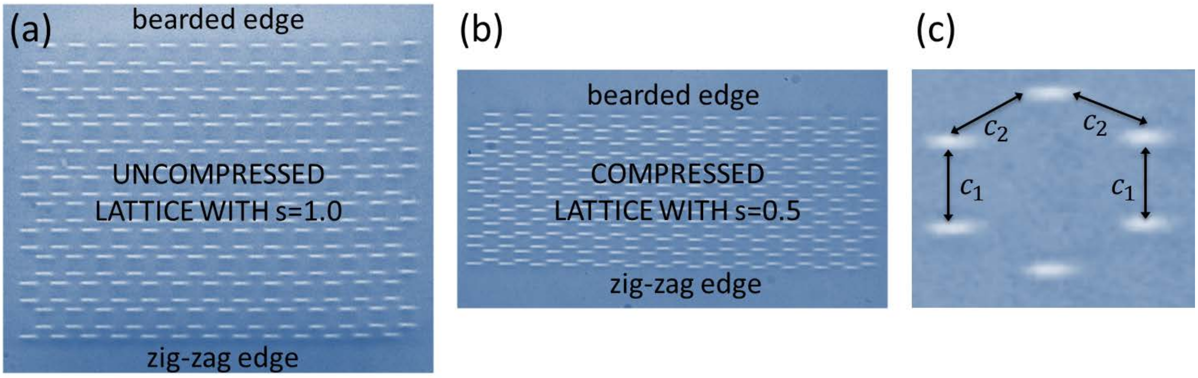

Figure 3.6: Microscopic images of (a) the uncompressed lattice and (b) the most strongly compressed lattice. (c) Section of one hexagon of waveguides with vertical coupling parameter c_1 and diagonal coupling parameter c_2 specified.

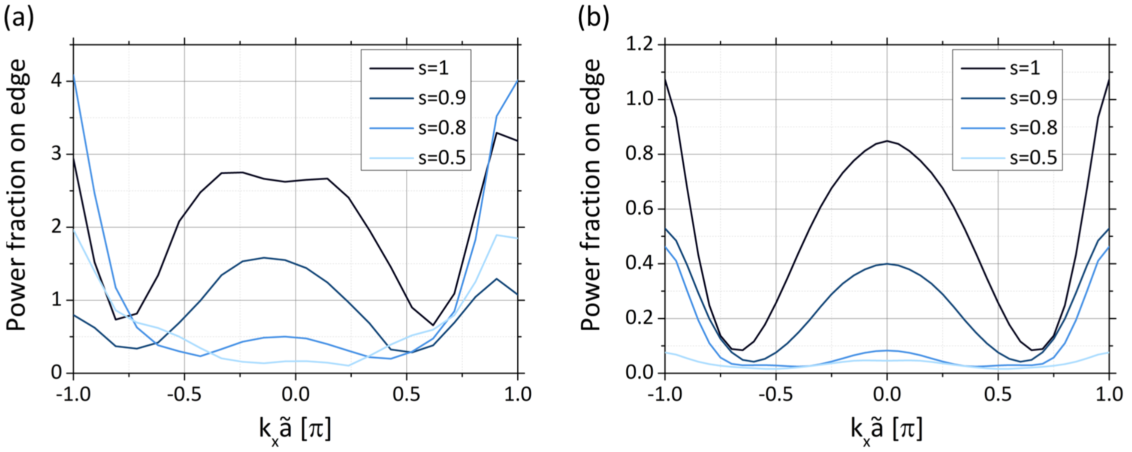

Figure 3.7: Ratio of optical power on the bearded edge to that diffracted into the bulk plotted against k_x from (a) experimental results and (b) from numerical BPM simulations.

The experimental results and the numerical simulations for the bearded edge excitation are plotted in Fig. 3.7(a) and (b), respectively. For the uncompressed lattice with $s = 1.0$, there is strong confinement in the center of the edge BZ, indicating an edge state. The strong edge confinement near $k_x = \pm\pi/\tilde{a}$ is due to the presence of another, non-topological edge state. This edge state cannot be explained using the coupled mode theory as introduced in Section 2.3.1 and is described in detail in [75]. With increasing compression, the region in which the bearded edge state exists gets smaller as a result of the approach of the Dirac points. Additionally, the results depict that the edge state on the bearded edge is less confined for increasing compression. This is due to the stronger vertical coupling, where a higher fraction of light is penetrating the bulk lattice.

Equivalent experiments and numerical simulations were performed for the zig-zag edge, with the results shown in Fig. 3.8(a) and (b), respectively. If there is no compression (s=1.0), the zig-zag edge state exists in the outer thirds of the edge BZ. With increasing strain, as theory predicts, the opposite image as for the bearded edge appears. The region where the zig-zag edge state exists in the edge BZ expands for increasing compression. In case of the most strongly compressed lattice the edge state occupies all values of k_x as it can be seen by the high power fraction residing on the edge. The experimental results at both, the bearded and the zig-zag edge are confirmed by numerical simulations. The slight differences may arise due to some uncertainty of the

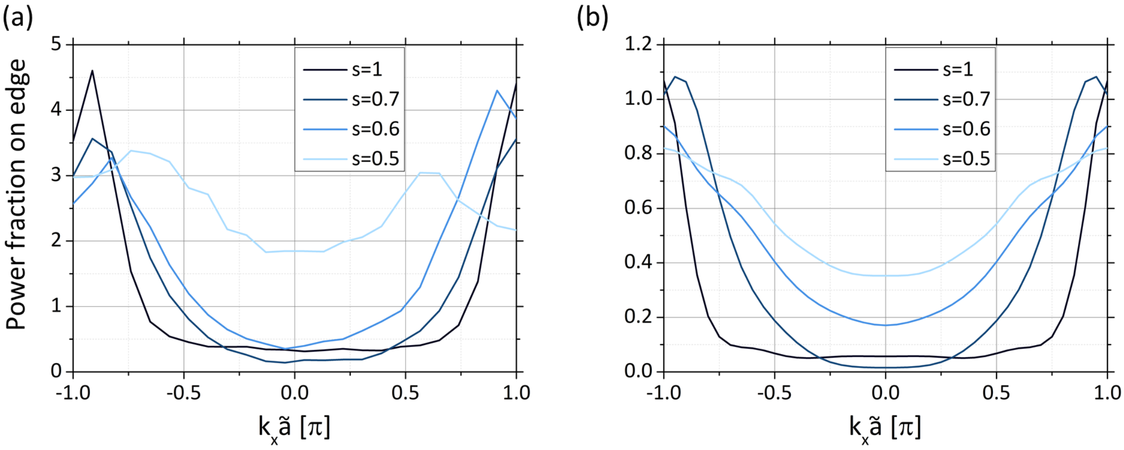

Figure 3.8: Ratio of optical power on the zig-zag edge to that diffracted into the bulk plotted against k_x for (a) experimental results and (b) for numerical simulations using BPM.

exact excitation parameters (center position, width of beam, exact orientation of the ellipse, and k_x) and hence, also differ from the perfect excitation used in the numerical simulations. Furthermore, fabrication effects play a role, as for example the fact, that the refractive index of the waveguides slightly changes with the depth in which they are fabricated. A measurement of this effect shows a change of the refractive index of approximately 0.2 per hundred microns writing depth. For the sake of simplicity, that divergence is not taken into account in the numerical simulations.

Four exemplary near field images of the light distribution at the output facet as evaluated to obtain Figs. 3.7 and 3.8 are depicted in Fig. 3.9, with the excitation region marked by a white ellipse. The left row shows an excitation of the bearded edge, whereas in the right row the zig-zag edge was excited. In all cases the excitation was performed using a reciprocal wave vector of $k_x = 0$, the center of the edge BZ. In the uncompressed case, light is confined to the bearded edge due to the presence of the edge state (Fig. 3.7(a)). If the zig-zag edge is excited, light is diffracted into the bulk of the lattice since in the edge BZ center no zig-zag edge state exists in the regular lattice (Fig. 3.7(c)). This completely changes in the strongly compressed lattice ($s = 0.5$), where now light gets diffracted into the bulk if the bearded edge is excited (Fig. 3.7(b)) but stays confined at the edge for input at the zig-zag edge (Fig. 3.7(d)). Thus, just as the edge state is destroyed on the bearded edge, it arises at the zig-zag edge. We observe

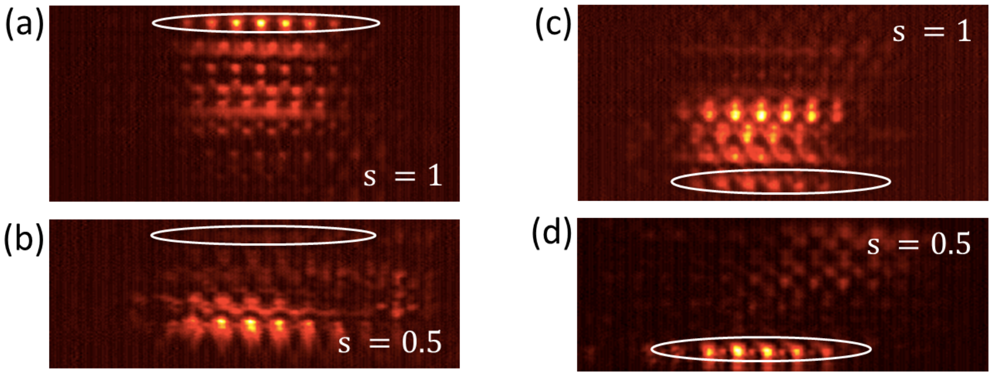

Figure 3.9: Experimental output images during elliptical edge excitation with phase $k_x = 0$ (white ellipse indicates the input region). (a) and (b) Excitation at bearded edge. (a) In the uncompressed lattice a bearded edge state exists at $k_x = 0$ and hence can be excited and (b) in the most strongly compressed lattice no bearded edge state is present such that the light diffracts and is not confined at the edge after 10 cm of propagation. (c) and (d): Excitation at zig-zag edge. (c) In the uncompressed lattice no zig-zag edge state is present at $k_x = 0$ and (d) in the most strongly compressed lattice a zig-zag edge state has arisen.

this edge state behavior as a result of the merging of the Dirac points with its subsequent opening of the bandgap.

In summary, the edge state experiment clearly demonstrates the destruction of edge states on the bearded edge of photonic graphene, while at the same time edge states on the zig-zag edge were created under the application of a one-dimensional strain. It is theoretically shown that this is correlated with a topological transition the system undergoes under strong linear compressions. In general, topological properties are characterized by their insensitivity to small perturbations. The experiments here are a prime example where a strong perturbation is employed to cause a transition between two topologically distinct phases. The strong strain leads to the fusion of the Dirac points that are characterized by the topological property of the Berry phase. As a result, the Berry phases of the Dirac points annihilate tuning the system from one topological phase to another. This result is general and holds not only for graphenelike structures of any kind, but most probably also will occur in other lattices exhibiting singular points in reciprocal space, as e.g. Lieb lattices.

4

PSEUDOMAGNETIC FIELD INDUCED BY INHOMOGENEOUS STRAIN

In general, magnetic effects at optical frequencies are notoriously weak. In consequence, magneto-optical devices must be comparatively large and cannot be applied on-chip. One possibility to induce magnetism at optical frequencies is the use of metamaterials. They work near resonances and contain metallic components with the drawback that they suffer from high losses. None of this is the case in the specially deformed photonic graphene system exhibiting pseudomagnetic effects at optical frequencies shown within this chapter. In contrast to a real magnetic field, a pseudomagnetic field does not break time-reversal symmetry. However, it leads to a splitting of the band structure into highly degenerate Landau levels in reciprocal space – as it is the case under the application of a real magnetic field. This can experimentally be proven by demonstrating a confinement of incident light, which lies in the bandgap between Landau levels.

The idea of inhomogeneous strain causing similar physical effects in a graphene lattice as an external magnetic field was brought up by Kane and Mele in 1997 [89]. Guinea et al. then in 2010 developed a precise theory of engineering a certain inhomogeneous strain in graphene corresponding to a constant magnetic field [90]. Experiments were performed with atomic graphene, which was grown on a particular surface. During the manufacturing process nanobubbles emerge, which exhibit a certain strain of the lattice and the formation of Landau levels was shown [71]. Within this thesis, by making the photonic graphene lattice aperiodic in a certain manner, the first realization of an ultrastrong pseudomagnetic field in optics will be demonstrated [91]. Photonic graphene compared to carbon-based graphene benefits from the ability that arbitrary strain can easily be implemented during fabrication.

4.1 STRAIN AND LANDAU LEVEL FORMATION

For wave packets lying near a Dirac point it has been shown, that straining graphene is mathematically equivalent to introducing magnetic fields [89]. Since this only relies on the lattice geometry, it is of course also valid for photonic graphene. In particular, a given position-dependent two-dimensional strain tensor $U(\vec{r})$ gives rise to a vector potential $\vec{A}(\vec{r}) = \pm \left(u_{xx} - u_{yy}, -2u_{xy}\right)/2l_0$, where u_{xx}, u_{yy}, and u_{xy} are the elements of $U(\vec{r})$, and the sign depends on which Dirac point is in question. From that vector potential a magnetic induction can be calculated via $\vec{B}(\vec{r}) = \nabla \times \vec{A}(\vec{r})$. Based on the theory of Guinea et al. [90], the photonic graphene system is strained using a radial and azimuthal displacement u_r and u_θ of each waveguide from its original position in the regular honeycomb lattice. It is defined by:

$$(u_r, u_\theta) = qr^2(\sin 3\theta, \cos 3\theta), \tag{4.1}$$

where r is the distance from an arbitrary origin (usually the center of the lattice), θ is the azimuthal angle, and q is a parameter determining the strength of the applied strain. Note, this kind of strain is completely different to the one applied in the previous Chapter 3. It is a position-dependent displacement breaking the periodicity of the lattice. Hence, also the coupling between neighboring waveguides is no longer constant, rather than a function of the position. In general, the coupling dependence on the distance d to the adjacent waveguide is given by: $c(d) = c_0 \mathrm{e}^{-(d-a)/l_0}$, where a is the nearest-neighbor spacing of the regular lattice, l_0 is the coupling decay length, and c_0 is the coupling

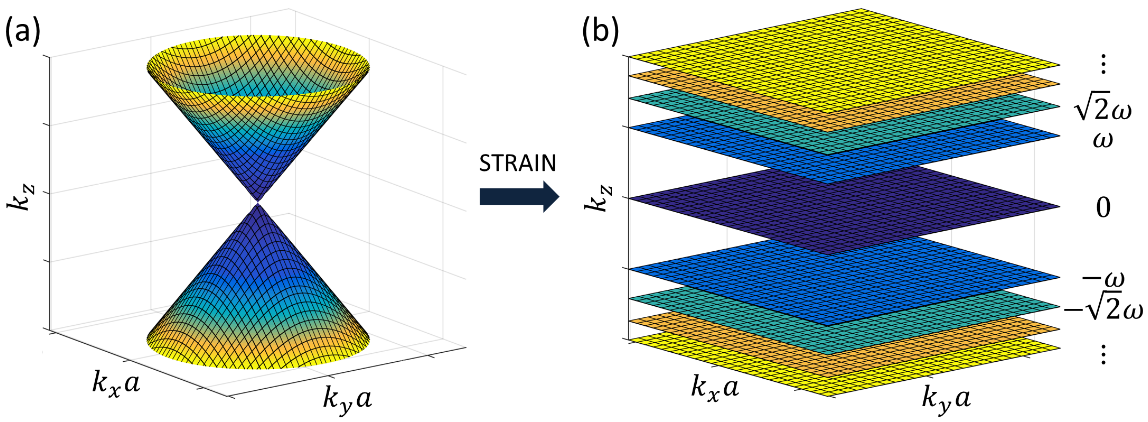

Figure 4.1: Dirac cone region of the spectrum (a) of a regular honeycomb lattice and (b) its splitting into Landau levels with $k_z = \pm\omega\sqrt{N}$ (where $N = 0, 1, 2, ...$), when a certain strain as defined in the text is applied to the lattice.

strength at $d = a$. The above introduced displacement allows to describe the lattice in the Dirac point region using a vector potential $\vec{A}(\vec{r}) = \pm 4q\,(y, -x)\,/l_0$, which is in the symmetric gauge and corresponds to a magnetic field of strength $B = 8q/l_0$. In contrast to a real magnetic field, this pseudomagnetic field does not break time-reversal symmetry in carbon-based graphene. Transferred to photonic graphene, it does not break z-reversal symmetry. The reason is that half of the Dirac cones underlie a field in the $+z$-direction, whereas the other half experiences a field in the $-z$-direction. In fact, breaking z-reversal symmetry in photonic graphene requires temporal or longitudinal modulation of the system as will be demonstrated in Chapter 5.

In reciprocal space, the application of a magnetic field leads to the formation of Landau levels with bandgaps in between. This means that the eigenstates of the system are no longer spread over a wide region of k_z, but congregate at discrete, highly degenerate levels. In photonic graphene, the separation of the spectrum into Landau levels is given by

$$k_z = \pm\omega\sqrt{N}, \text{ with } N = 0, 1, 2, ..., \tag{4.2}$$

where $\omega = 3\sqrt{B}c_0 a/2$. The spacing of the Landau levels is unique to honeycomb structures, and is strongly affected by conical dispersion in the vicinity of the Dirac cones. In two-dimensional electron gases with quadratic dispersion, as usually used to show the quantum Hall effect, the Landau levels are equally spaced and do not include

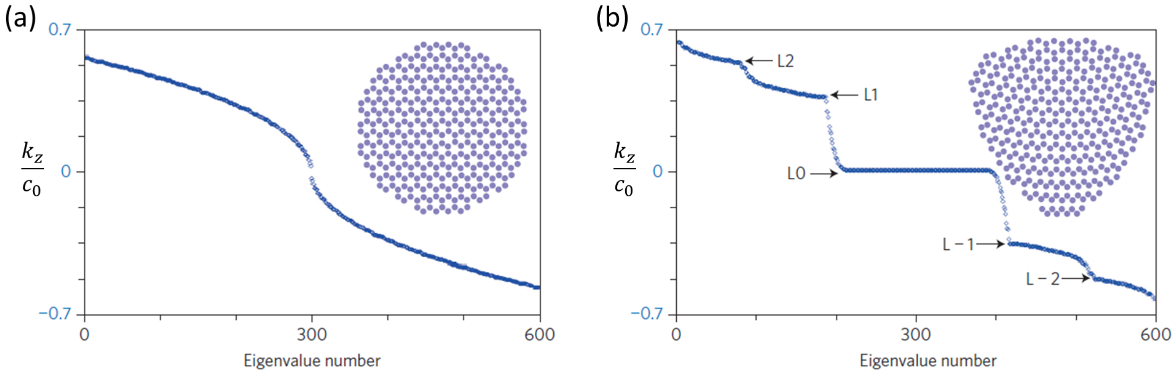

Figure 4.2: (a) Numerically computed eigenvalues of a regular photonic graphene lattice with ≈ 9600 waveguides plotted in the vicinity of the Dirac points. It is chosen such that only armchair edges are present. In the inset a section of the circular lattice is plotted. (b) Numerically computed eigenvalues of the specially strained lattice under the effect of the pseudomagnetic field. Clearly, Landau levels emerge in the eigenvalue spectrum labelled with "LN"and edge states are lying in between them. Inset: effect of the strain on the section of the lattice as shown in (a).

the zeroth Landau level [92]. The change in the spectral region does not only happen under the application of a real magnetic field but also under a pseudomagnetic field. Hence, the above described pseudomagnetic field splits the spectrum of an infinite photonic graphene lattice around the Dirac cone region into highly degenerate Landau levels with bandgaps in between as schematically depictured in Fig. 4.1. Note, this is an accurate description of the band structure in the vicinity of the Dirac point regions only. In the other parts of the reciprocal space, the eigenstates form a continuous band and cannot be described by the pseudomagnetic field. However, in the vicinity of the Dirac points the splitting effect is significant.

The approach above is based on an infinite lattice. Now a finite lattice exhibiting edges will be considered. For that purpose, a numerical tight-binding calculation for a very large photonic graphene system consisting of ≈ 9600 waveguides is performed. The shape is chosen such that all edges are of armchair type and thus support no edge states. A small part of the structure is depicted in the inset of Fig. 4.2(a). In the Figure itself, the eigenvalues of the system are plotted in ascending order (that is, the spatial spectrum) and only a small region around the Dirac point is depicted. The eigenvalues are widely spread over the spectrum. Albeit, in the direct vicinity of the Dirac points they get less densely packed due to the fact that the density of states approaches zero there. Figure 4.2(b) is an equivalent plot, with the lattice strained as defined in Eq. (4.1) (the shape of the lattice is schematically depicted in the inset). The applied strain here is $q = 0.0015a^{-1}$ and the coupling decay length is $l_0 = a/5$. Distinct plateaus in the spectrum arise corresponding to a higher density of states since there exist many eigenstates at the same value of k_z. These plateaus are the Landau levels emerging in the spectrum and according to Eq. (4.2) their propagation constants are calculated to be $k_z = \pm 0.37\sqrt{N}c_0$. These positions perfectly coincide with the numerical results of Fig. 4.2(b). Thus, in the vicinity of the Dirac points, the assumption that the states underlie the Dirac equation is fully justified. Therefore, the finite, just like the infinite, photonic graphene lattice exhibits Landau levels. Nevertheless, differences between the finite and the infinite lattice occur. In contrast to the infinite system, where band gaps are found in between the Landau levels, here states clearly exist in between them. Looking into the nature of these eigenstates offers an interesting detail: they are solely localized at the edge of the system, that is, these are strictly edge states. In the case of, e.g., the quantum Hall effect, it is these edge states that give rise to the quantum Hall conductivity. Additionally, edge states exist at $k_z = 0$, where usually zig-zag and bearded edge states appear in the spectrum. These originate due to deformation effects at the edge. Although the unstrained lattice exhibits only armchair edges not supporting edge states this changes in the strained lattice. Here, the armchair edge gets partly the character of other types of edge termination supporting edge states. Hence, some of the states in the zeroth Landau level have significant power residing on the armchair edge.

4.2 EXPERIMENTAL EVIDENCE OF PSEUDOMAGNETIC FIELD

To demonstrate the pseudomagnetic field in experiments, its effect in splitting the band structure into Landau levels is utilized. First, different photonic graphene lattices with increasing strain from $q = 0$ to $q = 0.021a^{-1}$ (as defined in Eq. (4.1)) were fabricated

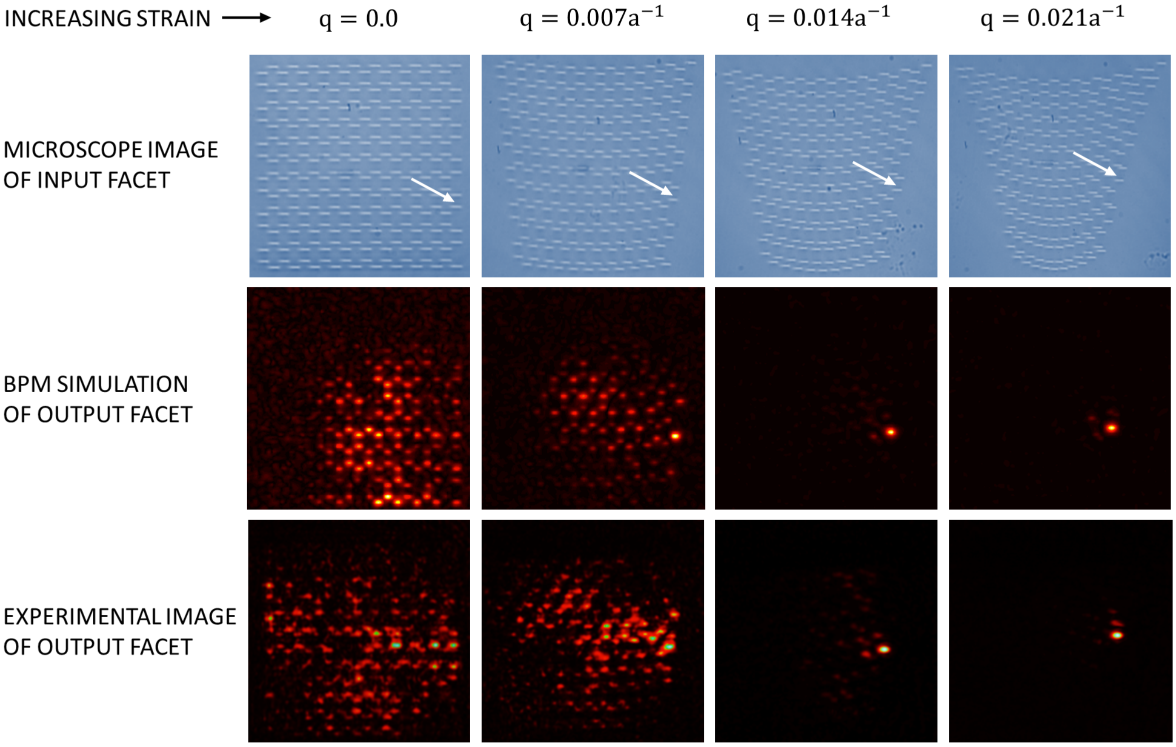

Figure 4.3: Top row: Microscope images of the input facet of the photonic graphene samples. The white arrows mark the waveguide at the armchair edge being excited by the input light. Centre row: Simulations of the light intensity distribution at the output facet using beam propagation method (BPM). Bottom row: Experimental images of the output facets. In the unstrained case with $q = 0$, no confinement is present since no edge state exists at the armchair edge (left column). From second to the fourth column the strain is successively increasing ($q = 0.007a^{-1}$, $q = 0.014a^{-1}$, and $q = 0.021a^{-1}$). With increasing strain the light becomes highly confined at the input waveguide, because more and more (and finally all) of the excited eigenstates are either in a band gap between Landau levels (and therefore cannot penetrate into the bulk) or are degenerate states in the zeroth Landau level.

by femtosecond direct laser writing (Section 2.3.3). A nearest-neighbour distance of the unstrained lattice of $a = 14\,\mu\text{m}$ is chosen. The microscope images of four different lattices are shown in the upper row of Fig. 4.3. Apart from the fact that it would be disrupted, if a piece of carbon-based graphene was strained to the applied extent it would underlie an immense pseudomagnetic field strength of approximately 5500 T.

To find an experimental evidence of the pseudomagnetic field, light of a HeNe-laser at 633 nm was launched into a single waveguide at the armchair edge via a fiber. The excited site is marked by a white arrow in Fig. 4.3. In the regular lattice, no edge state is associated with the armchair edge and hence, the incident light is scattered into the bulk of the waveguide structure. The continuum BPM simulations (see Appendix) of the light distribution at the output facet and the experimentally obtained distributions are shown in the first column of Fig. 4.3. They clearly reveal a spreading of the light during propagation. The minor discrepancies between simulations and experiments can be attributed to the fact that there is an uncertainity about the precise refractive index increase profile of the waveguides (see Chapter 2.3.3).

Investigating the pseudomagnetic field in strained photonic graphene, the same waveguide as before (at the armchair edge) was excited. For two reasons, this waveguide is excited to obtain information about the effect that strain has on the band structure as will be explained in further detail in the following section: (i) it provides a straightforward way of accessing the Dirac region of the spectrum and (ii) the degree of localization on the edge is a clear indicator whether (or not) the propagation constant of the excited spatial eigenmodes lies in a bulk bandgap between Landau levels.

To get an idea about which part of the band structure is addressed when exciting the l-th waveguide, the projection of the wave function Ψ_l onto each eigenstate Φ_n of the system is calculated as $|\langle\Psi_l|\Phi_n\rangle|$. If the l-th waveguide is equal to the experimentally excited one, this reveals mainly an overlap in the Dirac cone region for large strain values. To verify this, a tight-binding calculation of the eigenstate and eigenvalue spectrum in the Dirac cone region for $-0.6 \leq k_z/c_0 \leq 0.6$ was performed. The overlap $|\langle\Psi_l|\Phi_n\rangle|$ is plotted in Fig. 4.4 for both the unstrained and strained system. Additionally, the eigenvalue spectrum is plotted in blue as a guide to the eye where the Landau levels reside. The strain considered in Fig. 4.4(b) is $q = 0.015a^{-1}$ in accordance with Fig. 4.2(b).

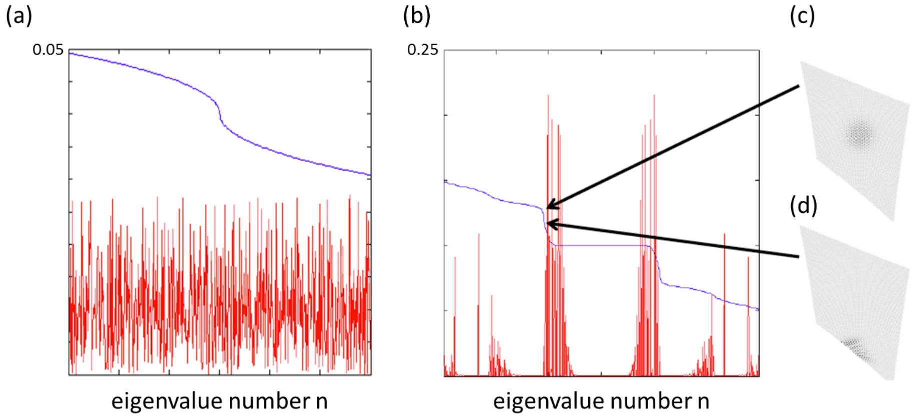

Figure 4.4: Projection of the single waveguide input function (exciting the lth waveguide (Ψ_l)) onto each eigenstate Φ_n of the system (a) for the unstrained case and (b) for a strain of $q = 0.015a^{-1}$. The spatial eigenvalue spectrum is shown in blue as a guide to the eye where the Landau levels reside. (c) and (d) show two exemplary eigenstates spectrally located at the first Landau level (c) and in the bandgap between zeroth and first Landau level (d).

In the unstrained case (Fig. 4.4(a)), the overlap of the initial state with the different eigenstates of the system is distributed quite evenly over the whole spectrum. The fraction of power that resides in eigenstates in the Dirac region is 9%. This low value is caused by the fairly low density of states in that region. This changes in the strained case plotted in Fig. 4.4(b). There, 55% of the projected power resides in the Dirac region and calculations with increasing strain resulted in a monotonically increasing fraction of power residing in the Dirac region. Hence, if in the performed experiments, a waveguide at the armchair edge in the most strongly strained lattice is excited, the input state lies entirely in the Dirac cone region in reciprocal space. Accordingly, the excited states lie either in the bandgap between Landau levels or they are degenerate eigenstates lying in the zeroth Landau level as usually associated with zig-zag and bearded edges of the honeycomb lattice. As explained above, the distortion of the lattice yields edge states at $k_z = 0$ on the armchair edge, too. However, in both cases the input light will stay confined. Exciting a state in the band gap leads to confinement to the edge since it cannot couple into the bulk states lying in the different Landau levels. If edge states in the zeroth Landau level are excited they are necessarily degenerate as all zero-energy (here corresponding to $k_z = 0$) edge states in graphene [93]. Thus, here they all have the same propagation constant and all acquire phase at the same rate during propagation. Consequently, such states will not spread. An example of a typical first Landau level eigenstate in real space is plotted in Fig. 4.4(c). Additionally, a tpyical eigenstate lying in the band gap is shown in Fig. 4.4(d).

In the simulations and experiments, shown in Fig. 4.3 (panels of the second and third row), the above described behaviour is confirmed. With increasing strain of the photonic graphene lattice, the light gets more and more confined at the input waveguide at the armchair edge and does not spread during its propagation along the 10 cm long sample. For sufficiently large strain, the light stays completely confined to the edge and does not at all couple to bulk modes since the states, which are excited, are either in a gap between Landau levels or are degenerate edge states at $k_z = 0$.

4.3 BAND STRUCTURE SCAN BY PROPAGATION CONSTANT CHANGE

The experiments shown so far strongly indicate a splitting of the band structure due to the pseudomagnetic field. However, it is important to ensure that the experimentally shown confinement behavior is not caused by a coincidental perturbation near the edge, which would constitute a simple 'defect mode'. For that reason another experiment is performed, where the excited waveguide at the armchair edge is replaced by a 'defect waveguide'. Five additional samples of the most strongly strained lattice type with $q = 0.021a^{-1}$ were fabricated with one site being modified. The refractive index of the excited waveguide was changed (leaving all others fixed) such that it was above or below the others. Hence, the coupled mode equations as defined in Eq. (2.24) can here be rewritten as:

$$i\partial_z \phi_n = -\sum_{\langle m \rangle} c_{n,m}\phi_m(z) - k_z^l \delta_{nl}\phi_n, \tag{4.3}$$

where the summation is only taken over nearest neighbour waveguides with a coupling constant of $c_{n,m}$, and k_z^l is the intrinsic propagation constant of the defect waveguide mode. The dimensionless parameter k_z^l/c_0 can be changed during the fabrication process (as described in Section 2.3.3) to be either positive if the change in the refractive index is positive and negative if the change in refractive index is negative. In the potential well picture this corresponds to changing the depth of the potential well of the input waveguide at the armchair edge with respect to all other potential wells to be either higher or deeper. Consequently, the propagation constant of the input waveguide mode can be tuned with respect to the band structure opening up the possibility of a band structure scan.

In Fig. 4.5(a), the nature of the band structure of the strained configuration is schematically depicted. In the center, the pseudomagnetic effect splits up the band into Landau levels with gaps in between them. Since the pseudomagnetic field effect occurs in the Dirac cone region only, the states in the remaining parts of the spectrum do not assemble in Landau levels. Hence, above and below the regions split into Landau levels, largely bulk eigenstates that spread throughout the lattice are found. Going further to even higher and even lower values of k_z/c_0, the edges of the first bands are reached and a band gap is present (although not one induced by the strain). For different refractive index values of the excited waveguide, this manifests in either confinement (if k_z^l lies in a band gap), or spreading (if k_z^l lies in a region composed of bulk states). The resulting light distributions of the experiments performed in the different lattices are shown in Figs. 4.5(b)-(g). If $k_z^l/c_0 = 0$ no defect mode is present and the result from the above experiment holds. As shown in Fig. 4.5(b) strong confinement is found since the excited states lie in the gap between Landau levels or are degenerate eigenstates at $k_z = 0$. Slightly decreasing the refractive index of the defect waveguide ($k_z^l/c_0 \approx -0.5$) a very slight expansion of the light beam at the output facet can be detected (Fig. 4.5(c)), since the overlap with bulk states has marginally increased. Further decreasing the refractive index of the input waveguide ($k_z^l/c_0 \approx -2$) leads to a significant spreading of the light during propagation (Fig. 4.5(d)). This is caused by the strong overlap between the exciting mode and the continuum eigenstates, far away from the Landau level region. Similar behaviour can be found, when changing the defect waveguide such that it has a higher refractive index than the remaining waveguides. When slightly increasing the refractive index ($k_z^l/c_0 \approx 0.5$) a very slight increase in the expansion of the beam is found (Fig. 4.5(e)); whereas strong increase ($k_z^l/c_0 \approx 2$) leads to strong expansion

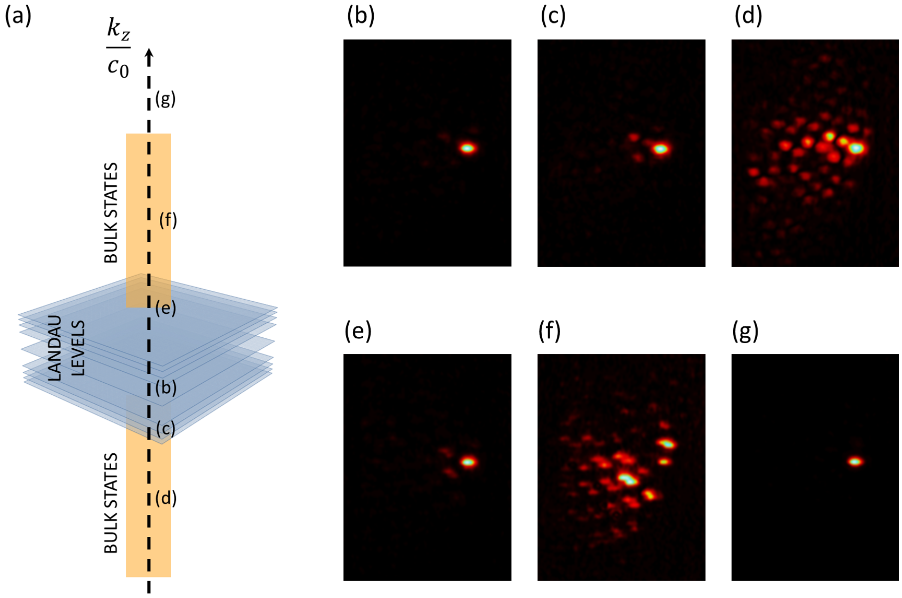

Figure 4.5: (a) Schematic of the eigenvalue spectrum of the strained lattice with Landau levels in the Dirac cone region. (b)-(d) Experimental light distribution at the output facet of lattices with strain $q = 0.021a^{-1}$ and different refractive index values of the input waveguide (lth waveguide) at the armchair edge. Thus, if the refractive index of the excited waveguide is shifted, a defect mode is excited with a different propagation constant. (b) Completely uniform lattice as shown in Fig. 4.3. (c) Defect guide with $k_z^l/c_0 \approx -0.5$ causing some spreading due to slight coupling with bulk states. (d) Larger defect strength ($k_z^l/c_0 \approx -2$) leading to stronger spreading. (e) Mildly positive defect with $k_z^l/c_0 \approx 0.5$ causing slight spreading. (f) Stronger positive defect with $k_z^l/c_0 \approx 2$ leading to coupling into the bulk. (f) Strong positive defect ($k_z^l/c_0 \approx 4$) with its defect mode residing above the first band in the overall band gap leading to localization. The approximate positions of each k_z^l/c_0 in the schematic eigenvalue spectrum is indicated in (a).

because the excited eigenstates are mainly bulk states (Fig. 4.5(f)). Increasing the refractive index of the input waveguide even further ($k_z^l/c_0 \approx 4$), again localization takes place since the defect eigenstate has passed through the entire band and now lies above it (Fig. 4.5(g)). Thus, it cannot overlap with any modes that spread throughout the bulk of the photonic lattice. This band structure scanning experiment demonstrates that both the negative and positive defects lead to spreading. It allows the conclusion that the gaps between the Landau levels, induced by strain, lie at the center of the band in the Dirac region and that exciting the l-th waveguide does not show a simple defect mode in the experiments of the above section 4.2.

In conclusion, theoretically and experimentally an ultrastrong pseudomagnetic field was induced at optical frequencies constituting the first realization of such fields in photonics. The localization of light at the edge of the sample was used to prove the formation of Landau levels with band gaps in between them. This was realized by applying a certain strain to the photonic graphene lattice leading to an aperiodicity of the structure. It was demonstrated, that going from strictly periodic lattices to aperiodic structures can yield very high degeneracies by the formation of Landau levels. Hence, such levels with high density of states might be realizable in a photonic crystal setting (e.g. a photonic-crystal slab on a silicon chip [94] or a three-dimensional photonic crystal [95]). In that regard, they can be used for the enhancement of spontaneous emission and nonlinear wave-mixing processes via the Purcell effect [96]. Thus, the formation of highly degenerate Landau levels suggests the possibility of extreme efficiency enhancement in nonlinear devices in photonic crystals. Generalizing these concepts to lattice systems beyond optics, such as matter waves in optical potentials, offers new intriguing physics that is fundamentally different from that in purely periodic structures.

5

PHOTONIC FLOQUET TOPOLOGICAL INSULATORS

Recently, considerable theoretical effort has been spent to achieve topological protection for electro-magnetic waves at optical frequencies in order to realize optical isolation. Though, making use of an analogue of the quantum Hall effect is inappropriate since magnetic fields are comparably weak in this frequency spectrum. Interestingly, the first proposal of how to achieve a topological non-trivial phase without the need of an external magnetic field in condensed matter physics [46] dates back to 1988 and was discovered by F. D. M. Haldane being honored with the 2016 Nobel Prize in Physics. Yet, while this idea is based on a graphene lattice geometry, it is not transferable to photonic graphene since magnetic fluxes with local lattice-periodicity and the manipulation of next-nearest neighbour coupling are employed. However, another concept from solid state physics can support inspiration: topological insulators [47–49]. They are a fundamentally new phase of matter, supporting extremely robust edge transport otherwise known only for superconductors. In contrast to the quantum Hall effect, in these structures topologically protected edge transport is achieved without the need of an external magnetic field and at room temperature.

In this chapter, an entirely new approach for topological protection of light without the need of external fields will be introduced and experimentally demonstrated. To this end, the trajectories of the individual waveguides comprising the photonic graphene lattice are modified such that z-reversal symmetry is broken. In this structure, one-way edge states that are topologically protected from scattering are observed [97].

5.1 TOPOLOGICAL PROTECTION OF ELECTROMAGNETIC WAVES

Following the seminal work of Raghu and Haldane in 2008 [98], there has been an ongoing effort to realize topological protection in photonic systems. Possible applications of photonic topological insulators in various systems include highly robust delay lines as well as efficient micron-scale on-chip optical isolators [99,100]. The first observation of topological protection of electro-magnetic waves demonstrated the characteristic absence of scattering in a microwave, magneto-optic photonic crystal with a strong, external, static magnetic field [101]. This system can be seen as the photonic analogue of the quantum Hall effect. However, this method of achieving topological protection is limited by the vanishing impact of magneto-optic effects at optical frequencies. Clearly, it is of great interest to realize the photonic equivalent of a topological insulator, which should require no external field, be realizable at optical frequencies, and exhibit scatter-free behavior. Various theoretical proposals have been directed to achieve topological protection of light: (i) by employing bi-anisotropic metamaterials with strong magnetic response [102]; (ii) by using an aperiodic coupled-resonator system with two uncoupled photonic modes [99]; and (iii) by temporal modulation of a two-dimensional photonic crystal structure [103] to explicitly break time-reversal symmetry. However, before the experiments shown within this work were performed [97], no such non-magnetic topological protection was experimentally realized. The work presented here was followed up short afterwards by another experimental realization of topological protection at optical frequencies using a system of coupled ring resonators [104].

The principle, applied here, is in the spirit of so-called Floquet topological insulators.

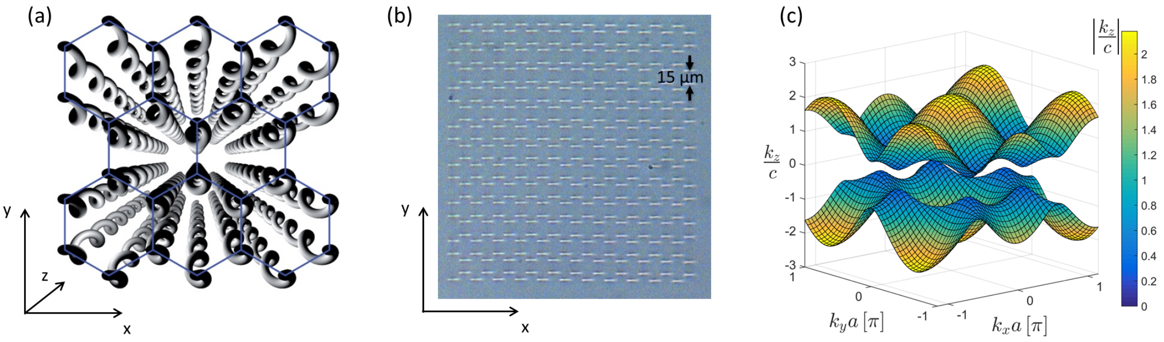

Figure 5.1: (a) Sketch of the photonic graphene lattice with helical waveguides. (b) Microscopic image of the input facet of the honeycomb array with two zig-zag (top and bottom) and two armchair edges (left and right). The nearest neighbour distance of the waveguides is $a = 15\,\mu\text{m}$. (c) Floquet bulk band structure of the helical waveguide honeycomb lattice where a band gap is opened up around $k_z/c = 0$.

This concept was brought up for a solid-state system underlying a time-periodic oscillation in the electron potential, by virtue of an electromagnetic wave passing through the material [105]. It has been proposed that in such materials spin-orbit coupling is not necessary for achieving topological protection [105, 106]. In recent years, graphene too, has been theorized to exhibit topologically protected edge states under the influence of a circularly polarized electric field [106], but this has never been shown experimentally.

5.2 HELICAL HONEYCOMB LATTICE

In order to generate a non-trivial topological phase, a helical trajectory is imposed on the individual waveguides, resulting in a chiral modulation of the lattice. Consequently, the diffraction of light through the honeycomb array of helical waveguides is equivalent to the temporal propagation of electrons as they move through graphene with the carbon atoms rotating around their original position in time. A scheme of the helical photonic graphene lattice and a microscopic image of the front facet of one of the samples is shown in Figs. 5.1(a) and (b), respectively.

The propagation of light in such an array can be described by the paraxial Helmholtz equation as defined in Eq. (2.23). The helix period Z is chosen so as to allow the guided mode to adiabatically follow the waveguide trajectory. Therefore, the coordinates can be transformed into a reference frame where the waveguides are straight in the z-direction:

$$\begin{aligned} x' &= x + R \cdot \cos\left(\Omega z\right) \\ y' &= y + R \cdot \sin\left(\Omega z\right) \\ z' &= z, \end{aligned} \tag{5.1}$$

where $\Omega = 2\pi/Z$ is the frequency of rotation. Now, the Helmholtz equation

$$i\partial_z \psi(\vec{r}, z) = -\frac{1}{2k_0} {\nabla_T}^2 \psi(\vec{r}, z) - \frac{k_0 \Delta n(\vec{r}, z)}{n_0} \psi(\vec{r}, z). \tag{5.2}$$

can be transformed to the new coordinate system. The partial derivative in z and the second partial derivatives in x and y take the form of:

$$\begin{aligned} \partial_x &= \partial_{x'} \tfrac{\partial x'}{\partial x} + \partial_{y'} \tfrac{\partial y'}{\partial x} + \partial_{z'} \tfrac{\partial z'}{\partial x} &&= \partial_{x'} \Rightarrow \partial_x^2 = \partial_{x'}^2, \\ \partial_y &= \partial_{x'} \tfrac{\partial x'}{\partial y} + \partial_{y'} \tfrac{\partial y'}{\partial y} + \partial_{z'} \tfrac{\partial z'}{\partial y} &&= \partial_{y'} \Rightarrow \partial_y^2 = \partial_{y'}^2, \\ \partial_z &= \partial_{x'} \tfrac{\partial x'}{\partial z} + \partial_{y'} \tfrac{\partial y'}{\partial z} + \partial_{z'} \tfrac{\partial z'}{\partial z} &&= -R\Omega \sin\left(\Omega z'\right) \partial_{x'} + R\Omega \cos\left(\Omega z'\right) \partial_{y'} + \partial_{z'}. \end{aligned} \tag{5.3}$$

Substituting these results in Eq. 5.2, and using the abbreviation $\psi' = \psi(x', y', z')$ yields:

$$i\left[-R\Omega \sin\left(\Omega z'\right) \partial_{x'} + R\Omega \cos\left(\Omega z'\right) \partial_{y'} + \partial_{z'}\right] \psi' = -\frac{1}{2k_0} {\nabla_T'}^2 \psi' - \frac{k_0 \Delta n(x', y')}{n_0} \psi', \tag{5.4}$$

and rearranging the above equation, one obtains:

$$i\partial_{z'} \psi' = -\frac{1}{2k_0} {\nabla_T'}^2 \psi' + i \begin{pmatrix} \partial_{x'} \\ \partial_{y'} \\ \partial_{z'} \end{pmatrix} \begin{pmatrix} R\Omega \sin\left(\Omega z'\right) \\ -R\Omega \cos\left(\Omega z'\right)' \\ 0 \end{pmatrix} \psi' - \frac{k_0 \Delta n(x', y')}{n_0} \psi'. \tag{5.5}$$

In the next step, a vector potential $\vec{A}(z') = k_0 R\Omega \left[\sin(\Omega z'), -\cos(\Omega z'), 0\right]$ is introduced, the here valid commutation $\nabla \vec{A} = \vec{A} \nabla$ is applied, and quadratic completement is utilized by introducing the term $-\frac{k_0 R^2 \Omega^2}{2} \psi'$. This finally produces the modified paraxial Helmholtz equation describing the diffraction of light in the helical array in the transformed coordinate system:

$$i\partial_{z'} \psi' = -\frac{1}{2k_0} \left(\nabla_T' + i\vec{A}(z')\right)^2 \psi' - \frac{k_0 R^2 \Omega^2}{2} \psi' - \frac{k_0 \Delta n(x', y')}{n_0} \psi'. \tag{5.6}$$

Interestingly, $\vec{A}$ is fully equivalent to the vector potential associated with a spatially homogeneous electric field of circular polarization. Altogether, it is now possible to simplify the description of the propagation of light in terms of coupled mode equations:

$$i\partial_{z'}\phi_n(z') = -\sum_{\langle m\rangle} c\mathrm{e}^{i\vec{A}(z')\cdot\vec{r}_{mn}}\phi_m(z'), \tag{5.7}$$

where the summation is only taken over nearest neighbour waveguides, c is the coupling constant, and $\vec{r}_{mn}$ is the displacement between waveguides m and n. Here, the Peierls substitution [107] is used, which yields the phase of the coupling constants between waveguides in the presence of a vector potential. In contrast to the previous Chapter 3 and 4, where the waveguides are z-independent, here no static eigenmodes exist since the right-hand side of Eq. (5.7) is z-dependent. However, since the changes along z are periodic, Floquet theory can be applied, which yields Floquet eigenmodes along z-direction being the equivalent to Bloch modes in the x-y plane. Consequently, it allows for describing the solutions of Eq. (5.7) as Floquet modes: $\phi_n(z') = exp(ik_z z')\varphi_n(z')$, where the function $\varphi_n(z')$ is periodic in z [105]. This enables the calculation of the spectrum k_z, called the Floquet eigenvalues (also known as the 'quasi-energies'or 'quasi-propagation constants'), as well as their associated Floquet eigenmodes. The Floquet band structure for the case of helical waveguides with above described parameters is plotted as a function of the transverse Bloch wave vectors k_x and k_y in Fig. 5.1(c). In contrast to the regular tight-binding graphene band structure (2.3), in case of the helical array a band gap emerges.

However, despite the similarity to a conventional insulator, this structure is a Floquet-topological insulator supporting topologically protected edge states. To verify their existence, it is helpful to calculate the edge band structure as described in Section 2.2.2. For that purpose, three different semi-infinite arrays were modeled as shown in Fig. 2.6(a) with two armchair, Fig. 2.6(b) two zig-zag, and Fig. 2.6(c) two bearded edges. Based on that, the respective dispersion curves were calculated. In regular photonic graphene, no edge states exist at the armchair termination. However, at the zig-zag and bearded terminations two degenerate edge states at $k_z = 0$ can be found, one residing at each edge of the array (see Fig. 2.6(e) and 2.6(f)). These are the topologically trivial edge states that exhibit no transverse (x-y-plane) group velocity and therefore do not allow

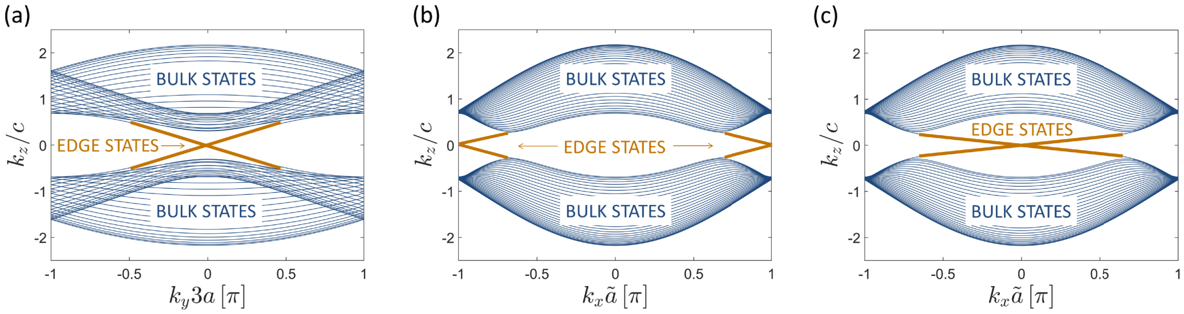

Figure 5.2: Floquet edge band structures of semi-infinite photonic graphene lattices consisting of helical waveguides with a radius of 8 µm shown for the different edge types: (a) armchair edges, (b) zig-zag edges, and (c) bearded edges. In all three cases, a band gap in the bulk is opened in which the edge states (marked in orange) reside. They acquire a non-zero group velocity since they exhibit a slope in their dispersion curves. For each termination, two edge state curves with opposite slopes exist in reciprocal space. However, they are not counterpropagating at one edge, but each of them resides at one of the opposite edges of the sample. Especially, although at the armchair edge (plotted in (a)) in case of helical waveguides, edge states in the band gap arise. Consequently, in a finite lattice this constitutes one edge state circulating around the sample.

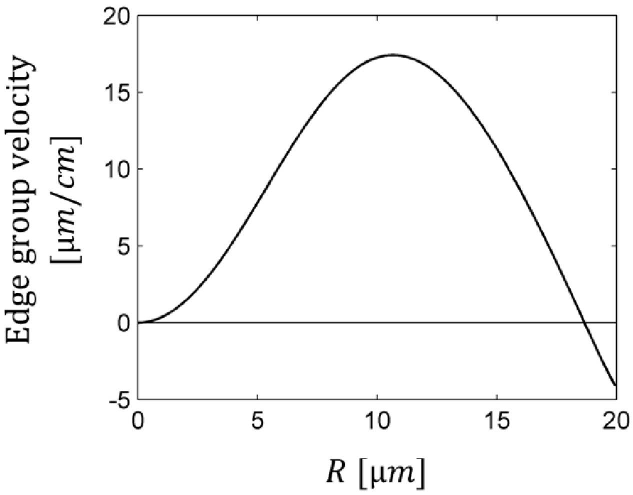

Figure 5.3: Edge group velocity of the zig-zag edge state plotted versus helix radius R of the waveguides. It equals the slope of one of the zig-zag edge state dispersion curves as shown in Fig. 2.6(b) for a certain radius.

for any transport along the edge. However, this changes as soon as the topological band gap is opened by choosing a non-zero radius of the helix. As a result, edge states appear even at the armchair termination. For all three different types of lattice terminations, in the Floquet edge band structure the edge states are no longer degenerate, but clearly acquire a slope as depicted in Fig. 5.2(a-c). They exhibit a transverse group velocity proportional to the first derivative of $k_z(k_y)$ (for armchair termination) or $k_z(k_x)$ (for zig-zag and bearded terminations) and move along the edge.

In each of the three cases in Fig. 5.2, two edge dispersion curves with opposite slopes exist. Thus, the associated edge states move in opposite direction. Importantly, they are not counterpropagating at the same edge as one might expect, but each of them is confined to one of the two existing edges in the semi-infinite lattice. Hence, for example in the case of two zig-zag edges, the edge state at the top is directed to the right, whereas the one at the bottom edge is directed to the left. In a finite array, they consequently merge to a single edge state that propagates clockwise around the sample's edge and is impervious to any backscattering at lattice defects or corners. Since the edge state exists exclusively in the band gap, scattering into bulk states is prevented as well. The existence of the topologically protected edge state can be independently confirmed by calculating the related topological number of the structure, the Chern number as defined in Eq. (2.20). In the here described case, $\mathcal{C} = -1$, meaning that there exists one clockwise propagating edge state at the interface between the helical photonic graphene structure and its environment with a Chern of zero.

The dependence of the transverse group velocity of the chiral edge state at the zig-zag edge (at $k_x = \pi/\tilde{a}$) on the helix radius R is plotted in Fig. 5.3. Interestingly, it is not a monotonic function. First, in the region of small R, the group velocity increases, then at $R = 10.3\,\mu\text{m}$ it reaches a maximum, and up to a radius of $R = 20\,\mu\text{m}$ it decreases. The group velocity even crosses zero which means that the band gap is closed at this special point. Here, another topological transition takes place which corresponds to a change of the Chern number from $\mathcal{C} = -1$ to $\mathcal{C} = 2$ (indicating the presence of two anti-clockwise rotating edge states).

5.3 EXPERIMENTAL OBSERVATION

A lattice of helical waveguides arranged in the photonic graphene structure was fabricated using femtosecond direct laser writing (Section 2.3.3) in a 10 cm long fused silica sample. It exhibits a nearest neighbour distance of the waveguides of $a = 15\,\mu\mathrm{m}$, the period of the helix is $Z = 1\,\mathrm{cm}$, and unless otherwise stated the helix radius is $R = 8\,\mu\mathrm{m}$. To experimentally demonstrate the existence of the topologically protected edge states, except otherwise noted, light at 633 nm is launched into the lattices.

A microscopic image of the front facet of the array in which the first experiment is performed is depicted in Fig. 5.1(b). A broad elliptical beam with a phase of $k_x = \pi/\tilde{a}$ is used to excite the topological edge state at the zig-zag edge (this technique is described in further detail in Section 2.3.4). The light distribution at the output facet is shown in Fig. 5.4 while light was injected into the input facet in the region marked by the white ellipse. The edge state moves during propagation clockwise along the edge of the sample and in Fig. 5.4(a) it can be seen, that at the output facet, it is located in the corner region of the array. In Figs. 5.4(b)-(d) the input position at the zig-zag edge is moved further to the right resulting in a movement of the edge state around the corner and slightly down the perpendicular armchair edge. The light stays confined even when it encounters strong defects such as the lattice corner. Clearly, neither backscattering nor coupling to bulk states takes place. Even at the armchair edge, where in the regular (non-helical) photonic graphene lattice no edge state exists, here the edge state stays confined. Thus, the light propagation behavior observed in this experiment provides very strong evidence of topological protection of the edge state.

The second experiment is performed in a triangular patch of photonic graphene that is exclusively bounded by edges of the zig-zag type; a microscopic image of the front facet of the sample is depicted in Fig. 5.5(a). The lattice parameters are identical to the above mentioned ones. The lattice was fabricated such that a strong defect in its geometry is included by omitting one of the edge sites during the waveguide writing process. For the experiment, light was injected into the upper right corner waveguide (marked by the white ellipse in Fig. 5.5(a)) which leads to the excitation of two different types

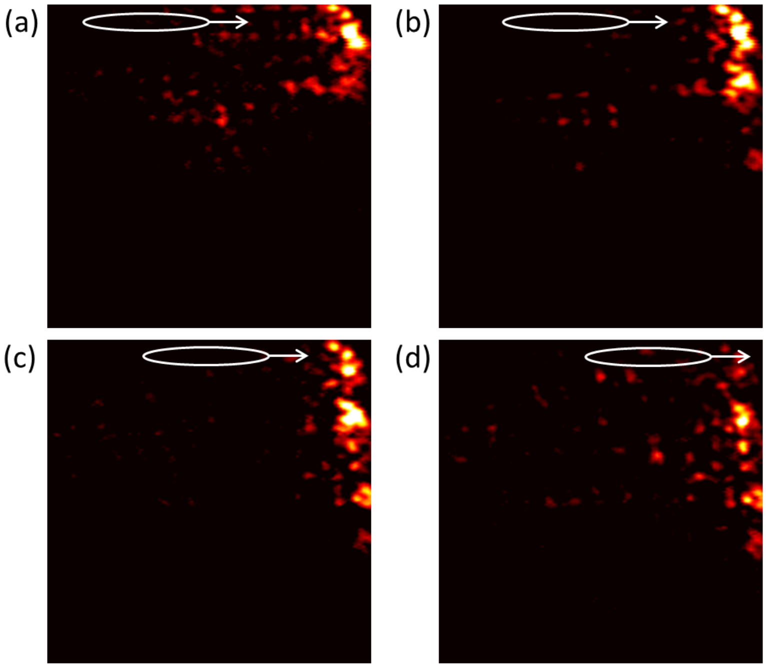

Figure 5.4: Light distribution at the output facet of the helical honeycomb sample ($R = 8\,\mu\text{m}$) when light is shined in at different positions at the zig-zag edge marked by the white ellipse. The microscopic image of the corresponding input facet is shown in Fig. 5.1(b). (a)-(d) During the propagation of the light through the sample along the z-direction, the excited edge state moves to the right, hits the corner, and clearly moves down the vertical armchair edge. When moving the input position rightwards, the output position of the light moves further clockwise along the edge of the sample. Due to the topological protection of the edge state, it is not backscattered or scattered into the bulk during its impact with the corner of the lattice.

of eigenstates: (i) bulk modes extending to the corner and (ii) edge states that meet at the corner. During propagation, the light in the bulk modes spreads over the entire lattice leading to a certain amount of optical power residing in the bulk. If desirable for a given application, this could be readily avoided by matching the excitation beam to the edge eigenstates. The light distribution observed at the output facet of the sample is shown in Fig. 5.5(b). It can clearly be seen that the excited edge state has passed the defect and even reaches the next corner. Consequently, this experiment shows that the excited edge state is topologically protected and thus robust against such lattice defects. To get an impression of what happens in the sample during propagation, in Fig. 5.5(c) a simulation of the output light distribution using BPM (for further details see Appendix) is shown at different points along z (at $z = 2\,\mathrm{cm}$, $z = 4\,\mathrm{cm}$, $z = 6\,\mathrm{cm}$, $z = 8\,\mathrm{cm}$, and $z = 10\,\mathrm{cm}$). Due to uncertainties of the refractive index profile of the waveguides, there are slight differences between the simulation and the experiment. In the simulation, after 10 cm, the edge state clearly has propagated a bit further compared to the experiment.

One of the key advantages of topological protection is its non-resonant nature. This allows for light across a broad spectral range to be handled with the same structure. We exploited this capability to gain insight into the propagation dynamics of light in our sample. To this end, we varied the excitation wavelength in the above described sample between $\lambda = 543\,\mathrm{nm}$ and $\lambda = 633\,\mathrm{nm}$, and observed the output distribution while keeping the injection fixed. When moving to higher wavelengths, the coupling constant between adjacent waveguides increases, thereby accelerating the transverse dynamics of the propagating wave packet. This effect is stronger than the reduction of vector potential which occurs when increasing the wavelength. The observed output images as depicted in Fig. 5.6 clearly show that the edge state moves along the edge. For $\lambda = 594\,\mathrm{nm}$, after 10 cm of propagation, it has reached the defect and for higher wavelengths it moves around the defect without being backscattered. For $\lambda = 633\,\mathrm{nm}$ the wave packet of the edge mode has passed the defect and moved further along the edge.

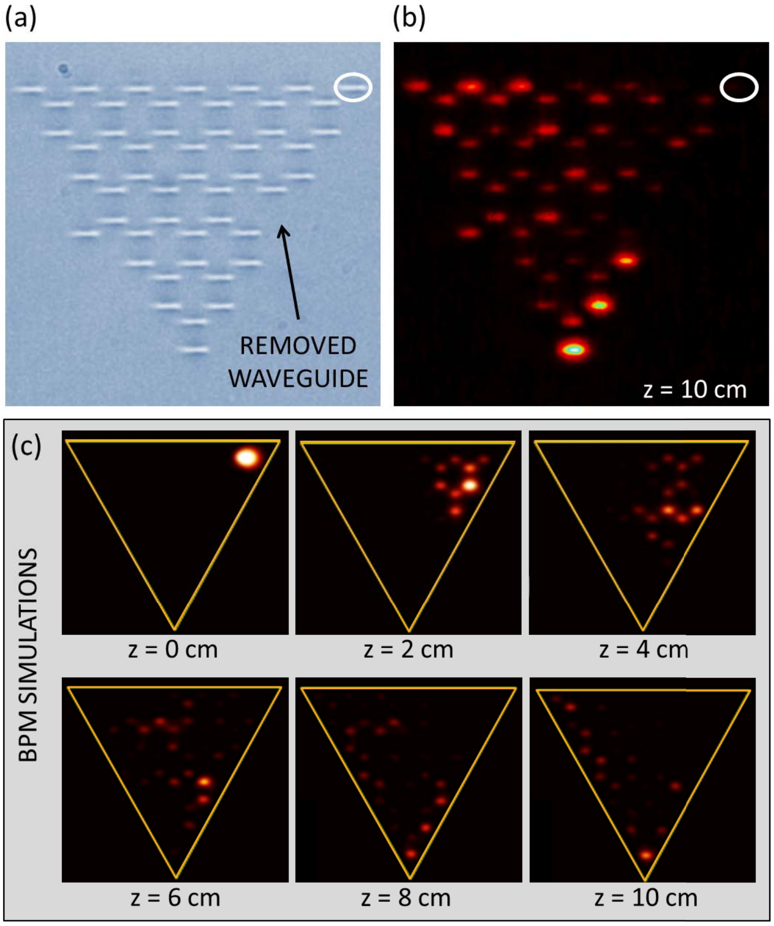

Figure 5.5: (a) Microscopic image of the front facet of the triangular lattice with one waveguide omitted during fabrication (removed waveguide), which acts as an edge defect. (b) Light distribution at the output facet ($z = 10\,\mathrm{cm}$) when the top right corner waveguide (marked by the white ellipse) is excited. The edge state has clearly passed the defect remaining confined. (c) Simulations of the light distribution at different positions along z applying BPM.

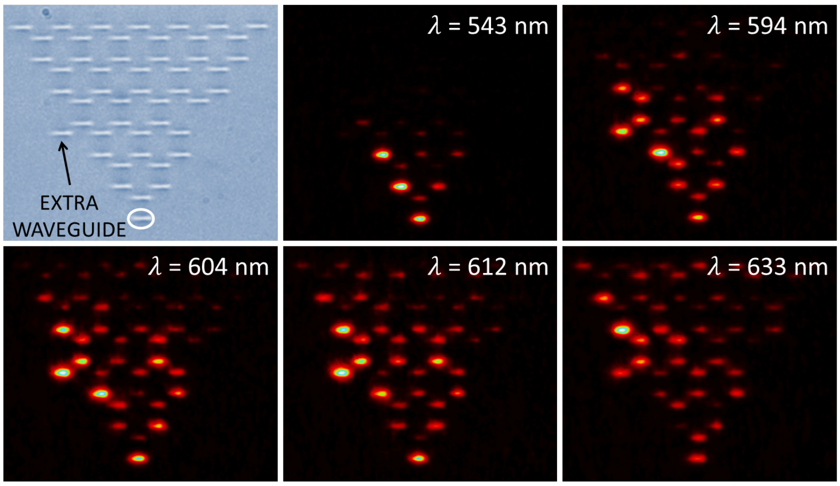

Figure 5.6: Effect of different input wavelength. Left panel: Microscopic image of the front facet of the triangular lattice with one extra waveguide added, acting as an edge defect. The white ellipse marks the initially excited waveguide in the here shown experiments. Other panels: Output light distribution for increasing wavelength resulting in growing coupling strength $c(\lambda)$. As the coupling strength increases, the edge wave packet experiences larger group velocity and can be seen “move past”the edge defect without backscattering.

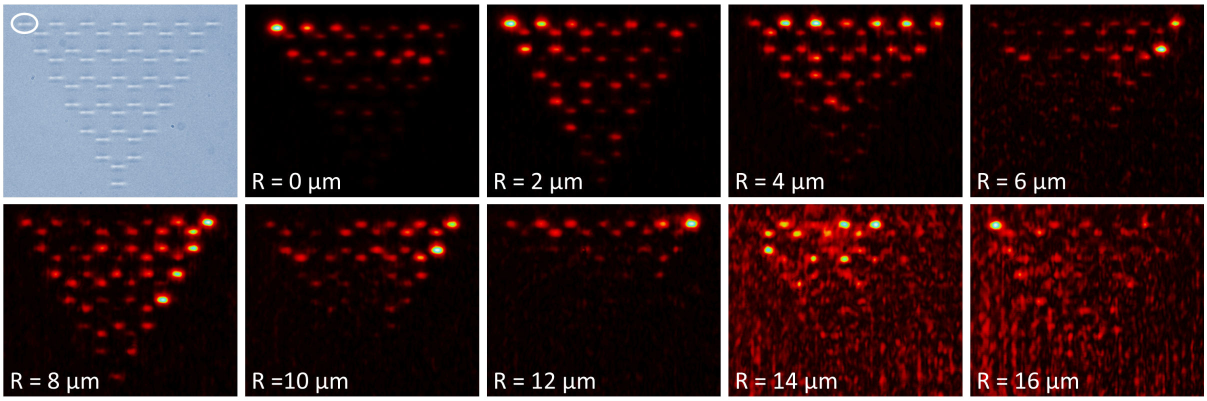

Figure 5.7: Changing the radius of the helical waveguide shape. Upper left panel: Microscopic image of the front facet of a triangular lattice structure with helical waveguides. The white ellipse marks the initially excited waveguide in the here shown experiments. Other panels: Light distribution at the output facet of several lattices each with a different helical waveguide radius (with numbers given in each panel). The distance which the edge state has travelled along the edge after 10 cm of propagation changes strongly, depending on the helical radius.

In the fourth experiment, the dependence of the transverse group velocity of the edge state on the helical radius of the waveguides is examined. For that purpose, several lattices with radii between $R = 0\,\mu\mathrm{m}$ and $R = 16\,\mu\mathrm{m}$ were fabricated. A microscopic image of the input facet of such a lattice is shown in Fig. 5.7 (upper left panel) with the waveguide in which light was injected marked by a white ellipse. In the non-helical case ($R = 0\,\mu\mathrm{m}$), the output light distribution shows bulk modes, as well as the edge state which does not transversally move during propagation. Note, that without helical trajectory of the waveguides, the edge state band is flat with degenerate eigenmodes such that any superposition of them behaves as an eigenmode. In contrast, the edge states of a Floquet topological insulator start to move clockwise along the edge while propagating along z as shown in the experimental output images in Fig. 5.7. The travelled transverse distance depends on the helical radius of the waveguides. In accordance to the theoretical results shown in Fig. 5.2(c), first with increasing radius the transverse movement of the edge state accelerates. The wave packet exhibits the highest transverse group velocity for a value of the radius lying between $R = 6\,\mu\mathrm{m}$ and $R = 10\,\mu\mathrm{m}$, while the theoretical result ($R = 10.3\,\mu\mathrm{m}$) is well within experimental error, given that this is a prediction from coupled-mode theory. At $R = 8\,\mu\mathrm{m}$, the wave packet has passed the corner of the triangle and has begun to move down the second edge. With further increasing radius a slow-down of the transverse group velocity can be observed until finally, at $R = 16\,\mu\mathrm{m}$, no transverse movement is experimentally observed meaning that the optical power is located at the excited corner waveguide. The qualitative behavior is in very good agreement with the theoretical results predicted using coupled mode theory. There are slight quantitative differences, as the maximum and the zero of the transverse group velocity is predicted at slightly higher values of the radius than found in the experiment. These differences can mainly be traced back to the fact that perfect adiabaticity is assumed for the coupled mode approach which cannot be achieved in experiments. The large background signal in the lower right panels of Fig. 5.7 is a result of bending losses which become stronger with increasing helix radius caused by the leaking of more and more optical power into scattering modes. The examination of the region with higher radii, where two counterclockwise propagating edge states are expected from theory, as discussed earlier, is prevented by the large background signal.

In summary, these data show topologically protected modes as they travel along the edge of the lattice. The observations clearly demonstrate the presence of a one-way edge state on the boundary of the photonic lattice that behaves according to theory. The edge transport is topologically robust in a way that it is not destroyed by different kinds of defects like missing lattice sites or 60° and 90° corners of the lattice edge geometry. It was demonstrated that the wave packet of the edge mode is neither backscattered nor scattered into the bulk when passing a defect. This robustness against perturbations is the key feature of topological protection. Furthermore, it was shown that the topologically protected edge state is a non-resonant feature. Taken together, the experiments unequivocally prove that the photonic graphene lattice with helical waveguides constitutes a photonic Floquet topological insulator.

This new class of photonic structures enables topological protection of light waves in the optical regime without the need of an external field. Consequently, photonic Floquet topological insulators open an entirely new platform upon which topological protection, a general wave effect clearly not confined to just solid-state systems, can be understood and probed. Topological transport with its special features can play a key role in the development of robust photonic devices being insensitive to disorder or fabrication errors. Furthermore, in the distant future photonics-on-chip might be a promising extremely fast-operating alternative to electronic signals in circuits and if so, topologically protected states could play a major role. Also applications in robust quantum computing were conceivable. Moreover, a use in single-mode lasers being independent of the cavity size might be enabled by the fact that the number of topological modes does not scale with the system size. Another promising field of application is slow-light technology, so far suffering strongly from scattering losses and localization due to disorder which both could be suppressed using chiral modes [108]. However, in the near future first of all very basic open questions have to be answered, concerning for example the behavior of entangled photons under topological protection or the effect of interactions on the robust transport. The realization of a photonic Floquet topological insulator presented here paves the way towards manifold applications and other realizations of topological protection in many different areas of physics.

6

CONCLUSION AND OUTLOOK

In condensed matter physics, the peculiar Dirac dynamics of electrons in graphene enables a plethora of novel applications, ranging from composite materials and optical electronics to photovoltaics and energy storage. In this thesis, I demonstrated that also in integrated photonics the unique structural properties of graphene open up new avenues. The transfer of the honeycomb lattice structure to an array of evanescently coupled waveguides carries over extraordinary physics from solid state graphene to optics. Thereby, "photonic graphene"enables the optical access of exploring physics based on the Dirac equation, in contrast to conventional optical lattices that are described by a Schrödinger-type dispersion. In this thesis, femtosecond laser written photonic graphene allowed me to explore various novel phenomena, based on the special band structure of the honeycomb lattice.

The main part of this work begins with Chapter 3, demonstrating the first experiments on a transition between different types of edge states when applying a linear strain to a honeycomb lattice. This transition is caused by the fusion of the two Dirac points in the band structure. During this process, the Berry phases exhibiting opposite sign at the two distinct singularities annihilate each other and a band gap forms. In the unperturbed graphene geometry, the two edge state types (zig-zag and bearded) are located in different regions of the edge band structure. Above the deformation threshold at which the Dirac points merge, the edge state between the Dirac points, the bearded state, ceases to exist, whereas the zig-zag edge state outside the Dirac points prevails and eventually resides on the entire band structure.

Chapter 4 introduces an alternate approach that utilizes non-uniform strain and succeeded in the realization of the first ultrastrong pseudomagnetic field in optics corresponding to a magnetic field strength of approximately 5500 T. Such high pseudomagnetic fields cannot be realized in conventional graphene, since the necessary deformations would lead to the disintegration of the entire lattice. The presence of these enormous field strengths gives rise to the formation of Landau levels as experimentally evidenced by robust transverse confinement of light at the armchair edge of the strained lattice. In addition to serving as indicators for the pseudomagnetic field, the Landau levels are highly degenerate – their extraordinary large density of states makes them promising for the realization of efficient nonlinear interactions enhanced by the Purcell effect. The degeneracies in the photonic band structure could lead to more efficient nonlinear optical devices and single-photon source efficiency, for example. More broadly, it was demonstrated that aperiodicity in photonic structures can much further enhance photonic crystals' originally intended uses.

The culmination of my work, as presented in Chapter 5, was the first realization of a photonic topological insulator with its hallmark feature of robust one-way light transport along the edges of the system. Crucially, the technique utilized here does not rely on external magnetic fields. Instead, the topologically protected edge states emerge due to a periodic external drive along the direction of propagation that breaks the z-reversal symmetry. As a result, this type of topological insulator can operate naturally at optical frequencies, thereby overcoming the two main challenges for adapting topological notions to real-world photonic applications. The unique transport properties in such systems hold immense potential for the improvement of various photonic functionalities, ranging from scattering-free waveguides and delay lines to isolators, couplers, advanced interconnects, unidirectional cavities and many more [108]. As the first and still one of the very few experimental realizations of photonic topological systems without the need of an external magnetic field [104, 109–111], the here introduced approach [97] denotes a big step forward. It already has spawned considerable interest in the community, as evidenced by numerous follow-up investigations concerning, e.g., the realization of topological insulators in other photonic systems [104, 109–111], nonlinear effects and gap solitons [112], topological states in non-Hermitian settings [113, 114] and in sub-wavelength-systems [115], the realization of higher Chern numbers [116], disorder-induced topological insulators [117], anomalous chiral states being connected to a Chern number of zero [110, 118, 119], and even 3D-photonic topological crystals exhibiting Weyl points were realized recently [120]. In summary, the waveguide based implementation of the topological insulator principle brought new impulses to the field of topological photonics. In addition, the principles shown here also inspired progress in other areas of physics, as e.g., cold atoms [121], optomechanics [122, 123], mechanics [124] and acoustics [125], where the ideas and methods developed in my work were fruitfully adapted in turn.

Future works in photonic graphene, as well as in other optical Dirac systems will indubitably include the general concept of gauge fields. This is not only of fundamental importance, but also promises novel degrees of freedom for innovative applications. Among the many open questions in this regard are the possibility of incorporating pseudomagnetic fields in photonic crystals and the interplay of topological states and non-Hermitian systems. In particular, understanding the behaviour of topological states under the influence of strong losses is of relevance for integrated-optical applications. Along these lines, waveguide-based implementations are once more a highly capable experimental platform, as they readily allow for the introduction of precisely predetermined amounts of losses through rapid modulation of the waveguide trajectory [113, 126]. Along different lines, the limits of topological robustness in the presence of different types of defects have to be explored in alternate approaches such as ring resonator networks or metamaterials, where spin-orbit coupling is emulated without genuine breaking of time-reversal symmetry. Including a third dimension to the design of topological systems is expected to open up new avenues of applications [108]. Considering that 1D waveguide systems based on quasicrystalline structures have been employed in demonstrating 2D topological phenomena [127], and theoretical proposals outline the possibility of realizing 4D topological physics in 2D systems [128], the prospects of exploring higher-dimensional topological photonics with the techniques utilized in my thesis are quite promising. Going beyond the honeycomb lattice, future investigations have a large variety of geometries to chose from when looking for structures that support Dirac points in reciprocal space. Examples such as the Lieb-, Kagome- or maple-leaf lattices [129] allow for even richer band structures. The capability to freely chose the underlying lattice geometry is one of the most important advantages of photonic systems – the possibilities arising from this flexibility are far from being exhausted.

In conclusion, my work has introduced new basic impulses to the field of optics. Inspired by solid state physics, the fundamental research on Dirac and topological photonics will continue to evolve above and beyond these fundamental notions and address the requirements of modern optics. Ultimately, the result will be a set of versatile tools for the design of compact highly efficient and robust photonic circuits.

BIBLIOGRAPHY

[1] K. S. Novoselov, A. K. Geim, S. V. Morozov, D. Jiang, Y. Zhang, S. V. Dubonos, I. V. Grigorieva, and A. A. Firsov, “Electric Field Effect in Atomically Thin Carbon Films,” Science **306**, 666 (2004).

[2] K. S. Novoselov, D. Jiang, F. Schedin, T. J. Booth, V. V. Khotkevich, S. V. Morozov, and A. K. Geim, “Two-dimensional atomic crystals,” Proceedings of the National Academy of Sciences of the United States of America **102**, 10451 (2005).

[3] “The 2010 Nobel Prize in Physics - Press Release,” Nobelprize.org. Nobel Media AB 2014. Web. 18 May 2016. <http://www.nobelprize.org/nobel_prizes/physics/laureates/2010/press.html> .

[4] A. K. Geim and K. S. Novoselov, “The rise of graphene,” Nat. Mater. **6**, 183 (2007).

[5] C. Lee, X. Wei, J. W. Kysar, and J. Hone, “Measurement of the Elastic Properties and Intrinsic Strength of Monolayer Graphene,” Science **321**, 385 (2008).

[6] A. A. Balandin, S. Ghosh, W. Bao, I. Calizo, D. Teweldebrhan, F. Miao, and C. N. Lau, “Superior Thermal Conductivity of Single-Layer Graphene,” Nano Letters **8**, 902 (2008).

[7] K. S. Novoselov, A. K. Geim, S. V. Morozov, D. Jiang, M. I. Katsnelson, I. V. Grigorieva, S. V. Dubonos, and A. A. Firsov, “Two-dimensional gas of massless Dirac fermions in graphene,” Nature **438**, 197 (2005).

[8] R. R. Nair, P. Blake, A. N. Grigorenko, K. S. Novoselov, T. J. Booth, T. Stauber, N. M. R. Peres, and A. K. Geim, “Fine Structure Constant Defines Visual Transparency of Graphene,” Science **320**, 1308 (2008).

[9] Y. Zhang, Y.-W. Tan, H. L. Stormer, and P. Kim, “Experimental observation of the quantum Hall effect and Berry’s phase in graphene,” Nature **438**, 201 (2005).

[10] A. F. Young and P. Kim, “Quantum interference and Klein tunnelling in graphene heterojunctions,” Nat. Phys. **5**, 222 (2009).

[11] O. Klein, “Die Reflexion von Elektronen an einem Potentialsprung nach der relativistischen Dynamik von Dirac,” Zeitschrift für Physik **53**, 157 (1929).

[12] M. I. Katsnelson, “Zitterbewegung, chirality, and minimal conductivity in graphene,” The European Physical Journal B - Condensed Matter and Complex Systems **51**, 157 (2006).

[13] M. I. Katsnelson, K. S. Novoselov, and A. K. Geim, “Chiral tunnelling and the Klein paradox in graphene,” Nat. Phys. **2**, 620 (2006).

[14] J. Tworzydło, B. Trauzettel, M. Titov, A. Rycerz, and C. W. J. Beenakker, “Sub-Poissonian Shot Noise in Graphene,” Phys. Rev. Lett. **96**, 246802 (2006).

[15] P. Recher, B. Trauzettel, A. Rycerz, Y. M. Blanter, C. W. J. Beenakker, and A. F. Morpurgo, “Aharonov-Bohm effect and broken valley degeneracy in graphene rings,” Phys. Rev. B **76**, 235404 (2007).

[16] F. Schwierz, “Graphene transistors,” Nat. Nanotechnol. **5**, 487 (2010).

[17] P. R. Wallace, “The Band Theory of Graphite,” Phys. Rev. **71**, 622 (1947).

[18] M. Katsnelson, *Graphene: Carbon in Two Dimensions*, Cambridge University Press (2012).

[19] S. Reich, J. Maultzsch, C. Thomsen, and P. Ordejón, “Tight-binding description of graphene,” Phys. Rev. B **66**, 035412 (2002).

[20] L. Van Hove, “The Occurrence of Singularities in the Elastic Frequency Distribution of a Crystal,” Phys. Rev. **89**, 1189 (1953).

[21] N. M. R. Peres, “*Colloquium* : The transport properties of graphene: An introduction,” Rev. Mod. Phys. **82**, 2673 (2010).

[22] K. A. Ritter and J. W. Lyding, “The influence of edge structure on the electronic properties of graphene quantum dots and nanoribbons,” Nat. Mater. **8**, 235 (2009).

[23] M. Nakahara, *Geometry, Topology and Physics, Second Edition*, Graduate student

series in physics, Taylor & Francis (2003).

[24] K. v. Klitzing, G. Dorda, and M. Pepper, “New Method for High-Accuracy Determination of the Fine-Structure Constant Based on Quantized Hall Resistance,” Phys. Rev. Lett. **45**, 494 (1980).

[25] R. B. Laughlin, “Quantized Hall conductivity in two dimensions,” Phys. Rev. B **23**, 5632 (1981).

[26] D. J. Thouless, M. Kohmoto, M. P. Nightingale, and M. den Nijs, “Quantized Hall Conductance in a Two-Dimensional Periodic Potential,” Phys. Rev. Lett. **49**, 405 (1982).

[27] J. Bellissard, A. van Elst, and H. Schulz-Baldes, “The noncommutative geometry of the quantum Hall effect,” Journal of Mathematical Physics **35**, 5373 (1994).

[28] Y. Hatsugai, “Bulk-edge correspondence in graphene with/without magnetic field: Chiral symmetry, Dirac fermions and edge states,” Solid State Communications **149**, 1061 (2009).

[29] M. V. Berry, “Quantal Phase Factors Accompanying Adiabatic Changes,” Proceedings of the Royal Society of London A: Mathematical, Physical and Engineering Sciences **392**, 45 (1984).

[30] J. Zak, “Berry’s phase for energy bands in solids,” Phys. Rev. Lett. **62**, 2747 (1989).

[31] P. Delplace, D. Ullmo, and G. Montambaux, “Zak phase and the existence of edge states in graphene,” Phys. Rev. B **84**, 195452 (2011).

[32] Z. Liu, K. Suenaga, P. J. F. Harris, and S. Iijima, “Open and Closed Edges of Graphene Layers,” Phys. Rev. Lett. **102**, 015501 (2009).

[33] D. Klein, “Graphitic polymer strips with edge states,” Chemical Physics Letters **217**, 261 (1994).

[34] M. Fujita, K. Wakabayashi, K. Nakada, and K. Kusakabe, “Peculiar Localized State at Zigzag Graphite Edge,” Journal of the Physical Society of Japan **65**, 1920 (1996).

[35] S. Ryu and Y. Hatsugai, “Topological Origin of Zero-Energy Edge States in Particle-Hole Symmetric Systems,” Phys. Rev. Lett. **89**, 077002 (2002).

[36] S. Ryu and Y. Hatsugai, "Zero-energy edge states and chiral symmetry breaking at edges of graphite sheets," Physica E: Low-dimensional Systems and Nanostructures **22**, 679 , 15th International Conference on Electronic Propreties of Two-Dimensional Systems (EP2DS-15) (2004).

[37] M. Kohmoto and Y. Hasegawa, "Zero modes and edge states of the honeycomb lattice," Phys. Rev. B **76**, 205402 (2007).

[38] R. S. K. Mong and V. Shivamoggi, "Edge states and the bulk-boundary correspondence in Dirac Hamiltonians," Phys. Rev. B **83**, 125109 (2011).

[39] J. M. Zeuner, M. C. Rechtsman, S. Nolte, and A. Szameit, "Edge states in disordered photonic graphene," Opt. Lett. **39**, 602 (2014).

[40] R. Rammal, G. Toulouse, M. T. Jaekel, and B. I. Halperin, "Quantized Hall conductance and edge states: Two-dimensional strips with a periodic potential," Phys. Rev. B **27**, 5142 (1983).

[41] Y. Hatsugai, "Edge states in the integer quantum Hall effect and the Riemann surface of the Bloch function," Phys. Rev. B **48**, 11851 (1993).

[42] Y. Zheng and T. Ando, "Hall conductivity of a two-dimensional graphite system," Phys. Rev. B **65**, 245420 (2002).

[43] V. P. Gusynin and S. G. Sharapov, "Unconventional Integer Quantum Hall Effect in Graphene," Phys. Rev. Lett. **95**, 146801 (2005).

[44] N. Peres, F. Guinea, and A. C. Neto, "Electronic properties of two-dimensional carbon," Annals of Physics **321**, 1559 (2006).

[45] K. S. Novoselov, Z. Jiang, Y. Zhang, S. V. Morozov, H. L. Stormer, U. Zeitler, J. C. Maan, G. S. Boebinger, P. Kim, and A. K. Geim, "Room-Temperature Quantum Hall Effect in Graphene," Science **315**, 1379 (2007).

[46] F. D. M. Haldane, "Model for a Quantum Hall Effect without Landau Levels: Condensed-Matter Realization of the "Parity Anomaly"," Phys. Rev. Lett. **61**, 2015 (1988).

[47] C. L. Kane and E. J. Mele, "Quantum Spin Hall Effect in Graphene," Phys. Rev. Lett. **95**, 226801 (2005).

[48] B. A. Bernevig, T. L. Hughes, and S.-C. Zhang, "Quantum Spin Hall Effect and Topological Phase Transition in HgTe Quantum Wells," Science **314**, 1757 (2006).

[49] M. König, S. Wiedmann, C. Brüne, A. Roth, H. Buhmann, L. W. Molenkamp, X.-L. Qi, and S.-C. Zhang, "Quantum Spin Hall Insulator State in HgTe Quantum Wells," Science **318**, 766 (2007).

[50] M. Z. Hasan and C. L. Kane, "*Colloquium* : Topological insulators," Rev. Mod. Phys. **82**, 3045 (2010).

[51] X.-L. Qi and S.-C. Zhang, "Topological insulators and superconductors," Rev. Mod. Phys. **83**, 1057 (2011).

[52] A. B. Khanikaev, R. Fleury, S. H. Mousavi, and A. Alu, "Topologically robust sound propagation in an angular-momentum-biased graphene-like resonator lattice," Nat. Commun. **6**, 8260 (2015).

[53] M. Polini, F. Guinea, M. Lewenstein, H. C. Manoharan, and V. Pellegrini, "Artificial honeycomb lattices for electrons, atoms and photons," Nat. Nanotechnol. **8**, 625 (2013).

[54] D. Torrent and J. Sánchez-Dehesa, "Acoustic Analogue of Graphene: Observation of Dirac Cones in Acoustic Surface Waves," Phys. Rev. Lett. **108**, 174301 (2012).

[55] R. A. Sepkhanov, Y. B. Bazaliy, and C. W. J. Beenakker, "Extremal transmission at the Dirac point of a photonic band structure," Phys. Rev. A **75**, 063813 (2007).

[56] U. Kuhl, S. Barkhofen, T. Tudorovskiy, H.-J. Stöckmann, T. Hossain, L. de Forges de Parny, and F. Mortessagne, "Dirac point and edge states in a microwave realization of tight-binding graphene-like structures," Phys. Rev. B **82**, 094308 (2010).

[57] L. Tarruell, D. Greif, T. Uehlinger, G. Jotzu, and T. Esslinger, "Creating, moving and merging Dirac points with a Fermi gas in a tunable honeycomb lattice," Nature **483**, 302 (2012).

[58] K. K. Gomes, W. Mar, W. Ko, F. Guinea, and H. C. Manoharan, "Designer Dirac fermions and topological phases in molecular graphene," Nature **483**, 306 (2012).

[59] T. Jacqmin, I. Carusotto, I. Sagnes, M. Abbarchi, D. D. Solnyshkov, G. Malpuech, E. Galopin, A. Lemaître, J. Bloch, and A. Amo, "Direct Observation of Dirac

Cones and a Flatband in a Honeycomb Lattice for Polaritons," Phys. Rev. Lett. **112**, 116402 (2014).

[60] M. Schmidt, V. Peano, and F. Marquardt, "Optomechanical Dirac physics," New Journal of Physics **17**, 023025 (2015).

[61] O. Peleg, G. Bartal, B. Freedman, O. Manela, M. Segev, and D. N. Christodoulides, "Conical Diffraction and Gap Solitons in Honeycomb Photonic Lattices," Phys. Rev. Lett. **98**, 103901 (2007).

[62] J. M. Zeuner, M. C. Rechtsman, R. Keil, F. Dreisow, A. Tünnermann, S. Nolte, and A. Szameit, "Negative coupling between defects in waveguide arrays," Opt. Lett. **37**, 533 (2012).

[63] R. Keil, C. Poli, M. Heinrich, J. Arkinstall, G. Weihs, H. Schomerus, and A. Szameit, "Universal Sign Control of Coupling in Tight-Binding Lattices," Phys. Rev. Lett. **116**, 213901 (2016).

[64] J. M. Zeuner, N. K. Efremidis, R. Keil, F. Dreisow, D. N. Christodoulides, A. Tünnermann, S. Nolte, and A. Szameit, "Optical Analogues for Massless Dirac Particles and Conical Diffraction in One Dimension," Phys. Rev. Lett. **109**, 023602 (2012).

[65] F. Dreisow, M. Heinrich, R. Keil, A. Tünnermann, S. Nolte, S. Longhi, and A. Szameit, "Classical Simulation of Relativistic *Zitterbewegung* in Photonic Lattices," Phys. Rev. Lett. **105**, 143902 (2010).

[66] R. Keil, J. M. Zeuner, F. Dreisow, M. Heinrich, A. Tünnermann, S. Nolte, and A. Szameit, "The random mass Dirac model and long-range correlations on an integrated optical platform," Nat. Commun. **4**, 1368 (2013).

[67] D. N. Christodoulides and R. I. Joseph, "Discrete self-focusing in nonlinear arrays of coupled waveguides," Opt. Lett. **13**, 794 (1988).

[68] F. Lederer, G. I. Stegeman, D. N. Christodoulides, G. Assanto, M. Segev, and Y. Silberberg, "Discrete solitons in optics," Physics Reports **463**, 1 (2008).

[69] A. L. Jones, "Coupling of Optical Fibers and Scattering in Fibers," J. Opt. Soc. Am. **55**, 261 (1965).

[70] A. Szameit, *Light Propagation in Two-dimensional Waveguide Arrays*, BoD–Books on

Demand (2008).

[71] N. Levy, S. A. Burke, K. L. Meaker, M. Panlasigui, A. Zettl, F. Guinea, A. H. C. Neto, and M. F. Crommie, "Strain-Induced Pseudo-Magnetic Fields Greater Than 300 Tesla in Graphene Nanobubbles," Science **329**, 544 (2010).

[72] Y. Kobayashi, K.-i. Fukui, T. Enoki, K. Kusakabe, and Y. Kaburagi, "Observation of zigzag and armchair edges of graphite using scanning tunneling microscopy and spectroscopy," Phys. Rev. B **71**, 193406 (2005).

[73] C. Tao, L. Jiao, O. V. Yazyev, Y.-C. Chen, J. Feng, X. Zhang, R. B. Capaz, J. M. Tour, A. Zettl, S. G. Louie, H. Dai, and M. F. Crommie, "Spatially resolving edge states of chiral graphene nanoribbons," Nat. Phys. **7**, 616 (2011).

[74] K. He, A. W. Robertson, S. Lee, E. Yoon, G.-D. Lee, and J. H. Warner, "Extended Klein Edges in Graphene," ACS Nano **8**, 12272 (2014).

[75] Y. Plotnik, M. C. Rechtsman, D. Song, M. Heinrich, J. M. Zeuner, S. Nolte, Y. Lumer, N. Malkova, J. Xu, A. Szameit, Z. Chen, and M. Segev, "Observation of unconventional edge states in 'photonic graphene'," Nat. Mater. **13**, 57 (2014).

[76] Y. V. Kartashov, J. M. Zeuner, A. Szameit, V. A. Vysloukh, and L. Torner, "Light scattering in disordered honeycomb photonic lattices near the Dirac points," Opt. Lett. **38**, 3727 (2013).

[77] K. Itoh, W. Watanabe, S. Nolte, and C. B. Schaffer, "Ultrafast Processes for Bulk Modification of Transparent Materials," MRS Bulletin **31**, 620 (2006).

[78] J. W. Chan, T. Huser, S. Risbud, and D. M. Krol, "Structural changes in fused silica after exposure to focused femtosecond laser pulses," Opt. Lett. **26**, 1726 (2001).

[79] J. Chan, T. Huser, S. Risbud, and D. Krol, "Modification of the fused silica glass network associated with waveguide fabrication using femtosecond laser pulses," Applied Physics A **76**, 367 (2003).

[80] K. M. Davis, K. Miura, N. Sugimoto, and K. Hirao, "Writing waveguides in glass with a femtosecond laser," Opt. Lett. **21**, 1729 (1996).

[81] A. Szameit and S. Nolte, "Discrete optics in femtosecond-laser-written photonic structures," Journal of Physics B: Atomic, Molecular and Optical Physics **43**, 163001 (2010).

[82] I. Mansour and F. Caccavale, "An improved procedure to calculate the refractive index profile from the measured near-field intensity," Journal of Lightwave Technology **14**, 423 (1996).

[83] A. Szameit, F. Dreisow, M. Heinrich, T. Pertsch, S. Nolte, A. Tünnermann, E. Suran, F. Louradour, A. Barthélémy, and S. Longhi, "Image reconstruction in segmented femtosecond laser-written waveguide arrays," Applied Physics Letters **93**, 181109 (2008).

[84] A. Szameit, I. L. Garanovich, M. Heinrich, A. A. Sukhorukov, F. Dreisow, T. Pertsch, S. Nolte, A. Tünnermann, S. Longhi, and Y. S. Kivshar, "Observation of Two-Dimensional Dynamic Localization of Light," Phys. Rev. Lett. **104**, 223903 (2010).

[85] M. Heinrich, A. Szameit, F. Dreisow, R. Keil, S. Minardi, T. Pertsch, S. Nolte, A. Tünnermann, and F. Lederer, "Observation of Three-Dimensional Discrete-Continuous X Waves in Photonic Lattices," Phys. Rev. Lett. **103**, 113903 (2009).

[86] U. Naether, J. M. Meyer, S. Stützer, A. Tünnermann, S. Nolte, M. I. Molina, and A. Szameit, "Anderson localization in a periodic photonic lattice with a disordered boundary," Opt. Lett. **37**, 485 (2012).

[87] M. C. Rechtsman, Y. Plotnik, J. M. Zeuner, D. Song, Z. Chen, A. Szameit, and M. Segev, "Topological Creation and Destruction of Edge States in Photonic Graphene," Phys. Rev. Lett. **111**, 103901 (2013).

[88] O. Bahat-Treidel, O. Peleg, and M. Segev, "Symmetry breaking in honeycomb photonic lattices," Opt. Lett. **33**, 2251 (2008).

[89] C. L. Kane and E. J. Mele, "Size, Shape, and Low Energy Electronic Structure of Carbon Nanotubes," Phys. Rev. Lett. **78**, 1932 (1997).

[90] F. Guinea, M. I. Katsnelson, and A. K. Geim, "Energy gaps and a zero-field quantum Hall effect in graphene by strain engineering," Nat. Phys. **6**, 30 (2010).

[91] M. C. Rechtsman, J. M. Zeuner, A. Tünnermann, S. Nolte, M. Segev, and A. Szameit, "Strain-induced pseudomagnetic field and photonic Landau levels in dielectric structures," Nat. Photon. **7**, 153 (2013).

[92] M. Stone, *Quantum Hall Effect*, World Scientific (1992).

[93] A. R. Akhmerov and C. W. J. Beenakker, "Boundary conditions for Dirac fermions

on a terminated honeycomb lattice," Phys. Rev. B **77**, 085423 (2008).

[94] S. G. Johnson, S. Fan, P. R. Villeneuve, J. D. Joannopoulos, and L. A. Kolodziejski, "Guided modes in photonic crystal slabs," Phys. Rev. B **60**, 5751 (1999).

[95] P. Lodahl, A. Floris van Driel, I. S. Nikolaev, A. Irman, K. Overgaag, D. Vanmaekelbergh, and W. L. Vos, "Controlling the dynamics of spontaneous emission from quantum dots by photonic crystals," Nature **430**, 654 (2004).

[96] E. M. Purcell, H. C. Torrey, and R. V. Pound, "Resonance Absorption by Nuclear Magnetic Moments in a Solid," Phys. Rev. **69**, 37 (1946).

[97] M. C. Rechtsman, J. M. Zeuner, Y. Plotnik, Y. Lumer, D. Podolsky, F. Dreisow, S. Nolte, M. Segev, and A. Szameit, "Photonic Floquet topological insulators," Nature **496**, 196 (2013).

[98] F. D. M. Haldane and S. Raghu, "Possible Realization of Directional Optical Waveguides in Photonic Crystals with Broken Time-Reversal Symmetry," Phys. Rev. Lett. **100**, 013904 (2008).

[99] M. Hafezi, E. A. Demler, M. D. Lukin, and J. M. Taylor, "Robust optical delay lines with topological protection," Nat. Phys. **7**, 907 (2011).

[100] L. Lu, J. D. Joannopoulos, and M. Soljačić, "Topological photonics," Nat. Photon. **8**, 821 (2014).

[101] Z. Wang, Y. Chong, J. D. Joannopoulos, and M. Soljačić, "Observation of unidirectional backscattering-immune topological electromagnetic states," Nature **461**, 772 (2009).

[102] A. B. Khanikaev, S. Hossein Mousavi, W.-K. Tse, M. Kargarian, A. H. MacDonald, and G. Shvets, "Photonic topological insulators," Nat. Mater. **12**, 233 (2013).

[103] K. Fang, Z. Yu, and S. Fan, "Realizing effective magnetic field for photons by controlling the phase of dynamic modulation," Nat. Photon. **6**, 782 (2012).

[104] M. Hafezi, S. Mittal, J. Fan, A. Migdall, and J. M. Taylor, "Imaging topological edge states in silicon photonics," Nat. Photon. **7**, 1001 (2013).

[105] N. H. Lindner, G. Refael, and V. Galitski, "Floquet topological insulator in semiconductor quantum wells," Nat. Phys. **7**, 490 (2011).

[106] Z. Gu, H. A. Fertig, D. P. Arovas, and A. Auerbach, "Floquet Spectrum and Transport through an Irradiated Graphene Ribbon," Phys. Rev. Lett. **107**, 216601 (2011).

[107] E. Akkermans and G. Montambaux, *Mesoscopic Physics of Electrons and Photons*, Cambridge University Press (2007).

[108] L. Lu, J. D. Joannopoulos, and M. Soljačić, "Topological states in photonic systems," Nat. Phys. **12**, 626 (2016).

[109] W.-J. Chen, S.-J. Jiang, X.-D. Chen, B. Zhu, L. Zhou, J.-W. Dong, and C. T. Chan, "Experimental realization of photonic topological insulator in a uniaxial metacrystal waveguide," Nat. Commun. **5**, 5782 (2014).

[110] F. Gao, Z. Gao, X. Shi, Z. Yang, X. Lin, H. Xu, J. D. Joannopoulos, M. Soljačić, H. Chen, L. Lu, Y. Chong, and B. Zhang, "Probing topological protection using a designer surface plasmon structure," Nat. Commun. **7**, 11619 (2016).

[111] A. P. Slobozhanyuk, A. B. Khanikaev, D. S. Filonov, D. A. Smirnova, A. E. Miroshnichenko, and K. Y. S., "Experimental demonstration of topological effects in bianisotropic metamaterials," Scientific Reports **6** (2016).

[112] Y. Lumer, Y. Plotnik, M. C. Rechtsman, and M. Segev, "Self-Localized States in Photonic Topological Insulators," Phys. Rev. Lett. **111**, 243905 (2013).

[113] J. M. Zeuner, M. C. Rechtsman, Y. Plotnik, Y. Lumer, S. Nolte, M. S. Rudner, M. Segev, and A. Szameit, "Observation of a Topological Transition in the Bulk of a Non-Hermitian System," Phys. Rev. Lett. **115**, 040402 (2015).

[114] S. Weimann, M. Rechtsman, Y. Plotnik, Y. Lumer, K. Makris, M. Segev, and A. Szameit, "Parity-time (PT) symmetric topological interface states," "CLEO: 2015," FTu2C.7, Optical Society of America (2015).

[115] A. P. Slobozhanyuk, A. N. Poddubny, A. E. Miroshnichenko, P. A. Belov, and Y. S. Kivshar, "Subwavelength Topological Edge States in Optically Resonant Dielectric Structures," Phys. Rev. Lett. **114**, 123901 (2015).

[116] S. A. Skirlo, L. Lu, Y. Igarashi, Q. Yan, J. Joannopoulos, and M. Soljačić, "Experimental Observation of Large Chern Numbers in Photonic Crystals," Phys. Rev. Lett. **115**, 253901 (2015).

[117] P. Titum, N. H. Lindner, M. C. Rechtsman, and G. Refael, “Disorder-Induced Floquet Topological Insulators,” Phys. Rev. Lett. **114**, 056801 (2015).

[118] L. J. Maczewsky, J. M. Zeuner, S. Nolte, and A. Szameit, “Observation of photonic anomalous Floquet Topological Insulators,” ArXiv e-prints (2016).

[119] S. Mukherjee, A. Spracklen, M. Valiente, E. Andersson, P. Öhberg, N. Goldman, and R. R. Thomson, “Experimental observation of anomalous topological edge modes in a slowly-driven photonic lattice,” ArXiv e-prints (2016).

[120] L. Lu, Z. Wang, D. Ye, L. Ran, L. Fu, J. D. Joannopoulos, and M. Soljačić, “Experimental observation of Weyl points,” Science **349**, 622 (2015).

[121] G. Jotzu, M. Messer, R. Desbuquois, M. Lebrat, T. Uehlinger, D. Greif, and T. Esslinger, “Experimental realization of the topological Haldane model with ultracold fermions,” Nature **515**, 237 (2014).

[122] V. Peano, C. Brendel, M. Schmidt, and F. Marquardt, “Topological Phases of Sound and Light,” Phys. Rev. X **5**, 031011 (2015).

[123] M. Schmidt, S. Kessler, V. Peano, O. Painter, and F. Marquardt, “Optomechanical creation of magnetic fields for photons on a lattice,” Optica **2**, 635 (2015).

[124] R. Süsstrunk and S. D. Huber, “Observation of phononic helical edge states in a mechanical topological insulator,” Science **349**, 47 (2015).

[125] R. Fleury, A. B. Khanikaev, and A. Alu, “Floquet topological insulators for sound,” Nat. Commun. **7**, 11744 (2016).

[126] T. Eichelkraut, S. Weimann, S. Stützer, S. Nolte, and A. Szameit, “Radiation-loss management in modulated waveguides,” Opt. Lett. **39**, 6831 (2014).

[127] Y. E. Kraus, Y. Lahini, Z. Ringel, M. Verbin, and O. Zilberberg, “Topological States and Adiabatic Pumping in Quasicrystals,” Phys. Rev. Lett. **109**, 106402 (2012).

[128] Y. E. Kraus, Z. Ringel, and O. Zilberberg, “Four-Dimensional Quantum Hall Effect in a Two-Dimensional Quasicrystal,” Phys. Rev. Lett. **111**, 226401 (2013).

[129] K. Asano and C. Hotta, “Designing Dirac points in two-dimensional lattices,” Phys. Rev. B **83**, 245125 (2011).

[130] K. Kawano and T. Kitoh, *Introduction to Optical Waveguide Analysis: Solving*

Maxwell's Equation and the Schrödinger Equation, Wiley (2004).

[131] R. Kosloff and D. Kosloff, "Absorbing boundaries for wave propagation problems," Journal of Computational Physics **63**, 363 (1986).

[132] A. Szameit, *Dirac dynamics in photonic waveguide lattices*, Habilitation, Friedrich-Schiller-Universität Jena (2015).

APPENDIX

CONTINUUM SIMULATIONS APPLYING BPM

A way to describe the light propagation in the applied photonic arrays are the coupled mode equations. However, if a more realistically simulation of experimental conditions is required, full-wave continuum simulations applying a beam propagation method (BPM) [130] are performed. The algorithm is based on the paraxial Helmholtz equation with the full refractive index profile of the waveguide array. The waveguides themselves are embedded in a fused silica bulk material, which has a refractive index of $n_0 = 1.45$ at a wavelength of $\lambda = 633\,\text{nm}$. There is a smooth increase of refractive index building up the waveguides which reaches its maximum in their center with approximately $\Delta n = 10^{-3}$. The refractive index increase profile of a typical waveguide as used within this thesis is characterized by the following hypergaussian refractive index profile $\Delta n_w(\vec{r})$:

$$\Delta n_w(\vec{r}) = \Delta n \exp\left(-\left[\left(\frac{x}{r_1}\right)^2 + \left(\frac{y}{r_2}\right)^2\right]^3\right),$$

where r_1 is the waveguide radius in x-direction, and r_2 in y-direction. Typical values of the waveguide radii, as applied in this work, are $r_1 = 2\,\mu\text{m}$ and $r_2 = 5\,\mu\text{m}$. However, these values are not fixed, but depend on the fabrication parameters as also the maximum refractive index change Δn does. The waveguides themselves are embedded in a fused silica bulk material, which has a refractive index of $n_0 = 1.45$ at a wavelength of $\lambda = 633\,\text{nm}$. With this refractive index profile and an initial input beam configuration $\psi_0(\vec{r})$ given, one can now start to solve the paraxial Helmholtz equation:

$$i\partial_z\psi(\vec{r},z) = -\frac{1}{2k_0}\nabla_T{}^2\psi(\vec{r},z) - \frac{k_0\Delta n(\vec{r},z)}{n_0}\psi(\vec{r},z). \tag{6.1}$$

In order to describe the numerical simulation method of the light dynamics in detail, first the paraxial Helmholtz equation can be rewritten in order to simplify the notation:

$$i\partial_z\psi = (T+V)\,\psi,$$

where $T\psi$ (referred to as the kinetic term) is the first term on the right-hand side of Eq. (6.1), and $V\psi$ (referred to as the potential term) is the second one. The formal integration of this equation yields $\psi = \exp\left(-i(T+V)z\right)\psi_0$, being in general only achievable numerically since T and V do not commute. For small steps, Δz, the wavefunction can be evolved forward in time using the Trotter-Suzuki approximation:

$$\psi = \mathrm{e}^{-iT\frac{\Delta z}{2}}\mathrm{e}^{-iV\Delta z}\mathrm{e}^{-iT\frac{\Delta z}{2}}\psi_0 + \mathcal{O}\left(\Delta z^3\right).$$

For longer times, the operator can therefore simply be iteratively multiplied:

$$\psi \approx \mathrm{e}^{-iT\frac{\Delta z}{2}}\mathrm{e}^{-iV\Delta z}\mathrm{e}^{-iT\Delta z}...\,\mathrm{e}^{-iT\Delta z}\mathrm{e}^{-iV\Delta z}\mathrm{e}^{-iT\frac{\Delta z}{2}}\psi_0,$$

where the approximate evolution operator is applied N times with $z = N\Delta z$. The advantage of using this iterative method is that since V is an operator that is diagonal in real space, the operation $\mathrm{e}^{-iV\Delta z}$ can be applied by a simple scalar multiplication, and since T is diagonal in Fourier space, the operation $\mathrm{e}^{-iT\Delta z}$ can be applied by a simple multiplication of the Fourier-transformed wavefunction. With this technique, not only the guided modes are taken into account, but also the continuum modes corresponding to the loss of the waveguides. To effectively describe the experiments, the simulation uses absorbing boundary conditions in a manner akin to [131]. In particular, a position-dependent damping of the wavefunction is applied such that strong decay occurs at the boundary, while choosing a decay length such that reflections are minimized. This effectively describes experimental conditions since in the experiment, when radiating waves leave a waveguide array, they simply never return to the array and can therefore be neglected.

ACKNOWLEDGEMENTS

The process towards a doctorate is supported by a lot of people to which I would like to give many thanks at that point.

First and foremost, it is a pleasure to express my deep gratitude to my supervisor Prof. Dr. Alexander Szameit for his outstanding support, for his enduring willingness to answer questions, for his numerous ideas, and simply for his encouraging way of doing physics and for passing this enthusiasm on to his students.

Further thanks go to Prof. Dr. Stefan Nolte as the head of the Ultrafast Optics department for offering our subgroup the possibility to use the laser equipment in the lab and for fruitful discussions. I also want to thank Prof. Dr. Andreas Tünnermann, the head of the Institute of Applied Physics and the Fraunhofer Institute for Applied Optics and Precision Engineering for recommending me Prof. Szameit's group as an interesting option to graduate.

I am indebted to all the collaborators participating in this work. Especially I am grateful to Prof. Dr. Mikael Rechtsman without whose theoretical expertise and excellent knowledge of the waveguide lattice systems this work would not have been possible. I am very grateful to Prof. Dr. Mordechai Segev who welcomed me in his group at the Technion for an instructive stay providing me, among others, a lot more insight into the theoretical aspects of topology. Here, I would like to name especially Yonatan Plotnik and Yakov Lumer and thank them for the fruitful discussions and explanations during the time in Haifa. Furthermore, I also would like to thank Mikael Rechtsman for the helpful discussions and his efforts organizing the surrounding conditions of my stay in Israel.

Extremely important is the versatile support by my office and group mates - Markus Gräfe, Dr. Matthias Heinrich, René Heilmann, Steffen Weimann, Christian Vetter, Dr. Felix Dreisow, Dr. Robert Keil, Arthur Jungkind and all the other colleagues from the group. They deserve a big thank you for helping out in the lab when the laser system had an off day or when other technical problems appeared, for numerous discussions about physics and about all the other important issues, and simply for the many cheerful hours during the last years.

I feel obliged to express my gratitude towards Christiane Otto for the diligent and fast preparation of samples, as well as towards Bodo Martin and his changing peers for caring for the computers of the institute.

I also wish to extend my heartfelt gratitude to my parents, not merely for the special motivation announcing a selected bottle of wine for the first one of the family - my brother or me - to achieve the doctoral degree, but rather for their permanent and great support on the long way to this point.

Lastly, but most importantly, from the very deep of my heart I wish to thank my husband Thomas for his help, for encouraging me when my motivation was low, and for being there for me, whenever needed. Although not exactly speeding up this thesis, I am deeply grateful to my little son Justus, remembering me every day what life is all about.

ZUSAMMENFASSUNG

Das erste realisierte Material, das aus einer einzigen Schicht Atome besteht, heißt Graphen [1, 2]. Es besitzt solch außergewöhnliche Eigenschaften, dass A. Geim und K. Novoselov 2010 den Physik-Nobelpreis für seine Entdeckung und Erforschung erhielten [1–3]. Dabei spielt die Honigwabenstruktur, in der die Atome angeordnet sind, bzw. die daraus resultierende Bandstruktur von Graphen eine besondere Rolle: durch die Schnittpunkte der zwei spiegelgleichen Bänder am Fermi-Energielevel und dem konischen Bandverlauf in der Umgebung dieser sogenannten Dirac-Punkte kann die Ladungsträgerdynamik in Graphen mittels der masselosen zweidimensionalen Dirac-Gleichung beschrieben werden [7]. Das führt neben solch interessanter Eigenschaften wie einer sehr hohen elektrischen [45] und thermischen Leitfähigkeit [6] zur Zugänglichkeit zu relativistischer Physik; ein Bereich, der ansonsten für Experimente nur äußerst schwer zugänglich ist, da interessante relativistische Phänomene nur unter extremen Bedingungen (sehr hohe Energien oder Leistungen) auftreten [132]. Inspiriert von diesem besonderen Material basiert die vorliegende Arbeit auf einer optischen Struktur aus miteinander gekoppelten Wellenleitern, die honigwabenförmig wie die Atome in Graphen angeordnet sind [61]. Durch die formelle Korrespondenz zwischen der Schrödingergleichung für Materiewellen und der paraxialen Helmholtzgleichung für die Ausbreitung optischer Wellen, stellt dieses sogenannte photonische Graphen ein Modellsystem für atomares Graphen dar. Die Honigwabengitterstruktur eröffnet auch in der Optik ganz neue Möglichkeiten, wie z. B. die Realisierung eines pseudomagnetischen Feldes oder einen Zugang zur Erforschung des neuen Gebiets der topologischen Photonik. Ein Feld, das von hohem physikalischen Interesse bezüglich neuartiger Anwendungen ist [100], da topologische Größen durch eine herausragende Robustheit gekennzeichnet sind.

Die Erforschung genau dieser topologischen Robustheit der Dirac-Punkte war Kern des ersten Hauptteils der vorliegenden Arbeit [87]. Dabei wurden die zwei unterschiedlichen Dirac-Punkte des reziproken Gitters immer weiter angenähert bis sie verschmolzen, wodurch sich ihre topologischen Größen aufhoben und eine echte Bandlücke geöffnet wurde. Erreicht wurde dieser Prozess durch eine lineare Kompression des Wellenleitergitters von zwei gegenüberliegenden Seiten ausgehend. Überdies findet dabei ein Übergang zwischen zwei Oberflächenzuständen statt, der experimentell bestätigt wurde. Der hier gezeigte Ansatz ist allgemein gültig für honigwabenförmige Gittersysteme und ein klassisches Beispiel für einen topologischen Phasenübergang.

Die Realisierung des ersten ultrastarken pseudomagnetischen Feldes in der Optik im zweiten Teil der Arbeit ist ein neuer Ansatz, der bisher unbekannte Möglichkeiten für photonische Strukturen eröffnet [91]. Dazu wurde das Wellenleitergitter von photonischem Graphen in einer bestimmten inhomogenen Art und Weise verzerrt. Die dabei erzielte extrem hohe magnetische Flussdichte des pseudomagnetischen Feldes von ca. 5500 T ist im Falle von atomarem Graphen nicht realisierbar, da das Gitter trotz seiner großen Stabilität vorher zerreißen würde. Wie auch unter Einwirkung eines echten Magnetfeldes wird die Verteilung der Zustände im reziproken Raum durch das pseudomagnetische Feld stark modifiziert. Es werden entartete Landauniveaus mit extrem erhöhter Zustandsdichte und Bandlücken zwischen denselben generiert. Folglich ist dieses Konzept bei seiner Übertragung auf photonische Kristalle vielversprechend zur Effizienzerhöhung bei nichtlinearen Prozessen. Die Generalisierung des hier gezeigten Konzepts auf Gittersysteme außerhalb der Optik ermöglicht neue interessante Physik, die sich grundlegend von derjenigen in strikt periodischen Strukturen unterscheidet.

Im letzten Hauptteil der Arbeit wurde zum ersten Mal eine in der Optik zuvor nur in theoretischen Ideen [98, 99, 102, 103] existierende Struktur realisiert und seine Funktionsweise demonstriert: ein photonischer topologischer Isolator [97]. Urpsrünglich aus der Festkörperphysik kommend, ist ein topologischer Isolator ein neuartiger Phasenzustand eines Materials, der sich durch seinen außergewöhnlichen Oberflächenladungstransport auszeichnet. Dieser ist immun gegen Streuung an Defekten oder Hindernissen; eine Robustheit, die ansonsten nur von Supraleitern bekannt ist. Inspiriert vom Festkörperpendant wurde in den hier beschriebenen Experimenten anstelle von äußerst robustem Ladungstransport entlang der Oberfläche ebensolcher Lichttransport gezeigt. So wurden photonische topologische Oberflächenzustände demonstriert, welche um beliebige Ecken und Kanten des Gitterrandes propagieren ohne gestreut zu werden. Die dafür notwendige Öffnung einer topologisch nicht-trivialen Bandlücke wurde mittels einer helikalen Modulation der Lichtleiter entlang der Ausbreitungsrichtung erreicht, welche im atomaren Analogon dem Bruch der Zeitumkehrsymmetrie des Systems entspricht. Solch ein Lichttransport ist vielversprechend für verschiedenste Anwendungen, da hier keine sonst üblichen Streuverluste auftreten. Das in diesem Teil der Arbeit gezeigte Prinzip ist in vielerlei Hinsicht neuartig und konnte somit vormals verschlossene Türen auf dem Gebiet der topologischen Photonik öffnen: es repräsentiert nicht nur den ersten topologisch geschützten Lichttransport, der ohne externes Magnetfeld und bei optischen Wellenlängen funktioniert, sondern stellt auch die erste Implementierung eines Floquet topologischen Isolators dar.

Zusammenfassend konnte die Arbeit grundlegende und herausragende Schritte bei der Erschließung des Gebiets der Dirac- und topologischen Photonik leisten, was bei einem Blick auf die hohe Zahl von Folgearbeiten sofort deutlich wird. Dabei hat sich das mittels Femtosekundenlaser geschriebene Wellenleitergitter in Honigwabenanordnung, inspiriert von atomarem Graphen, als exzellente Basis und vielseitiges Werkzeug herausgestellt. Die gezeigte Physik wird in zukünftigen Schritten auf andere optische Systeme und auf weitere Gittertypen übertragen werden, mit immer stärker werdendem Fokus auf Anwendungen in der Optik. Darüber hinaus dienten meine Ergebnisse aber auch als Inspiration in anderen Gebieten der Physik, wie z.B. für Experimente mit Ensembles kalter Atome [121], in der Optomechanik [122, 123], Mechanik [124] und Akustik [125], wo topologische Prinzipien bereits adaptiert wurden.

LIST OF OWN PUBLICATIONS

- L. J. Maczewsky*, J. M. Zeuner*, S. Nolte, and A. Szameit, "Observation of photonic anomalous Floquet Topological Insulators," ArXiv e-prints (2016).
- J. M. Zeuner*, M. C. Rechtsman*, Y. Plotnik, Y. Lumer, S. Nolte, M. S. Rudner, M. Segev, and A. Szameit, "Observation of a Topological Transition in the Bulk of a Non-Hermitian System," Phys. Rev. Lett. **115**, 040402 (2015).
- Y. Plotnik*, M. C. Rechtsman*, D. Song*, M. Heinrich, J. M. Zeuner, S. Nolte, Y. Lumer, N. Malkova, J. Xu, A. Szameit, Z. Chen, and M. Segev, "Observation of unconventional edge states in 'photonic graphene'," Nat. Mater. **13**, 57 (2014).
- J. M. Zeuner, M. C. Rechtsman, S. Nolte, and A. Szameit, "Edge states in disordered photonic graphene," Opt. Lett. **39**, 602 (2014).
- Y. V. Kartashov, J. M. Zeuner, A. Szameit, V. A. Vysloukh, and L. Torner, "Light scattering in disordered honeycomb photonic lattices near the Dirac points," Opt. Lett. **38**, 3727 (2013).
- R. Keil, J. M. Zeuner, F. Dreisow, M. Heinrich, A. Tünnermann, S. Nolte, and A. Szameit, "The random mass Dirac model and long-range correlations on an integrated optical platform," Nat. Commun. **4**, 1368 (2013).
- M. C. Rechtsman, Y. Plotnik, J. M. Zeuner, D. Song, Z. Chen, A. Szameit, and M. Segev, "Topological Creation and Destruction of Edge States in Photonic Graphene," Phys. Rev. Lett. **111**, 103901 (2013).
- M. C. Rechtsman*, J. M. Zeuner*, Y. Plotnik*, Y. Lumer, D. Podolsky, F. Dreisow, S. Nolte, M. Segev, and A. Szameit, "Photonic Floquet topological insulators," Nature

496, 196, - highlighted in ***News and Views*** (2013).

- M. C. Rechtsman*, J. M. Zeuner*, A. Tünnermann, S. Nolte, M. Segev, and A. Szameit, "Strain-induced pseudomagnetic field and photonic Landau levels in dielectric structures," Nat. Photon. **7**, 153, - highlighted in ***News and Views*** (2013).
- J. M. Zeuner, N. K. Efremidis, R. Keil, F. Dreisow, D. N. Christodoulides, A. Tünnermann, S. Nolte, and A. Szameit, "Optical Analogues for Massless Dirac Particles and Conical Diffraction in One Dimension," Phys. Rev. Lett. **109**, 023602 (2012).
- J. M. Zeuner, M. C. Rechtsman, R. Keil, F. Dreisow, A. Tünnermann, S. Nolte, and A. Szameit, "Negative coupling between defects in waveguide arrays," Opt. Lett. **37**, 533 (2012).
- U. Naether, J. M. Meyer, S. Stützer, A. Tünnermann, S. Nolte, M. I. Molina, and A. Szameit, "Anderson localization in a periodic photonic lattice with a disordered boundary," Opt. Lett. **37**, 485 (2012).
- J. Meyer, A. Brückner, R. Leitel, P. Dannberg, A. Bräuer, and A. Tünnermann, "Optical Cluster Eye fabricated on wafer-level," Opt. Express **19**, 17506 (2011).

---

* equally contributed

CONFERENCE CONTRIBUTIONS

- J. M. Zeuner, S. Stützer, Y. Plotnik, Y. Lumer, M. A. Bandres, M. Segev, M. C. Rechtsman, and A. Szameit, "Realization of Topological Anderson Insulators," ICTP - Conference on Interactions and Topology in Dirac Systems (smr2823), Trieste, Italy, ***invited*** (2016).
- T. Eichelkraut, S. Weiman, J. M. Zeuner, and A. Szameit, "Managing Radiation Loss in Photonic Waveguides for Applications in PT-Symmetric Systems," CLEO/QELS Conference, paper SF1P.6, San Jose, USA (2016).
- J. M. Zeuner, M. C. Rechtsman, Y. Plotnik, Y. Lumer, S. Nolte, M. S. Rudner, M. Segev, and A. Szameit, "Probing Topological Invariants in the Bulk of Non-Hermitian Photonic Lattices," CLEO/Europe-IQEC, Munich, Germany (2015).
- J. M. Zeuner, M. C. Rechtsman, Y. Plotnik, Y. Lumer, D. Podolsky, F. Dreisow, S. Nolte, M. Segev, and A. Szameit, "Experimental Implementation of Photonic Floquet Topological Insulators," Topolight 2015: 8th Optoelectronics and Photonics Winter School on "Topological Effects in Photonics", Trento, Italy, poster (2015).
- J. M. Zeuner, M. C. Rechtsman, Y. Plotnik, Y. Lumer, S. Nolte, M. S. Rudner, M. Segev, and A. Szameit, "Bulk optical measurement of topological numbers in photonic lattices with a non-Hermitian system," CLEO/QELS Conference, paper FW3C.3, San Jose, USA (2014).
- J. M. Zeuner, "Photonisches Graphen - Physikalische Effekte in honigwabenförmig angeordneten Wellenleitern," Greifswalder physikalisches Kolloquium, Greifswald, Germany, ***Kolloquium*** (2013).

- J. M. Zeuner, M. C. Rechtsman, S. Nolte, and A. Szameit, “Edge states in disordered photonic graphene,” 546. WE-Heraeus-Seminar on "Light in disordered Photonic Media", Bad Honnef, Germany, poster (2013).
- J. M. Zeuner, M. C. Rechtsman, S. Nolte, and A. Szameit, “Disordered Photonic Graphene,” CLEO/QELS Conference, paper QTh3D.3, San Jose, USA (2013).
- J. M. Zeuner, M. C. Rechtsman, S. Nolte, M. Segev, and A. Szameit, “Photonic Graphene: Honeycomb waveguide lattices,” Graphene Week, paper GW2013-91, Chemnitz, Germany (2013).
- J. M. Zeuner, Y. Plotnik, M. C. Rechtsman, Y. Lumer, M. Segev, and A. Szameit, “Experimental Demonstration of Photonic Floquet Topological Insulators,” CLEO/Europe-IQEC, Munich, Germany (2013).
- J. M. Zeuner, M. C. Rechtsman, M. Segev, and A. Szameit, “Strain-induced Magnetic Field in Photonic Graphene,” 518. WE-Heraeus-Seminar on Quantum Optical Analogies: a Bridge between Classical and Quantum Physics, Bad Honnef, Germany, poster (2012).
- J. M. Zeuner, N. K. Efremidis, R. Keil, F. Dreisow, D. N. Christodoulides, A. Tünnermann, S. Nolte, and A. Szameit, “One-Dimensional Massless Dirac-Particles,” CLEO/QELS, paper QW1E.3, San Jose, USA (2012).
- J. M. Zeuner, M. C. Rechtsman, R. Keil, F. Dreisow, A. Tünnermann, S. Nolte, and A. Szameit, “Negative Coupling Between Two Defect Waveguides,” CLEO/QELS, paper QM1E.5, San Jose, USA (2012).
- J. Meyer, A. Brückner, R. Leitel, P. Dannberg, A. Bräuer, and A. Tünnermann, “Ultracompact imaging system based on multi aperture architecture,” Photonics West, Proc. SPIE 7930, 79300C, San Francisco, USA (2011).

EHRENWÖRTLICHE ERKLÄRUNG

Ich erkläre hiermit ehrenwörtlich, dass ich die vorliegende Arbeit selbständig und ohne unzulässige Hilfe Dritter sowie ohne Benutzung anderer als der angegebenen Hilfsmittel und Literatur angefertigt habe. Aus anderen Quellen direkt oder indirekt übernommenen Daten und Konzepte sind unter Angabe der Quellen gekennzeichnet.

Bei der Erstellung und Auswertung des folgenden Materials haben mir die nachstehend aufgeführten Personen in der jeweils beschriebenen Weise unentgeltlich geholfen:

1. Die BPM Simulationen und die Berechnungen zu Abbildung 3.5 wurden von M. Rechtsman, damals Technion, durchgeführt.
2. Die Messungen in Kapitel 3.2 und in Abb. 5.4 wurden von Y. Plotnik und M. Rechtsman, Technion, gewonnen.

Weitere Personen waren an der inhaltlich-materiellen Erstellung der vorliegenden Arbeit nicht beteiligt. Insbesondere habe ich hierfür nicht die entgeltliche Hilfe von Vermittlungs- bzw. Beratungsdiensten (Promotionsberatern oder anderen Personen) in Anspruch genommen. Niemand hat von mir unmittelbar oder mittelbar geldwerte Leistungen für Arbeiten erhalten, die im Zusammenhang mit dem Inhalt der vorgelegten Dissertation stehen.

Die Arbeit wurde bisher weder im In- noch im Ausland in gleicher oder ähnlicher Form einer anderen Prüfungsbehörde vorgelegt.

Teile dieser Arbeit wurden aus Prioritätsgründen bereits veröffentlicht bzw. zur Veröffentlichung eingereicht [87,91,97].

Die geltende Promotionsordnung der Physikalisch-Astronomischen Fakultät ist mir bekannt.

Ich versichere ehrenwörtlich, dass ich nach bestem Wissen die reine Wahrheit gesagt und nichts verschwiegen habe.

Jena, 11. Oktober 2016 Julia Zeuner